RIKAGAKU KENKYUSHO
the Institute of Physical and Chemical Research
Wako-shi, Saitama Pref., JAPAN

'71

IPCR cyclotron Progress Report 1971

Vol. 5

Edited by Administration Committee of the IPCR Cyclotron

IPCR Cyclotron Progress Report 1971

Vol. 5

The Institute of Physical and Chemical Research
"RIKAGAKU KENKYUSHO" Wako-shi, Saitama, 351 JAPAN
December, 1971

This volume contains recent information of the IPCR Cyclotron, informal reports and abstracts of papers which will be published at scientific meetings or in publications by staff members, guests, and visitors.

This volume is dedicated to the memory of
Dr. Kazuhisa Matsuda

Kazuhisa Matsuda
1922–1971

KAZUHISA MATSUDA

In the midst of a full life, Kazuhisa Matsuda, chief of the Cyclotron Laboratory, the Institute of Physical and Chemical Research, died on 29 March at the age of 48 due to an accident. Deeply grieved, his colleagues suddenly lost a devoted friend who was a great leader in the field of nuclear physics in Japan.

He, graduated from the University of Tokyo in 1946, started his life as a scientist at Tokyo Institute of Technology. When the plan of construction of a new cyclotron at the Institute for Nuclear Study, University of Tokyo, started, he joined the construction group and played an important role to realize the variable-energy cyclotron. Then he woked mainly on the direct nuclear reactions, at first the elastic and inelastic scattering of protons on light and medium weight nuclei and then the transfer reactions. He was one of the pioneers who showed the existence of the resonance structure in the intermediate energy region.

He was also distinguished in developing the experimental technology. He designed the high resolution particle analyzers for INS FF and FM cyclotron with which valuable data on nuclear structure have been obtained.

In 1964 he joined the cyclotron laboratory of IPCR to construct the new cyclotron. Here he was a leader of the machine developing group and the nuclear physics group.

For a long time he was the chairman of the low energy nuclear physics committee in Japan and made efforts to construct the new AVF cyclotron in Osaka.

There was much that Kazuhisa Matsuda wanted to do if the sudden end of his life did not come. The warmth of his presence is bitterly missed but he has left the lasting imprint of his personality on whole who are acquainted with him.

CONTENTS

		Page
1.	INTRODUCTION	1
2.	MACHINE OPERATION	2
3.	MACHINE DEVELOPMENT AND ACCELERATOR PHYSICS	
	3-1. Production of Multiply-Charged Ions of Ne, Ar, Kr, and Xe by the Electron-Bombarded Hot Cathode Ions Source	5
	3-2. Charge Exchange Experiment (3) Cross Sections for Electron Loss and Capture of Nitrogen Ions in Various Gases	11
	3-3. Acceleration of Tritium Ions and Measurements of Residual Tritium in the Cyclotron	16
	3-4. Design of the Power Supply Distributor for the Beam Handling System of Cyclotron	19
	3-5. Safety Devices of the Beam Handling System to Prevent Radiation Hazard and Vacuum Trouble	22
	3-6. Improvement of the Beam-Handling System for Experiments of Nuclear Physics	25
4.	NUCLEAR PHYSICS Scattering and Reactions	
	4-1. ^{27}Al (^{12}C, ^{11}B) ^{28}Si and ^{27}Al (^{12}C, ^{13}N) ^{26}Mg Reactions	28
	4-2. The $^{100,98}Mo$ (t, p) $^{102,100}Mo$ Reactions and Low-Lying 0^+ States in Even Molybdenum Isotopes	31
	4-3. The ^{27}Al (^{3}He, p) ^{29}Si Reaction at 21.89 MeV	35
	4-4. Elastic Scattering of Alpha Particles from Even-Mass Molybdenum Isotopes	38
	4-5. The Manual of the Code for the Form Factor Computation of the Two-Nucleon Transfer Reaction	40
	4-6. The Spin-Flip Probability in the $^{92,94}Mo$ (p, p′) Reaction	42
	4-7. Spin Flip in the Inelastic Scattering of ^{3}He on ^{12}C	44

5. NUCLEAR PHYSICS
Nuclear Spectroscopy

5-1. The Level Structures of Light Even Strontium Isotopes Produced by $^{70,72,74,76}Ge$ (^{12}C, 4n) Reactions 46

5-2. Magnetic Moment of the 8^+ State of ^{206}Po 51

5-3. Magnetic Moment of the Lowest 6^+ State in ^{42}Ca 54

5-4. Decay of ^{87}Zr and ^{85}Zr 57

5-5. New Isomer in ^{148}Gd 63

6. NUCLEAR INSTRUMENTATION

6-1. Development of a Wire Spark Chamber with Ferrite Cores for a Broad Range Magnetic Spectrometer 68

6-2. A Mechanical Beam Chopper for Millisecond Beam Pulsing 72

6-3. A γ-Ray Spectrometer for Nuclear Study 75

6-4. Data Processor 78

7. RADIOCHEMISTRY

7-1. Chemical Behavior of Carbon in Semiconductor Silicon in the Dissolution and Fusion of the Matrix 80

7-2. Excitation Function for Some Triton-induced Reactions 83

7-3. A Mössbauer Spectroscopic Study of Chemical States of ^{119}Sn after EC Decay of ^{119}Sb in Antimony Chalcogenides 85

7-4. Charge States of Ions Produced by the Decay of ^{18}F 88

8. RADIATION CHEMISTRY AND RADIATION BIOLOGY

8-1. Radiolysis of Ketones in High LET Region 90

8-2. LET Effect in the Radiolysis of Some Organic Liquids 93

8-3. LET Effects on Bacterial Cells 95

9. SOLID STATE PHYSICS

9-1. Electron Microscopic Observation on Helium Bubbles in Aluminum Irradiated by Alpha-Particles 98

9-2. Point Defects in Irradiated Copper and Cu_3Au 101

9-3. Polarized Positron Annihilation in Ferromagnetic Nickel..... 105

10. RI PRODUCTION AND ITS APPLICATIONS

10-1. Production of Radioisotope for Medical and Agricultural Use 109

11. RADIATION MONITORING

11-1. Routine Monitoring 110

11-2. Individual Monitoring for Internal Contamination with Tritium 111

12. LIST OF PUBLICATIONS 114

13. LIST OF PERSONNEL 116

AUTHOR INDEX 119

1. INTRODUCTION

The participation of scientists of diverse fields in the research work with a large experimental facility such as cyclotron usually presents numerous difficulties concerning the use of machine and relevant instruments. In the research ensemble using our cyclotron, however, these difficulties are set aside step by step with accumulation of valuable experiences, and well-balanced developments in all fields of research are realized as seen in this report.

It is one of the remarkable features of the machine that one and the same target can be easily bombarded with different projectiles. The inelastic scattering of protons and alpha particles on molybdenum isotopes was thus found to give different β_2 values for the different projectiles. After the test runs made twice in the preceding period, tritium ions were accelerated up to 24 MeV for the first time in the cyclotron. (t,p) Reactions on ^{100}Mo and ^{98}Mo and isotope production by tritons were studied. Many kinds of radioisotopes were produced by the procedures developed here and supplied for use in medical and other fields. The energy dependence of the single transfer reaction with heavy ions was investigated. Use of heavy ions for the studies of radiation chemistry and radiation biology revealed a new process in the radiolysis of solution under large LET and an important role of delta rays in the radiation effect on bacteria was suggested. A simulation study of the radiation damage of nuclear fuel casing is being made in cooperation with the Japan Atomic Energy Research Institute.

The need for a large modification or innovation of the accelerator and other facilities has been foreseen in these several years and investigations of various possibilities thereof are under way, though not mentioned in this report.

It is our great regret that we have lost our colleague K. Matsuda who was to succeed H. Kumagai as chief of the Cyclotron Laboratory and to lead the work on the accelerator as well as on nuclear physics.

T. Hamada

Tatsuji Hamada, Chairman
Administration Committee of
the IPCR Cyclotron

2. MACHINE OPERATION

Machine Group

During the interval from Nov. 1970 to Oct. 1971 the cyclotron was operated by a full-time system without any serious difficulty. There was a 5-day stoppage in April 1971 on account of K. Matsuda's sudden death. Modification of the target area for nuclear scattering forced extension of the summer shutdown by a week. In spite of these unusual circumstances and a shorter period than ordinary years by one month for taking statistics, the total hours of "on beam" had amounted to 4579 h as listed in Table 1. This will be increased over 5200 h in the 12-month base and nearly the same with that of the last year.

Scheduled machine time and subject of research are indicated in Table 2. The "on beam" time is about 86 % of the scheduled machine time. This means that over 95 % of the schedule has been fulfilled. The machine time reserved for machine inspection and repair or time for ion source exchange does not need beam. A machine improvement and maintenance group was formed, and began activity in May in collaboration with the operating crew. Material reserve of proper quantity for repair and

Table 1. Machine operation time by working time meter.

Date	Oscillator on	Ion source on
Nov. 19, 1970	17539.1 (h)	19166.6 (h)
Oct. 20, 1971	22118.0 (h)	24204.8 (h)
336 days	4578.9 (h)	5038.2 (h)
Percent of 336 days	56.8 %	62.5 %

Schedule for this period:

Machine time	221 (days)
Overhaul and installation	29 (days)
Vacation, Holidays	80 (days)

Table 2. Scheduled machine time and subject of research in Period VI.

Subject	Hours	Percent
Heavy ion reaction	333	Nucl. Phys. 52.5 %
Direct reaction	1094	
In-beam spectroscopy	1027	
RI production for nuclear spectroscopy	331	
Radio chemistry and RI production	300	Fields other than Nucl. Phys. 25.3 %
Radiation chemistry and radiation biology	445	
Solid state physics	273	
Heavy ion charge exchange	113	
Mössbauer source	128	
Track detector	12	
Nuclide identification study	74	
Heavy ion source study	153	Accelerator Phys. and Maintenance. 17.6 %
Particle analyser calibration	9	
Beam analyser calibration	45	
Alignment of beam handling system	96	
Machine inspection and repair	480	
Reserved for machine time adjustment	124	
Exchange of heavy ion and ordinary ion source	27	
RI production for other organizations	243	4.6 %
	5307	100 %

periodical investigation of various parts, especially change of septum before serious damage, have resulted in a good operating condition of the cyclotron. Some of the improvement works done or planned by the group are described in 3-4, 3-5 of this report.

Demand for heavy ions is increasing. In addition to the time definitely indicated in Table 2, about two-thirds of time for in-beam spectroscopy, radiation-chemistry and radiation-biology were used for research by heavy ions. RI production by heavy ions was also carried out. Production and acceleration of heavier ions than presently used are studied with the ion source of the cyclotron now used. Results for Ne, Ar, Kr, and Xe are described in 3-1.

Tritium ion was accelerated up to 24 MeV and several experiments were performed.

3. MACHINE DEVELOPMENT AND ACCELERATOR PHYSICS

3-1. Production of Multiply-Charged Ions of Ne, Ar, Kr, and Xe by the Electron-Bombarded Hot Cathode Ion Source

I. Kohno, Y. Miyazawa, T. Tonuma, T. Inoue
A. Shimamura, and S. Nakajima

In the cyclotron, several multiply-charged heavy ions such as C^{4+}, N^{4+}, N^{5+}, O^{4+}, and O^{5+} have been accelerated[1] and their ion beams have been employed in the study of nuclear and atomic physics, radiation chemistry and biology.

At present, it is planned to accelerate heavier elements in the cyclotron, and for this purpose the production of multiply-charged ions of Ne, Ar, Kr, and Xe is being studied by using the electron-bombarded hot cathode type ion source which has been used for production of C^{4+}, N^{5+}, and O^{5+} ions.[1]

In order to know the kind of ions which were extracted from the ion source and accelerated in the cyclotron, the m/q spectra of ion beams were measured with a beam probe fixed at the radius of 55 cm by varying the magnetic field strength from 0.5 to 2.0 Wb/m^2 under the conditions of constant oscillator frequency and dee voltage. The operating condition of the ion source is not changed under variable magnetic field strength from 0.6 to 1.9 Wb/m^2. An example of spectrum is shown in Fig. 1. Most of

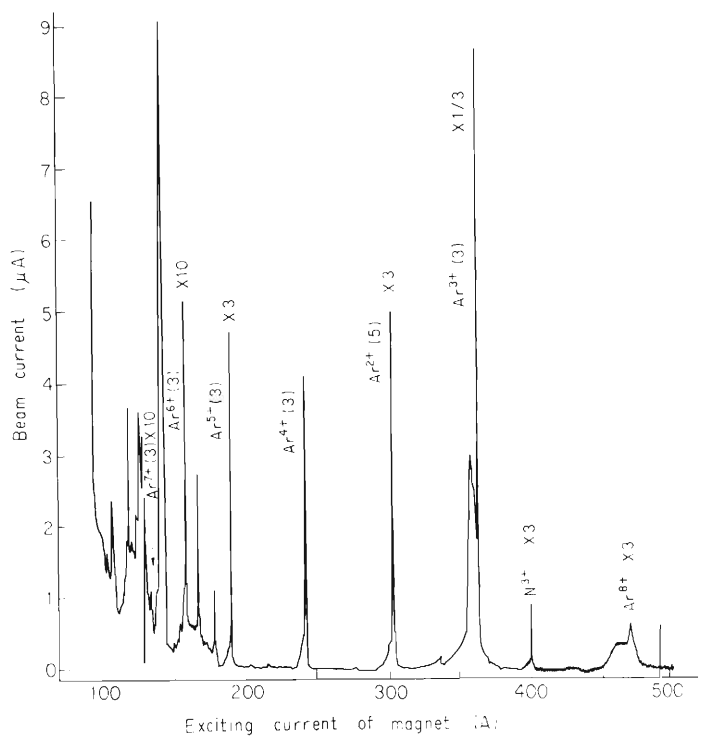

Fig. 1. The m/q spectrum of the ion beam measured at the radius of 55 cm by changing the magnetic field strength when Ar gas was fed.

multiply-charged heavy ions detected with a beam probe were accelerated by the 3rd harmonics of acceleration mode in the cyclotron, but some beams were accelerated by the fundamental mode or the 5th harmonics. The measured intensity of ion beam which was accelerated by the 3rd harmonics was about 0.5 % of the beam intensity extracted from the ion source (ion source output).

The measured spectrum when Ar gas was fed in the source is shown in Fig. 2(a). In the Ar gas several multiply-charged ions of ^{40}Ar isotope only were observed,

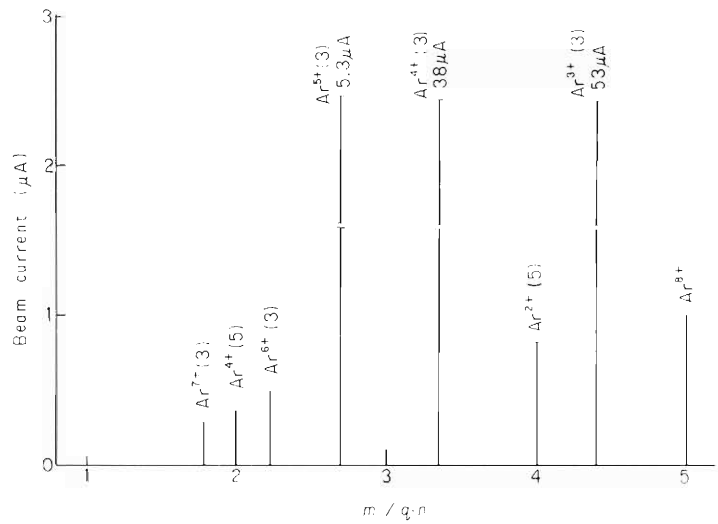

Fig. 2(a). The m/q spectrum of the ion beam when Ar gas was fed in the source. f = 6.5 MHz, Vd = 40 kV, arc power = 450V × 5A. (n) means a harmonic number of radio frequency.

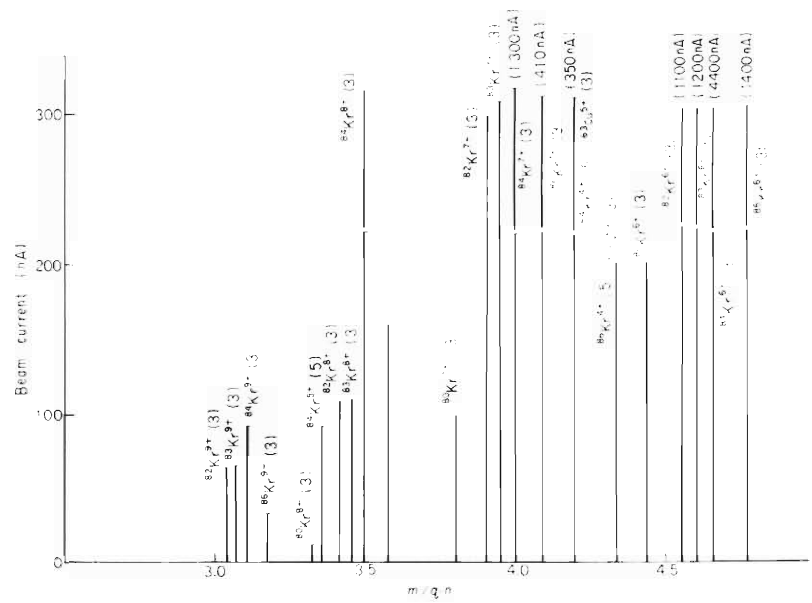

Fig. 2(b). The m/q spectrum of the ion beam when Kr gas was fed in the source. f = 6.0 MHz, Vd = 37 kV, arc power = 420V × 7.3A. (n) means a harmonic number of radio frequency.

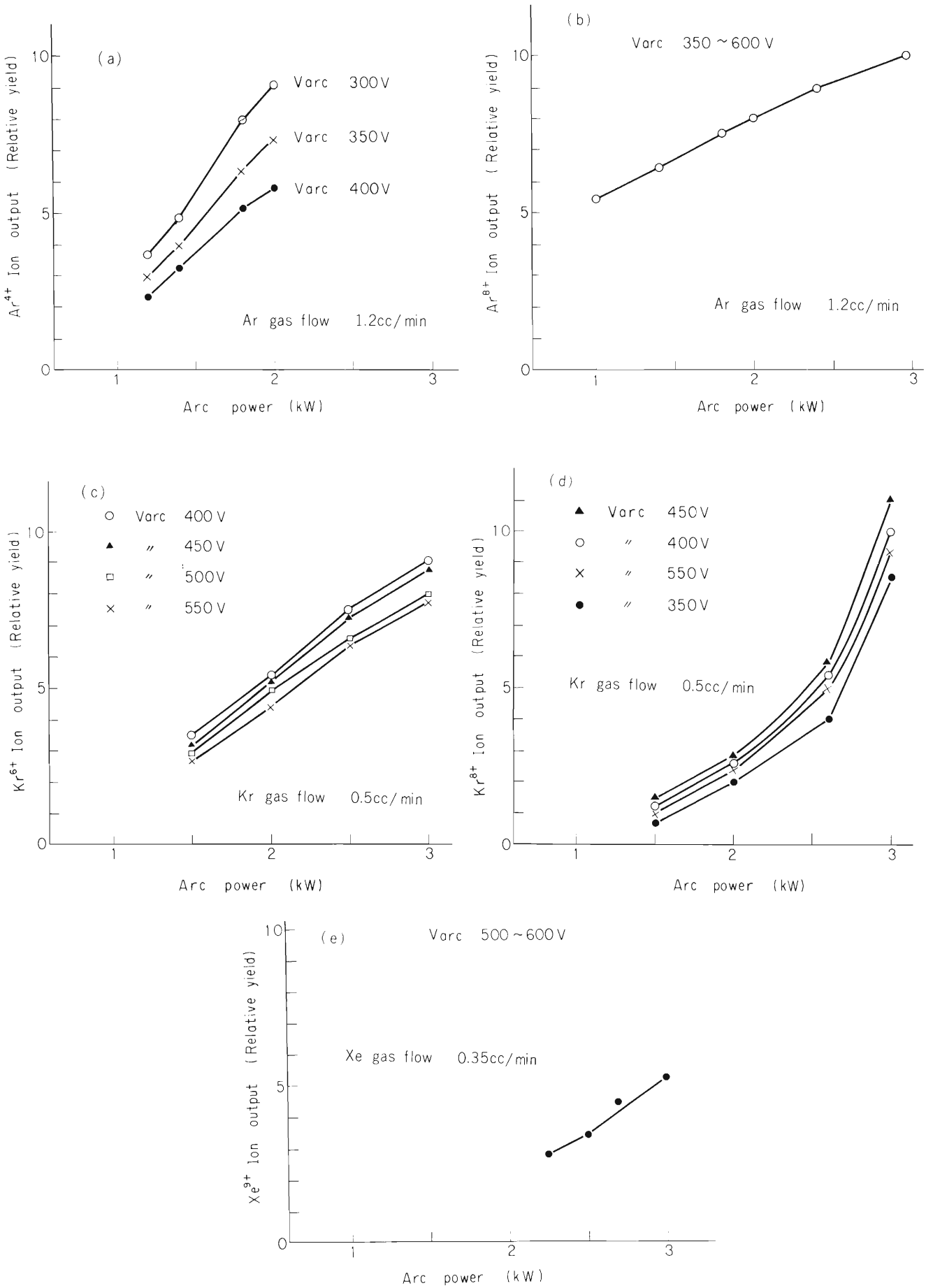

Fig. 3. Ar^{4+}, Ar^{8+}, Kr^{6+}, Kr^{8+}, and Xe^{9+} ion relative yields vs. are power.

because this isotope occupied an abundance of 99.6 %. Several peaks in this spectrum were assigned to Ar^{3+}, Ar^{4+}, Ar^{5+}, Ar^{6+}, and Ar^{7+} accelerated by the 3rd harmonics, Ar^{2+} and Ar^{4+} accelerated by the 5th harmonics and Ar^{8+} normally accelerated. Among them the intensity of Ar^{3+} accelerated by the 3rd harmonics was above 50 μA and that of the most highly charged ions Ar^{8+} accelerated normally was about 1 μA. Fig. 2(b) shows the measured spectrum when Kr gas was fed in the source. In Kr gas there were many multiply-charged ions of six Kr isotopes: ^{78}Kr, ^{80}Kr, ^{82}Kr, ^{83}Kr, ^{84}Kr, and ^{86}Kr ions. The observed peaks were assigned to Kr^{6+}, Kr^{7+}, Kr^{8+}, and Kr^{9+} of the six isotopes accelerated by the 3rd harmonics. Other two peaks with m/q = 4.2 and 4.3 were assigned to $^{84}Kr^{4+}$ and $^{86}Kr^{4+}$ accelerated by the 5th harmonics or to $^{63}Cu^{5+}$ and $^{65}Cu^{5+}$ accelerated by the 3rd harmonics. As these two peaks were measured also when Xe gas was fed in the source, they are supposed to be due to copper ions.

The electron bombardment power required to burn the arc discharge was about 500 W (1.2 kV × 0.4 A) in the cases of Ne, Ar, Kr, and Xe gases as well as in N_2 gas. The source was continuously operated with arc voltage (V arc) of 200 to 650 V and current (I arc) of 2.5 to 8 A, and then the arc power (V arc × I arc) was 1.0 to 3.0 kW. The gas flow rate was different according to the kind of gas. In the case of Xe gas, the gas flow rate was 0.2 to 0.7 cc/min, but Ar gas was introduced at the rate of 1.0 to 3.0 cc/min to keep arc plasma. Intensities of various multiply-charged ion beams

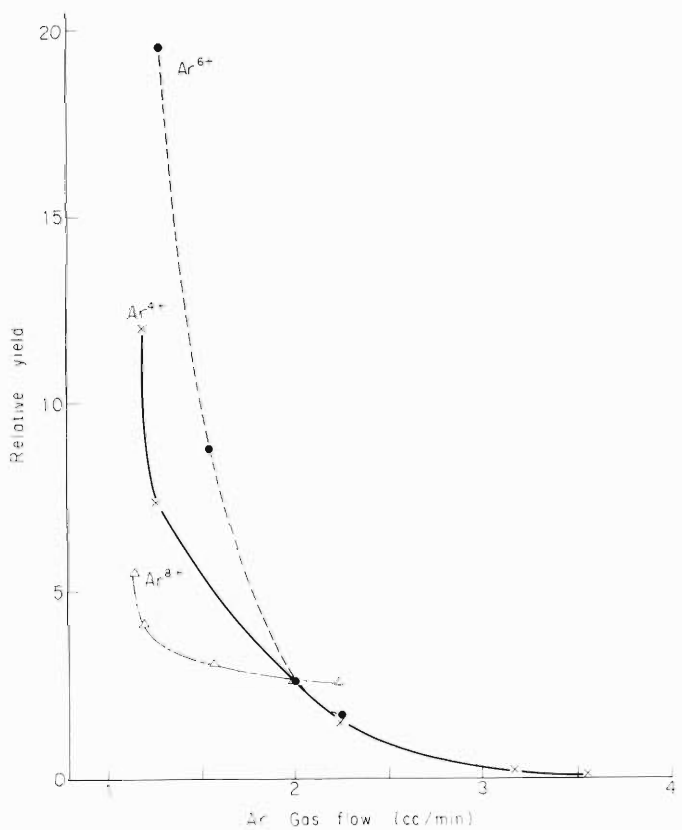

Fig. 4(a). The Ar^{4+}, Ar^{6+}, and Ar^{8+} relative yields vs. Ar gas flow rate. Each yield coincides with the value at 2 cc/min. Arc power = 450V × 5A.

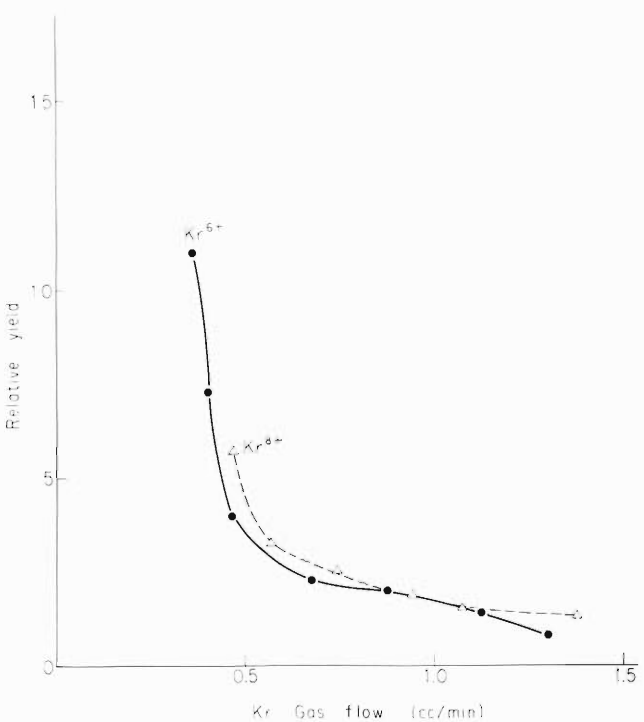

Fig. 4(b). The Kr^{6+} and Kr^{8+} relative yields vs. Kr gas flow rate. Each yield coincides with the value at 1 cc/min. Arc power = 450V × 5.5A.

depended mainly on the gas flow rate and the arc power. Figs. 3(a), (b), (c), (d), and (e) show the variation of yields of Ar^{4+}, Ar^{8+}, Kr^{6+}, Kr^{8+}, and Xe^{9+} versus the arc power at a constant gas flow rate. All multiply-charged ion yields increase with the arc power when the arc voltage is 300 to 600 V. Figs. 4(a) and (b) show the yields of Ar^{4+}, Ar^{6+}, Ar^{8+}, Kr^{6+}, and Kr^{8+} versus the gas flow rate for constant arc voltage and current for each gas. It is shown that the smaller gas flow brings about the higher yield of multiply-charged ions. As the multiply-charged ion yields depend on the gas flow rate more steeply than the arc power and a large arc power brings about a short life of source, it is better to operate the source with a smaller gas flow rate rather than with a larger arc power.

Relative abundance of charge states in Ne, Ar, Kr, and Xe was measured by observing the ion beams accelerated by the 3rd harmonics. In Table 1 the intensities of several ion currents extracted from the source are shown, and in Fig. 5 the relative

Table 1 The intensities of ion currents extracted from the source.

(mA)

Particle	Arc		Charge state									
	Va (V)	Ia (A)	2+	3+	4+	5+	6+	7+	8+	9+	10+	11+
^{20}Ne	380	5	12	7.5	0.55	0.04						
^{40}Ar	400	4		10	7	1	0.1	0.052	0.035			
^{84}Kr	420	7.3					0.65	0.26	0.11	0.44		
^{129}Xe	400	7.5								0.15	0.04	0.01

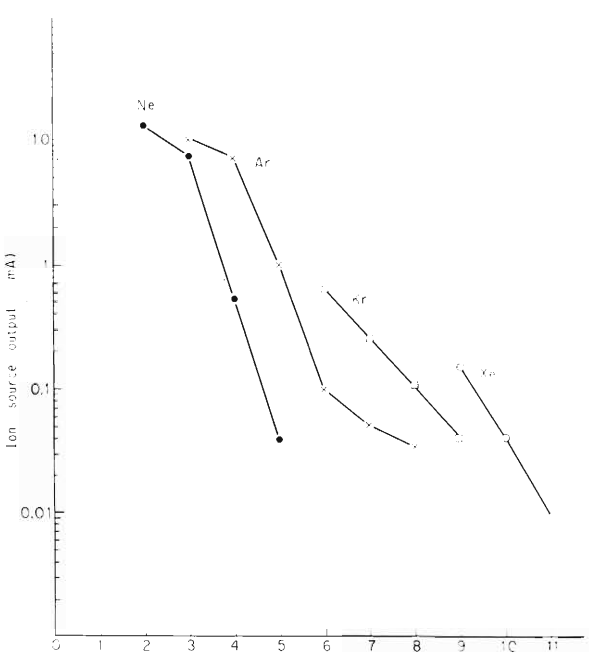

Fig. 5. Ion source output yields of Ne, Ar, Kr, and Xe charge states.

abundance of charge states in Ne, Ar, Kr, and Xe is shown. In the case of Ar, the relative abundance of charge states resembles Dubna's data[2] and the intensity of each charge state of Ar is almost the same as Argonne's data.[3] In the case of Kr and Xe, the intensities of observed multiply-charged ions decreased to 1/3 or 1/4 when the charge number is increased by one. The observed highest charge states were Ne^{5+}, Ar^{8+}, Kr^{9+}, and Xe^{11+}.

References

1) Y. Miyazawa and I. Kohno: Japan. J. Appl. Phys., 9, 532 (1970).
2) A. S. Pasyuk: Preprint OIYAI, No 7-3409, Dubna (1967).
3) G. S. Mavrogenes et al.: IEEE Trans. Nucl. Sci., NS/12, 769 (1965).

3-2. Charge Exchange Experiment (3)

Cross Sections for Electron Loss and Capture of Nitrogen Ions in Various Gases

T. Tonuma, F. Yoshida, I. Kohno,
Y. Miyazawa, T. Karasawa, T. Takahashi, and S. Konno

N^{4+} ions at energies of 65, 82, and 95 MeV were made to pass through H_2, He, N_2, Ne, Ar, Kr, and Xe gases, and the cross sections for electron loss and capture of the nitrogen ions were measured, the measurements being carried out essentially by the same method as had been reported.[1] The experimental apparatus and procedure were also the same as in the previous report except that the collision chamber was placed in a large vacuum chamber in which the pressure was made variable from 1×10^{-3} to 8×10^{-1} Torr by replacing $4\phi \times 20$ channels to $3\phi \times 20$ as shown in Fig. 1.

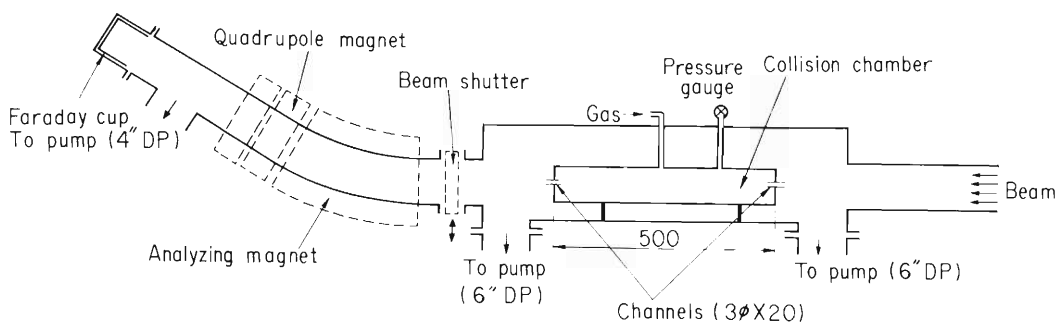

Fig. 1. Diagram of apparatus.

(1) Cross sections for electron loss and capture of nitrogen ions

The relative amounts F_k (k = 4, 5, 6, 7) of N^{4+}, N^{5+}, N^{6+}, and N^{7+} ions were observed when N^{4+} ions of energies mentioned above passed through the gases. $F_{4\infty}$ and $F_{5\infty}$, that is, the amounts of N^{4+} and N^{5+} states for a medium thick enough to reach equilibrium can be assumed to be zero and, therefore, the cross sections of σ_{54}, σ_{64}, σ_{65}, σ_{74}, and σ_{75} are negligible. Thus, the charge composition of ion beam is expressed by the following equations:

$$\begin{pmatrix} dF_4/d\pi \\ dF_5/d\pi \\ dF_6/d\pi \\ dF_7/d\pi \end{pmatrix} = \begin{pmatrix} -(\sigma_{45}+\sigma_{46}+\sigma_{47}) & 0 & 0 & 0 \\ \sigma_{45} & -(\sigma_{56}+\sigma_{57}) & 0 & 0 \\ \sigma_{46} & \sigma_{56} & -\sigma_{67} & \sigma_{76} \\ \sigma_{47} & \sigma_{57} & \sigma_{67} & -\sigma_{76} \end{pmatrix} \begin{pmatrix} F_4 \\ F_5 \\ F_6 \\ F_7 \end{pmatrix}. \tag{1}$$

The solutions of F_k are written as

$$F_4 = e^{a_{11}\pi} \tag{2}$$

$$F_5 = -\frac{a_{21}}{a_{22}-a_{11}}(e^{a_{11}\pi} - e^{a_{22}\pi}) \tag{3}$$

$$F_6 = \frac{(a_{22}-a_{11})(a_{31}+a_{44})-a_{21}(a_{32}+a_{44})}{(a_{22}-a_{11})(a_{11}-a_{33}-a_{44})} e^{a_{11}\pi}$$

$$+\frac{a_{21}(a_{32}+a_{44})}{(a_{22}-a_{11})(a_{22}-a_{33}-a_{44})} e^{a_{22}\pi}$$

$$+\frac{-a_{11}a_{22}a_{44}+(a_{33}+a_{44})\{a_{11}a_{44}+a_{21}(a_{32}+a_{44})-a_{31}(a_{22}-a_{33}-a_{44})\}}{(a_{33}+a_{44})(a_{11}-a_{33}-a_{44})(a_{22}-a_{33}-a_{44})}$$

$$\times e^{(a_{33}+a_{44})\pi}+\frac{a_{44}}{a_{33}+a_{44}} \tag{4}$$

$$F_7 = 1-(F_4+F_5+F_6), \tag{5}$$

where π is the number of gas atoms in a volume with 1 cm^2 cross section along the ion path and

$$a_{11} = -(\sigma_{45}+\sigma_{46}+\sigma_{47}),\ a_{21} = \sigma_{45},\ a_{31} = \sigma_{46},\ a_{41} = \sigma_{47}$$

$$a_{22} = -(\sigma_{56}+\sigma_{57}),\ a_{32} = \sigma_{56},\ \sigma_{42} = \sigma_{57}$$

$$a_{33} = -\sigma_{67},\ a_{44} = -\sigma_{76}.$$

The equilibrium states of F_6 and F_7 give the following relations:

$$\frac{F_{6\infty}}{F_{7\infty}} = \frac{\sigma_{76}}{\sigma_{67}} \text{ and } F_{6\infty}+F_{7\infty} = 1.$$

The cross sections were obtained by the least-square fit of the calculated F_k in the above to the measured F_k. Firstly, cross sections of a_{11} were obtained from the measured F_4 and Eqn. (2). Secondly, a_{21} and a_{22} were determined from the measured F_5, Eqn. (3) and a_{11} already known. Finally, the measured F_6, $F_{6\infty}$ and $F_{7\infty}$, Eqn. (4) and a_{11}, a_{21}, a_{22} (already known) determined the cross sections or a_{31}, a_{32} and a_{33}. Cross sections obtained by this procedure were σ_{45}, σ_{46}, σ_{47}, σ_{56}, σ_{57}, σ_{67}, and σ_{76} of nitrogen ions. The calculations were carried out with the DDP 124 computer in this laboratory.

Fig. 2 shows the relation between charge distribution and gas target thickness when 95 MeV N^{4+} ions traversed krypton gas. The solid points are values of measured F_k and solid lines show the calculated F_k using the cross sections determined by the above procedure. In H_2 and He media only σ_{45} was measured because the pressure in the apparatus could not be increased to the value necessary to attain the equlibrium states F_k for those media since cross sections are smaller in these gases.

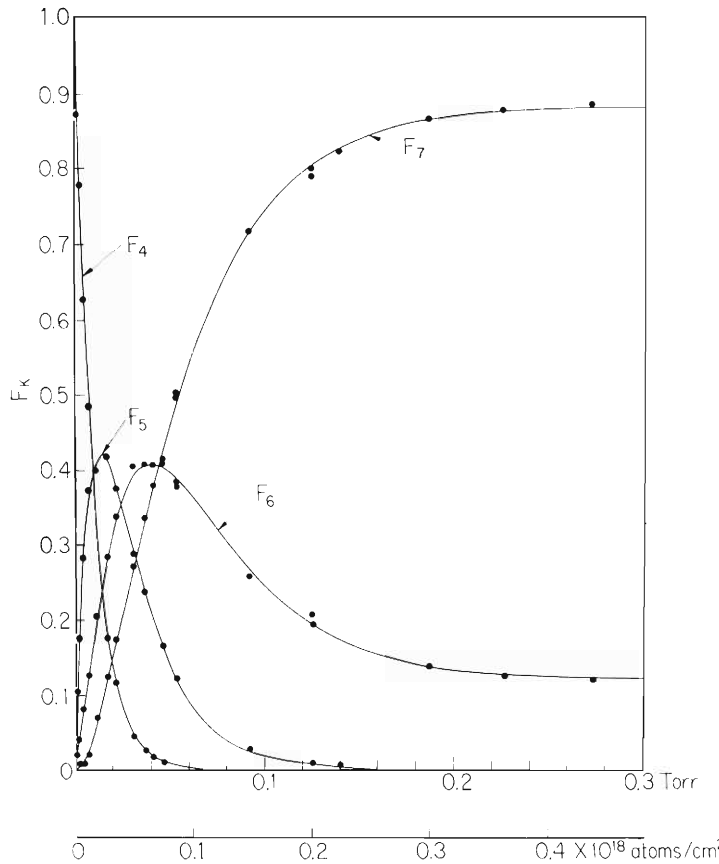

Fig. 2. Charge distribution vs. target thickness of krypton gas for 95 MeV N^{4+} ions. Solid lines are the calculated charge distributions using σ_{45}=50.9, σ_{46}=10.0, σ_{47}=0.7, σ_{56}=23.0, σ_{57}=6.2, σ_{67}=13.7 and σ_{76}=1.9 in unit of 10^{-18} cm^2/atom.

(2) The relation of cross sections to the atomic number Z_{med} of the medium

Fig. 3 shows the dependence of cross sections for single electron loss of σ_{45}, σ_{56}, and σ_{67}, and for single electron capture σ_{76} on the atomic number Z_{med} of the gases, the energies of nitrogen ions being 65, 82, and 95 MeV. The cross section σ_{45} is nearly proportional to Z_{med}^2 up to $Z_{med} \sim 10$ and to $Z_{med}^{2/3}$ approximately for the Z_{med} values larger than 10. The behavior is the same with the dependence of the cross section σ_{45} of carbon ions on Z_{med}.[2] The $Z_{med}^{2/3}$ effect follows from a shielding effect of atoms of a heavy medium. Since dependence of cross sections $\sigma_{i,\,i+1}$ on Z_{med} for ions of lower energies are affected by the shielding effect and the deformation of the atoms of the medium,[3] it is complicated to be treated theoretically. In the energy region of the present work, however, only the shielding effect approximated by the Thomas-Fermi model can explain the dependence of cross sections $\sigma_{i,\,i+1}$ on Z_{med}. Fig. 4 shows the comparison of the cross sections σ_{45}, σ_{56} and σ_{67} of 65 and 95 MeV nitrogen ions with the theoretical values derived by Bohr[4] and Dmitriev.[3] In the figure $\sigma_{i,\,i+1}$ (solid lines) up to $Z_{med} \sim 10$ are given by the formula in the free collision approximation without taking the shielding into account and for the

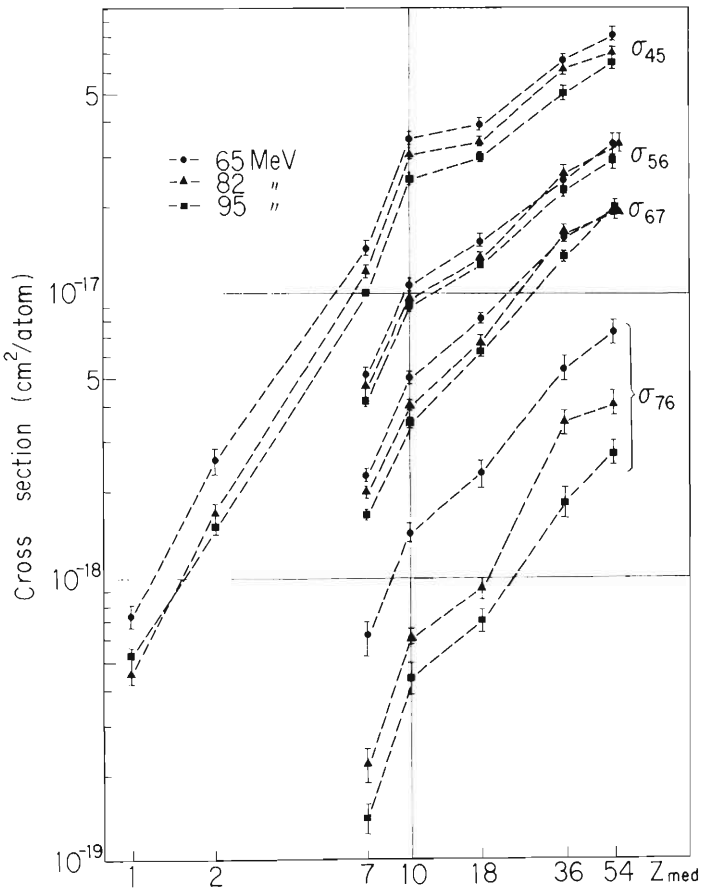

Fig. 3. The relation of the cross sections, σ_{45}, σ_{56}, and σ_{67}, for single electron loss and σ_{76} for single electron capture on the atomic number Z_{med} of the medium.

Z_{med} larger than 10 by the formula derived in the strongly shielded field of an atom. Dmitriev defines that electrons are lost mainly from the outermost shells in the ions (see Ref. 3)). Therefore, one electron in L-shell of nitrogen ions should be lost in the case of σ_{45}. But the values of σ_{45} shown in Fig. 4 are calculated on the assumption of two electrons being lost because the cross section of σ_{46}, which loses two electrons simultaneously, has a finite value.

The relation of σ_{46}, σ_{47}, and σ_{57} for multiple electron loss to Z_{med} could not be established because the observed cross sections involved large experimental uncertainties. The ratios of them to single loss are approximately $\sigma_{46}/\sigma_{45} = 0.1 \sim 0.3$, $\sigma_{47}/\sigma_{45} = 0.01 \sim 0.06$ and $\sigma_{57}/\sigma_{56} = 0.1 \sim 0.3$ for Z_{med} of from 10 up to 54 and these ratios increase with Z_{med}.

The cross section σ_{76} for single electron capture is proportional to $Z_{med} \sim Z_{med}^{3/2}$ and has the same dependence as σ_{65} of carbon ions.[2)]

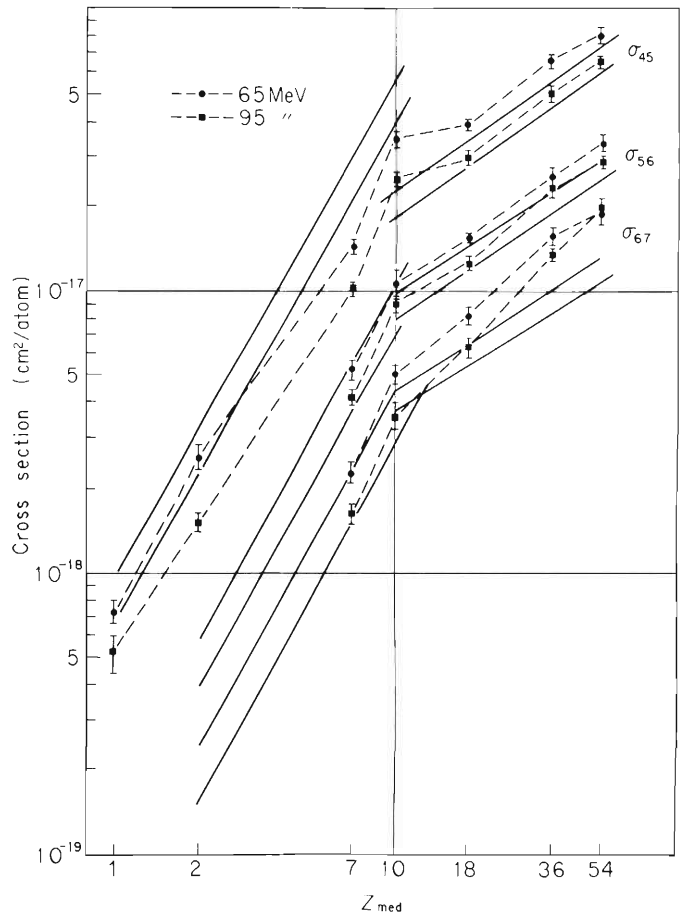

Fig. 4. The comparison of the cross sections, σ_{45}, σ_{56}, and σ_{67}, measured for 65 and 95 MeV N^{4+} ions with the theoretical values (solid lines) calculated with Bohr's and Dmitriev's formulas. Upper line for 65 MeV and lower line for 95 MeV.

References

1) T. Tonuma, Y. Miyazawa, T. Karasawa, and I. Kohno: Japan. J. Appl. Phys., 9, 1306 (1970).
2) T. Tonuma, Y. Miyazawa, T. Karasawa, I. Kohno, T. Takahashi, and S. Konno: IPCR Cyclotron Progr. Rep., 4, 15 (1970).
3) I. S. Dmitriev, V.S. Nikolaev, L. N. Fateeva, and Ya. A. Teplova: Sov. Phys. JETP., 15, 11 (1962).
4) N. Bohr: K. Danske Vidensk, Selsk. mat.-fys. Medd., 18, No. 8 (1948).

3-3. Acceleration of Tritium Ions and Measurements of Residual Tritium in the Cyclotron

I. Kohno, A. Shimamura, I. Sakamoto,
T. Tonuma, and T. Hamada

(1) Triton acceleration

Preliminary triton accelerations using 1 and 100 Ci tritium gas, respectively, were carried out in the preceding period in order to obtain technical experiences.[1] In this period a regular triton acceleration has been made for successive five days. Procedures of the experiment and measurements on residual tritium in the cyclotron and equipments involved were the same as in previous runs.

A mixture of 500 cc atm of deuterium gas and 40 cc atm (100 Ci) of tritium gas was prepared and supplied to the circulation system at a time. The ion source, which usually needs a gas flow of about 50 lus, was thus provided with a tritium gas flow of about 3.7 lus (44 Ci/h). The acceleration was continued for 15 ~ 25 h with one supply of the gas mixture to the system. The time of duration depended on the amount of leakage of air to the acceleration chamber, the circulation system and the beam handling system. In the present run a leakage of less than 0.5 lus was found at the target chamber.

When the beam intensity decreased considerably due to leakage of air as well as outgasing, a charcoal trap through which the gas was circulated at room temperature was cooled by liquid nitrogen for adsorption of all gases, and it was replaced by a new one. Then, another batch of the gas mixture containing 100 Ci of tritium was introduced to the system and the next acceleration run was started. 700 Ci in total of tritium gas was used through the whole runs.

At the end of each run, the remaining tritium was collected in the charcoal trap and another liquid nitrogen trap made of glass, then they were disconnected from the system and hydrogen gas was introduced and circulated for "washing" the system. In the whole runs about 2 cc of water was condensed in the glass trap. These traps, filaments and cones of the ion source and pump oils were disposed of as radioactive wastes.

Intensities of deflected and analysed triton beams are 10 μA and 100 nA, respectively.

(2) Measurements of residual tritium

From the preliminary tests, it was known that there may be a possibility of a strong contamination of vacuum pump oil with tritium, and, therefore, oil samples from pumps were measured using the liquid scintillation counter. A concentration of as much as 960 μCi/cc was detected in the oil of circulation pump and main diffusion pump of the cyclotron.

Air samples taken from different places around the machine after machine shutdown were measured various times with ionization chambers of collection type, and moisture in the air was also collected in a liquid nitrogen trap, and water samples thus obtained were measured with the liquid scintillation counter. As the results of both measurements nearly coincided, it may be said that the tritium remains as a form of water. Results of the measurements are summarized in Table 1.

Table 1. Tritium concentration (in μCi/cc) in air during and after triton acceleration.

Contamination due to:	Time of sampling	Time after end of run	Control room	Circulation system	Blower exhaust	Ion source	Acceleration chamber	Resonating tank
Tritium leak	During acceleration		10^{-5}	10^{-5}				
	During loading or recovery of tritium*		10^{-4}	10^{-4}	$10^{-2}\sim10^{-4}$			
Release of residual tritium	Dec. 26, '70	1 h	10^{-4}	10^{-4}	10^{-4}	10^{-4}		
	Jan. 10, '71	15 d				10^{-5}	10^{-3}	10^{-3}
	Mar. 1	65 d				4×10^{-3}		6×10^{-3}
	Mar. 2**	66 d				3×10^{-4}	6×10^{-5}	1×10^{-4}
	Mar. 11	75 d				4×10^{-3}		2×10^{-3}
	Mar. 12**	76 d					7×10^{-5}	4×10^{-5}
	Apr. 27***	122 d				9×10^{-5}	6×10^{-5}	
	Jun 17***	173 d					3×10^{-5}	6×10^{-5}
	Jul. 5	191 d				1×10^{-3}		4×10^{-3}
	Jul. 5***	191 d				9×10^{-5}	1×10^{-5}	2×10^{-5}
	Aug. 16	231 d				1×10^{-2}	9×10^{-3}	6×10^{-3}
	Aug. 16***	231 d				3×10^{-5}	3×10^{-5}	1×10^{-5}
	Sept. 14	250 d						2×10^{-4}
	Sept. 14****	250 d					1×10^{-5}	1×10^{-5}
	Oct. 4	270 d						8×10^{-4}
	Oct. 4*****	270 d						5×10^{-6}

* Tritium leaked from an imperfect connection of exhaust pipe.
** After 20 h washing with fresh air.
*** " 4 h " "
**** After 1 h washing with fresh air.
***** " 40 min " "

It is seen from the table that, even in 9 months after the triton acceleration, a concentration of 10^{-3} μCi/cc of tritium has been detected in the air inside the acceleration chamber just after the exposure of the chamber to the atmosphere for overhaul. The concentration was, however, reduced to $10^{-4} \sim 10^{-5}$ μCi/cc by means of a compulsive blowing of fresh air to the chamber. The "blowing off" of the chamber was carried out by a roughing pump (1500 ℓ/min) and a mechanical booster pump, but at present they are replaced by a large blower having a capacity of 10 m^3/min. Though the level of tritium contamination is gradually decreasing, this procedure is still necessary before working in the chamber during overhaul to keep the concentration down to the maximum permissible limit.

A contamination of $0.5 \sim 0.9$ μCi/cm^2 of tritium was detected using the smear testing method on the inner surface of the chamber and it remained for two months. It may be due to the deep permeation of tritium to metal surfaces.

(3) Discussion

It is a remarkable fact that air blowing is much more effective to the reduction of tritium concentration than keeping the chamber in vacuum of 2×10^{-6} mmHg for a long time.

A simulation experiment will be done for investigating the behavior of tritium atoms adsorbed on metal surfaces.

Reference

1) I. Kohno et al.: IPCR Cyclotron Progr. Rep., 4, 11 (1970).

3-4. Design of the Power Supply Distributor for the Beam Handling System of Cyclotron

H. Nakajima and M. Hemmi

The analyzing and focusing system of the extracted beam is composed of seven courses, and now seventeen magnets are installed and operated. These magnets with the suitable combination of polarities and exciting currents achieve beam transport to various target areas. Fig. 1 shows the analyzing and focusing system of the cyclotron.

The directions for use of the magnets are not firmly established. Moreover, a pair of power supplies excites several quadrupole-pairs in turn and must be switched on to alternative pairs according to the course used. These situations make the operation of the beam transport system complicated causing operation mistake and machine trouble. Therefore, a central controlling system has been desired and planned in the last few years.

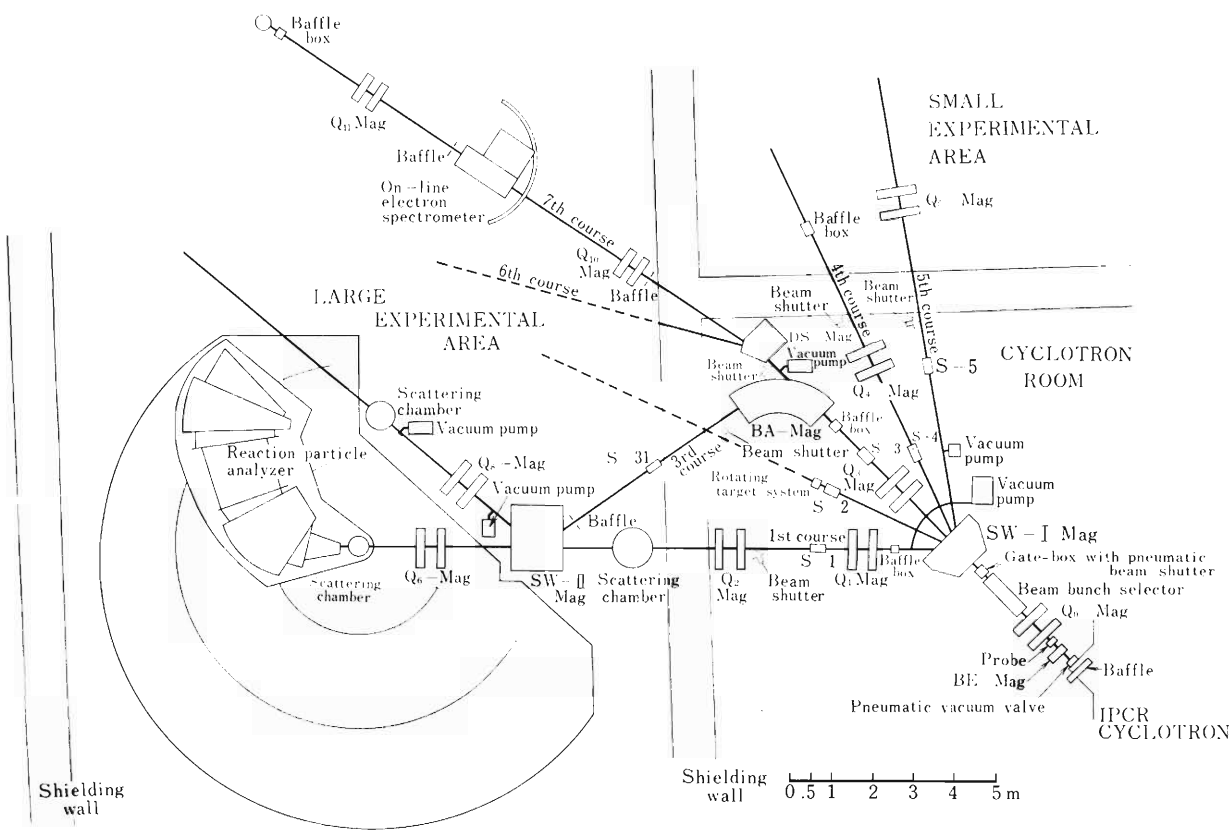

Fig. 1. Analyzing and focusing system of the cyclotron.

The distributor

The system has two functions; one is the selection of combination of magnets and power supplies, and the other is indication of the state of operation. The indication is given by a graphical display device in the control room, and the selection and control of main system in the cyclotron power room is made by switches on the display panel remotely. Block diagram of the system is shown in Fig. 2.

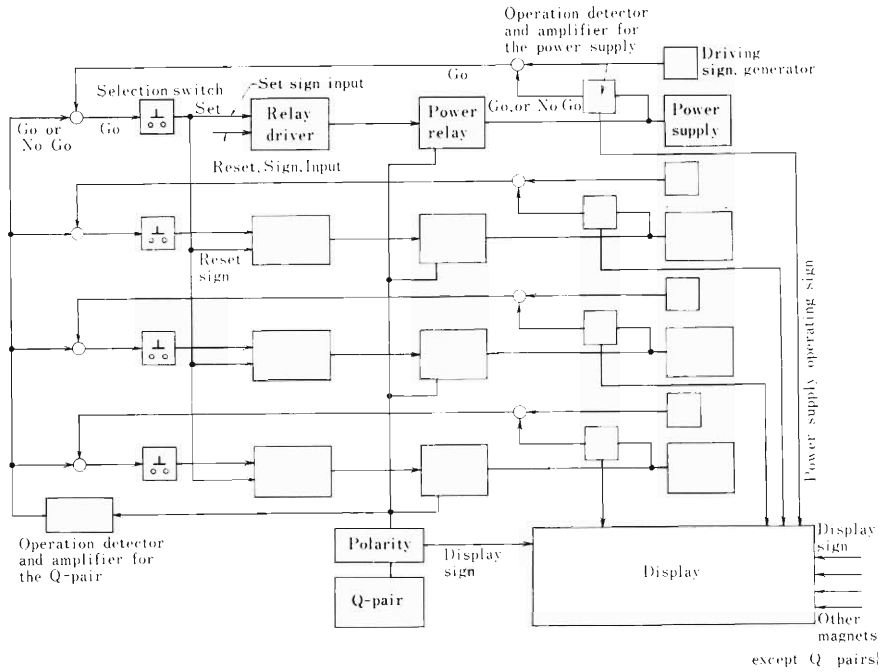

Fig. 2. Block diagram of the distributor. Block diagram is illustrated for a typical Q-pair.

(a) Selection of the combination of Q-magnets and power supplies

The selection is to be made among the Q-magnet assembly only. Each of the BA, SW I, SW II, DS,and BE magnets of Fig. 1, has an exclusive power supply. Therefore, no change of power supply is necessary. The selection system is capable of connecting 15 Q-pairs and 10 power supply pairs in maximum. A Q-pair can be connected with three emergency power supplies as well as be used alone normally. One special pair of power supply can be connected with any of the Q-pairs if necessary. Possible combination of Q-pair and power supply is determined by estimating the probability of troubles for each course and for operating frequency. Control units are standardized and are shown in Fig. 3 with their circuit schematics.

They have solid state discriminating safety circuits with logical levels that protect the connection system from operation mistake and other troubles such as change of combination of live magnet and power supply. Further, memory of the state of operation at the time of emergency shut-down can be preserved.

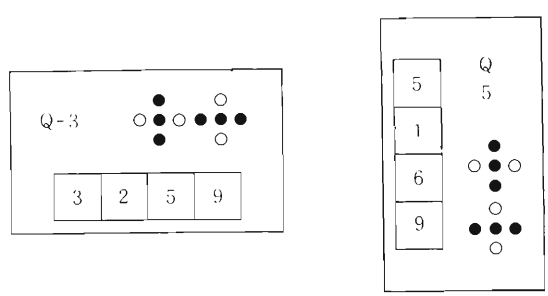

Fig. 3. (a) Control units.

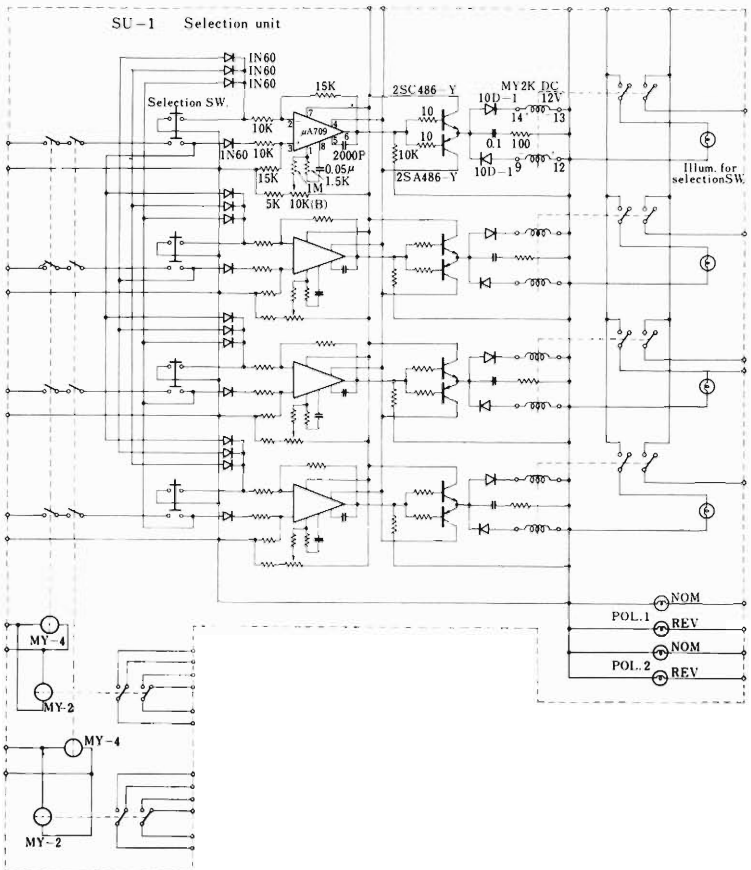

Fig. 3. (b) Schematic circuit of the control unit.

(b) Indication of the operation

A 2 m × 1.2 m panel displays the operating polarities of magnets and the state of beam transport graphically. In the Q-pair assembly, the operating unit indicates the connected power supply number and operating polarity of each magnet as well. The polarity is represented by a line on the panel denoting the motion of ion beam in the horizontal plane; convergence or divergence. The operating power supplies are also indicated with its numbers at the bottom of the graphical panel.

In the BE magnet, its polarity is indicated by the bending direction of ion beam.

For the SW I, SW II, BA, and DS magnets, the graphical display shows the transporting direction of beam. Fig. 4 shows the designed panel of graph.

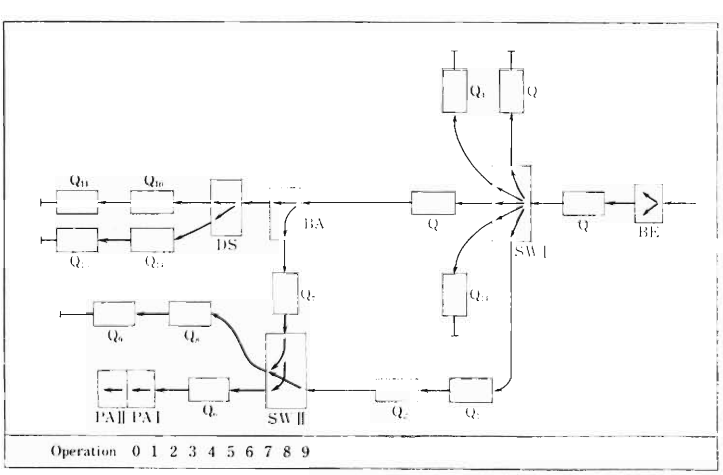

Fig. 4. Graphic display panel.

3-5. Safety Devices of the Beam Handling System to Prevent Radiation Hazard and Vacuum Trouble

M. Hemmi and H. Nakajima

There are seven beam courses in the extracted beam handling system of the cyclotron by which the beams are led to each target position. General layout of the beam handling system and safety devices can be seen in Fig. 1. The safety devices were designed and attached to the beam handling system to protect persons from radiation hazard and to the vacuum system from mis-operation or any other accident. Some are already in use and others are being installed. They will be described briefly.

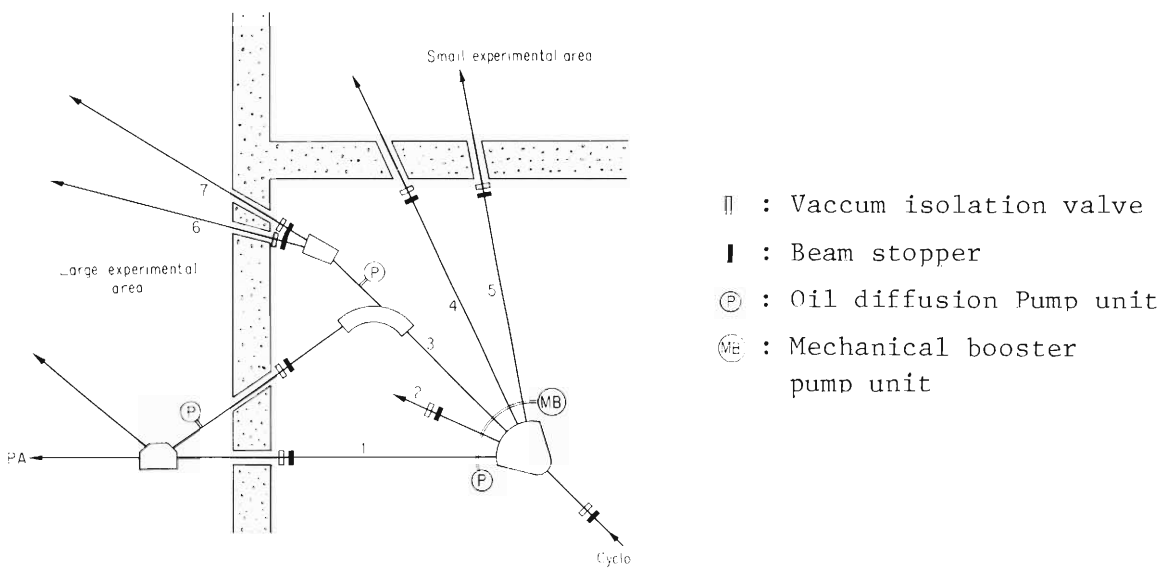

Fig. 1. Layout of the beam handling system and safety devices.

(1) Radiation hazard protection

Frequently, persons have to enter one experimental area when the cyclotron is bombarding the targets in the cyclotron vault or sending a beam to another area.

The beams must not be led to a place where any person is working in case of mis-operation or trouble of beam adjusting magnets.

Such is the aim of this device. It should also protect the surface of a vacuum valve from bombardment when it was shut off to isolate the beam pipe of the experimental area from the main vacuum.

The procedures of operation can be seen in Fig. 2. Signals indicating the state of doors of each area are given to a mixing and discriminating circuit and a distinction signal is fed to a beam stopper control circuit at a suitable location. The stoppers are set in the cyclotron vault and shut off the beams there from going downstream further.

Stopper control signals are also given by the position of the vacuum isolation valve, so that the stopper is always "in" when the valve is not opened. The beam stopper is a water-cooled graphite plate to minimize residual activity and is actuated by a pneumatic cylinder. The vacuum seal and bearing of the main shaft are made of glass wool and TEFLON containing molybdenum-disulphide.

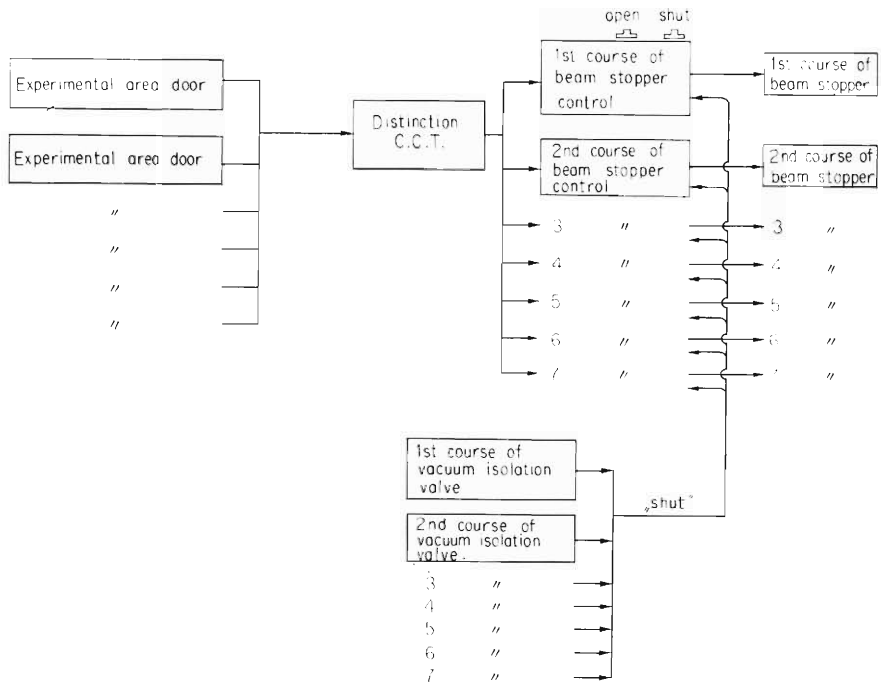

Fig. 2. Block diagram of the beam stopper system.

This structure is reliable in operation and any maintenance work is hardly necessary.

(2) Vacuum system protection

The vacuum system of the cyclotron and the beam handling system are desirable to be protected against vacuum failure at the end of each beam pipe where accidental leakage and breaking of foil of experimental apparatus are most likely to occur.

The systems must not also be left unguarded against unexpected failure of power supply. The protection divice is twofold. One is fast isolation of the beam pipe if failure has occurred, and the other is protection of the pumping system and automatic control of each evacuation stage.

(i) The isolation valves can be opened only under the condition of "good vacuum" of the corresponding branch of pipe and main volume of the beam system. "Good" condition is determined by two methods according to the desired vacuum pressure.

One uses Pirani detectors and gives trip signals at about 50 μHg. It is called high level unit. The other is a Penning ionization gauge to give an alarm at the threshold which can be arbitrarily set between 10^{-4} and 10^{-3} mmHg. It is called low level unit. A detector of the latter type is known to give a "good" reading when it is at the atmospheric pressure. A method to prevent this error is provided.

The device works always towards the safer side in case of accidents such as breaking or grounding of detector lead and failure of power supply.

It is standardized in the modular form and can be used in any place with an aim other than valve control. Analog output is also provided to give the vacuum pressure.

(ii) A vacuum unit is made up from rotary, mechanical booster and or oil diffusion pumps. Each has a region of pressure where it works properly. Many units are in use with the beam handling system and the cyclotron. Automatic control of these pumping systems seems necessary in view of need of simultaneous control of them taking into account of the vacuum condition at each site especially in case of emergency

such as unexpected power supply cut-off. Fig. 3 shows a standard evacuation set and Fig. 4 is the block diagram of automatic operation and protection. Given the criterion for each stage, the evacuation process proceeds automatically step by step evaluating the condition at each stage. When vacuum failure or power cut-off had coccured the pump system would not necessarily go back to the initial stage and the operation would be able to resume from a stage suitable for the vacuum condition of the volume to be evacuated again. Manual operation is of course possible. Standardization of an evacuation set to improve interchangeability is being planned.

The vacuum failure detection and control system is the same as that used for isolation valve operation and there is two kind of detectors according to the vacuum pressure range concerned as stated above.

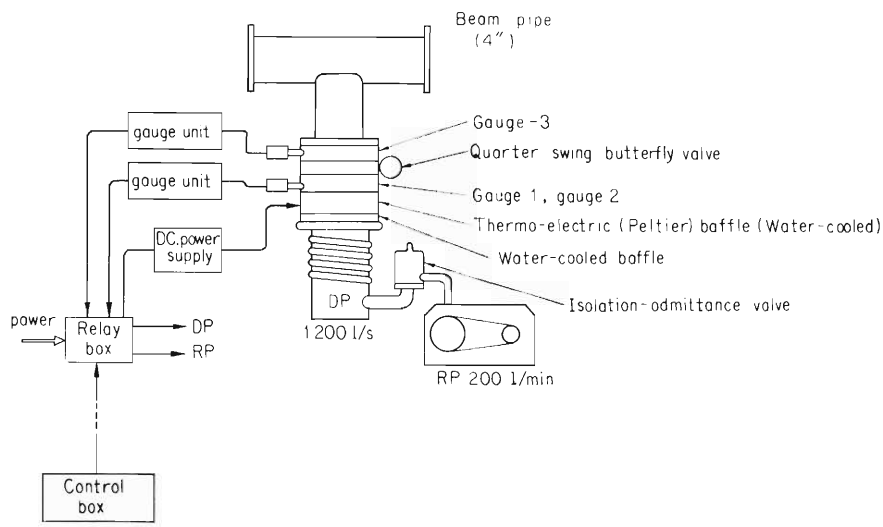

Fig. 3. Schematic view of evercuation set.

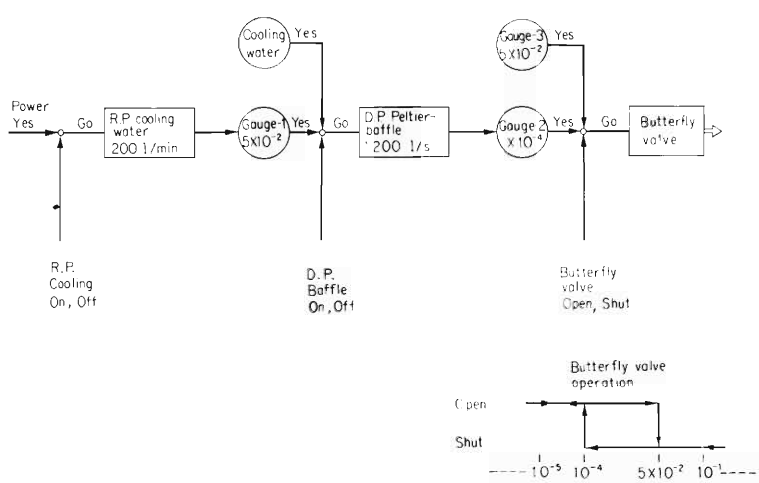

Fig. 4. Block diagram of automatic operation and protection.

3-6. Improvement of the Beam-Handling System for Experiments of Nuclear Physics

T. Wada, T. Fujisawa, and S. Motonaga

Two beam courses[1] have been used for the experiments of nuclear scattering until the completion of the PA system.[2] Because the energy analyzed beam cannot be used for other experiments after the completion of the PA system, a new deflecting magnet (SW-II) was installed in place of CL magnet. By means of this magnet the energy analyzed beam can be deflected in two directions. One is to the PA magnet and the other to the scattering chamber for SSD and particle-gamma experiments. The

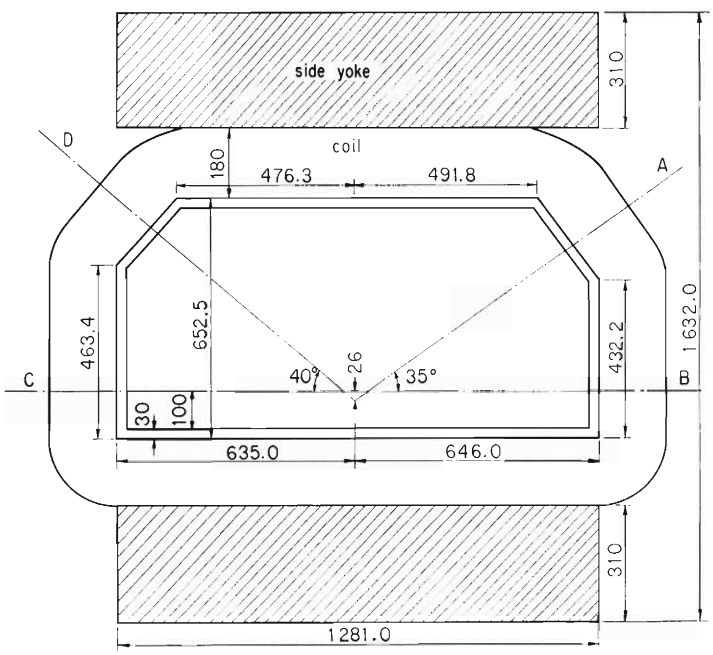

Fig. 1. Shape of the magnetic pole.

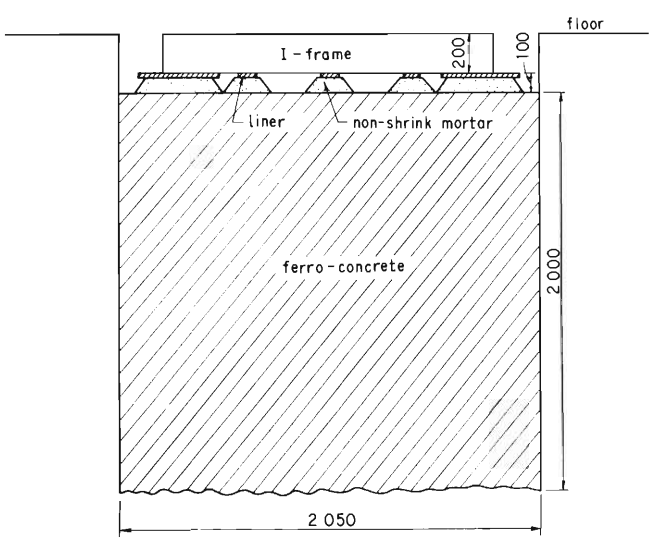

Fig. 2. Foundation of the SW-II magnet.

shape of the magnetic pole was designed by a computer to minimize its area. The results are shown in Figs. 1, 2, and Table 1. Fig. 3 is the excitation curve. Fig. 4 shows the beam-handling system around the new magnet. The beam optics for each course was calculated and shown in Fig. 5.

Table 1. Characteristics of the SW-II magnet.

Type	H-type
Pole gap	40 mm
Deflection angle	35^{o}, 40^{o}, 75^{o}
Maximum field	12 kg
Radius A-C	2132 mm
A-D	935 mm
B-D	1860 mm
Weight total	17.8 t
Cost	$36,000
Maker	Tohoku Metal Industries, Ltd.

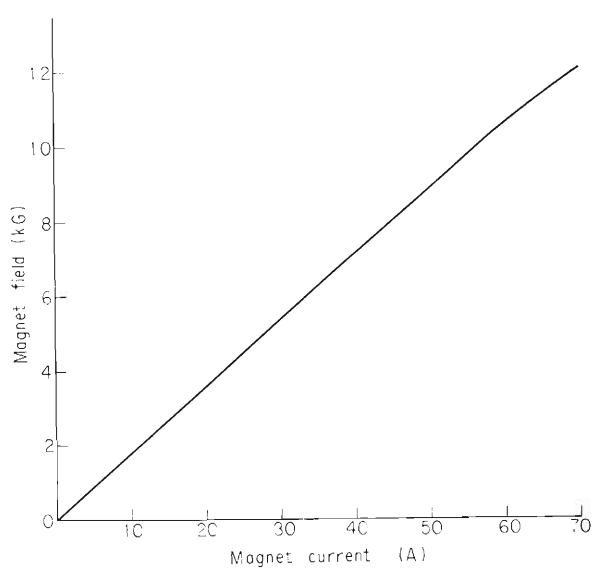

Fig. 3. Excitation curve.

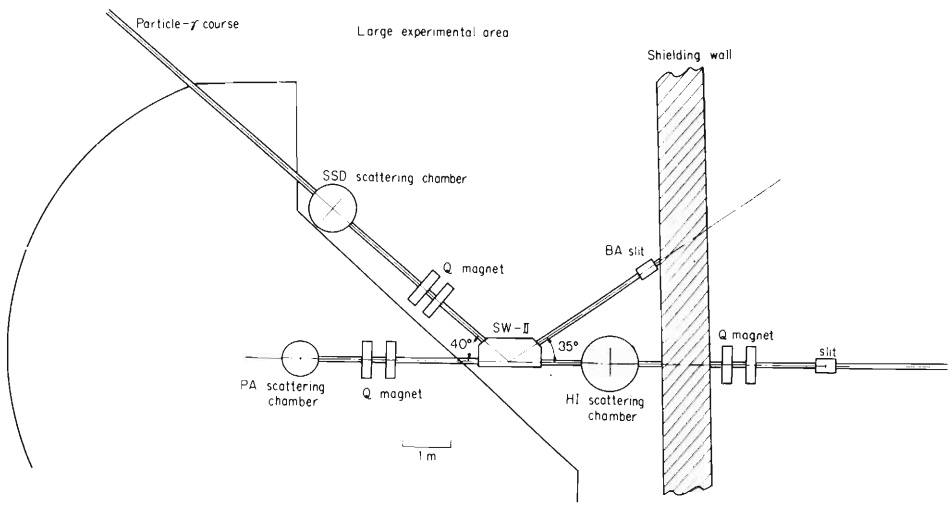

Fig. 4. Beam-handling system around the SW-II magnet.

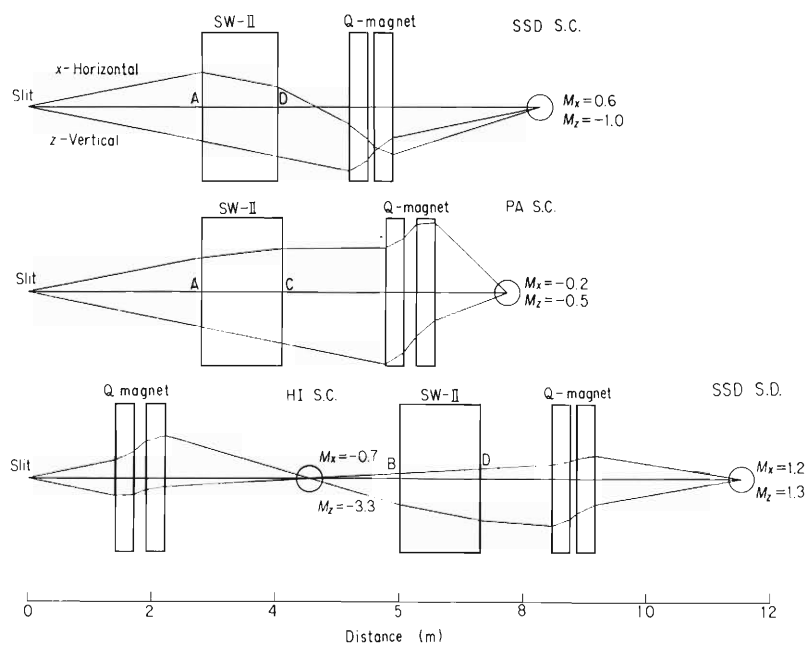

Fig. 5. Beam optics of each course.

References

1) S. Motonaga, H. Kamitsubo, M. Hemmi, N. Nakanishi, and K. Matsuda: IPCR Cyclotron Progr. Rep., 1, 10 (1967).
2) N. Nakanishi and K. Matsuda: Nucl. Instr. and Methods, 57, 245 (1967).

4. NUCLEAR PHYSICS

Scattering and Reactions

4-1. $^{27}Al(^{12}C, ^{11}B)^{28}Si$ and $^{27}Al(^{12}C, ^{13}N)^{26}Mg$ Reactions

S. Nakajima, I. Kohno, T. Tonuma,
and M. Odera

In order to study the reaction mechanism of one-nucleon transfer induced by heavy ions, the differential cross sections of $^{27}Al\,(^{12}C,\ ^{11}B)\,^{28}Si$ and $^{27}Al\,(^{12}C,\ ^{13}N)\,^{26}Mg$ have been measured with a ΔE-E counter telescope and a two-dimensional pulse height analyzer.

The ^{12}C beam extracted from the cyclotron was led into a 100 cm scattering chamber and focused in a size of 1.5 mm × 4 mm on a target. The energy resolution of the beam was about 0.5 % and the intensity was 30 nA ~ 100 nA. Thickness of the ^{27}Al target was 380 $\mu g/cm^2$. Combination of 15 μm and 200 μm surface barrier Si detector was used for the counter telescope. The electronic circuit of the detection system was described previously.[1)]

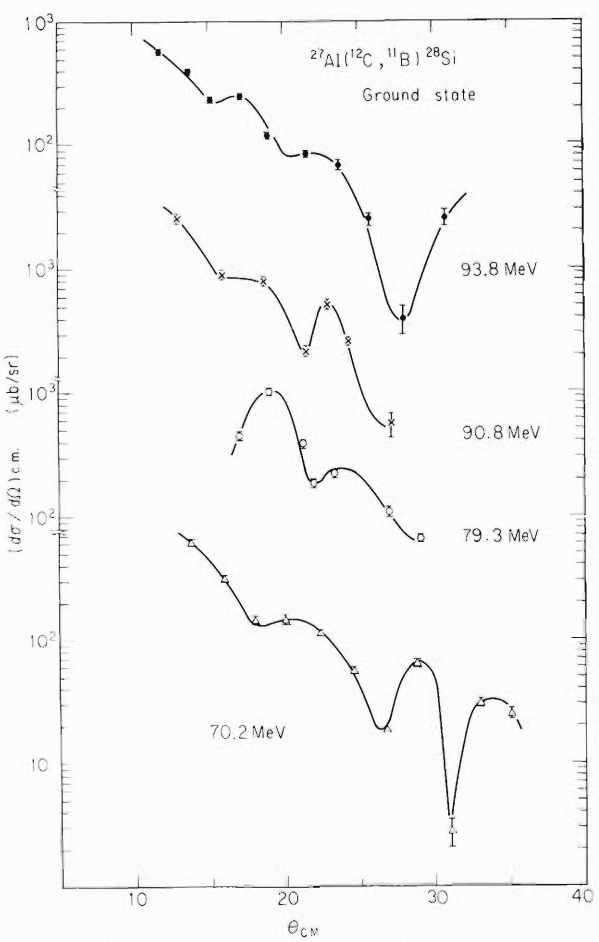

Fig. 1. Angular distributions of the reaction $^{27}Al\,(^{12}C,\ ^{11}B)\,^{28}Si$. The reaction products, ^{11}B and ^{28}Si, are both in their ground states.

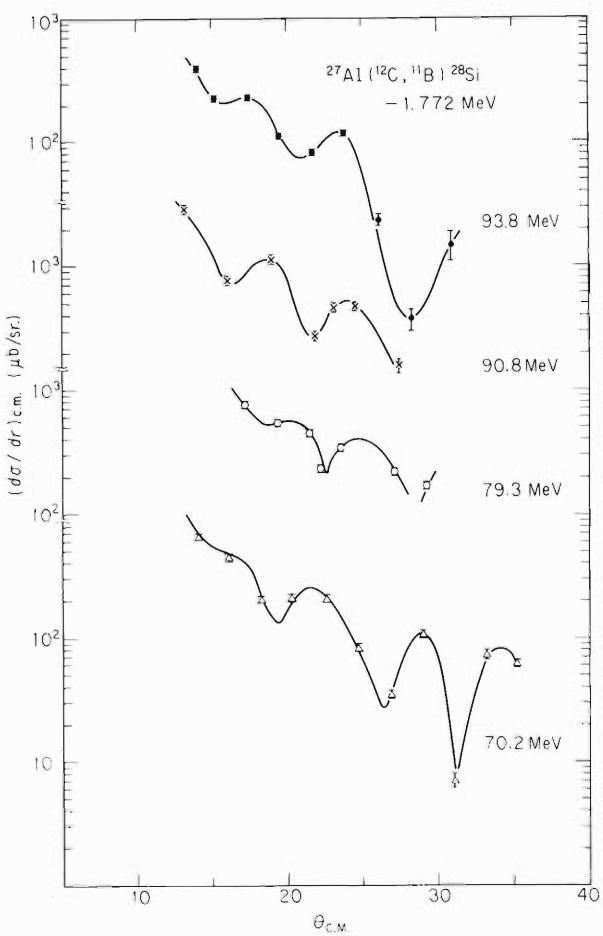

Fig. 2. Angular distributions of the reaction $^{27}Al\,(^{12}C,\ ^{11}B)\,^{28}Si$ leading to excited state of ^{28}Si (1.772MeV)

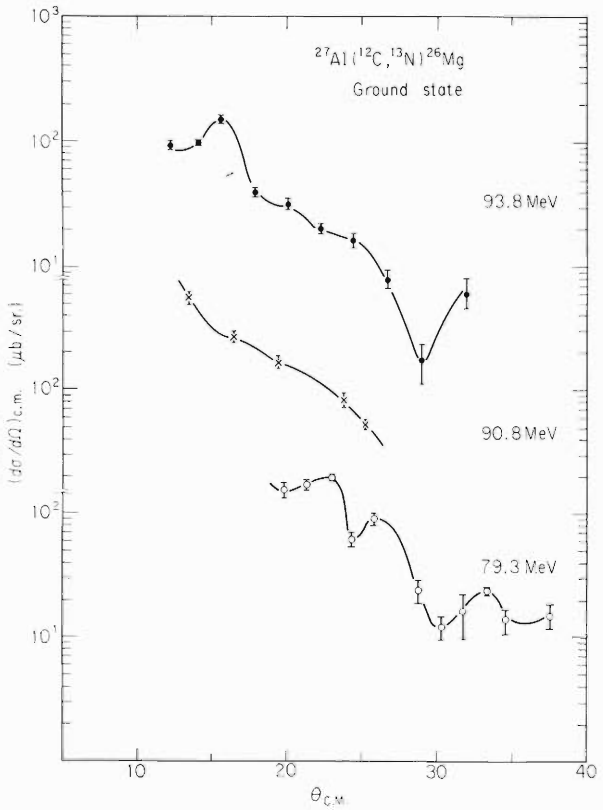

Fig. 3. Angular distributions of the reaction ^{27}Al (^{12}C, ^{13}N) ^{26}Mg. The reaction products, ^{13}N and ^{26}Mg, are both in their ground states.

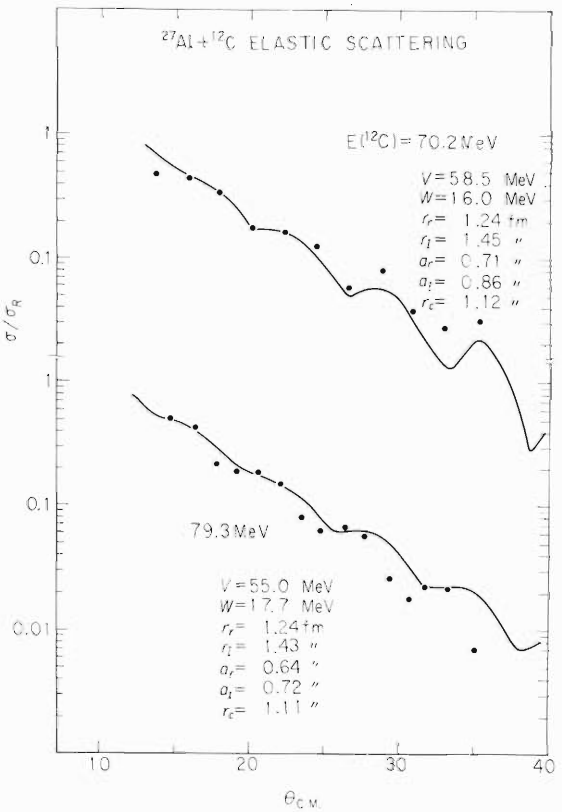

Fig. 4. Angular distributions of the elastic scattering of ^{12}C on ^{27}Al at the energies of 70.2 and 79.3 MeV and an example of optical model calculations of them.

Effects of variation of incident energy on the angular pattern were investigated by changing the ^{12}C energy at 70.2, 79.3, 90.8, and 93.8 MeV. These energies are all far above the Coulomb barrier of entrance and exit channels and the angular distributions obtained (Fig. 1, Fig. 2, and Fig. 3) show invariably a diffraction-like pattern which differs from one-peak feature at lower energies. Phases and absolute values of the pattern vary smoothly with energy. Any drastic change was not observed in this energy region. Comparing the cross section of ^{11}B to that of ^{13}N, it is indicated that the transfer of a proton from a target to a projectile is less favored than the transfer in the opposite direction as mentioned in the other case.[2) 3)] The data analyses by DWBA calculations are now under consideration.

Knowledge of the optical-model wave functions for the relative motion of the complex nuclei is necessary to describe transfer reactions in the DWBA. Angular distributions of the elastic scattering of ^{27}Al (^{12}C, ^{12}C) ^{27}Al have also been obtained. They resemble fairly well in shape with those of ^{28}Si + ^{12}C and ^{27}Al + ^{14}N at about the same energy.[4)] Optical parameter fits are being investigated with the "SEARCH" code written by T. Wada.[5)] Fig. 4 shows the angular distributions at incident energies of 70.2, and 79.3 MeV and an example of parameter fits to them.

References

1) S. Nakajima, I. Kohno, T. Tonuma, and M. Odera: IPCR Cyclotron Progr. Rep., 4, 35 (1970).
2) R. M. Diamond, A. M. Poskanzer, F. S. Stephens, W. J. Swiatecki, and D. Ward: Phys. Rev. Letters, 20, 802 (1968).
3) J. Galin, B. Gatty, M. Lefort, J. Peter, X. Tarrags, and R. Basile: Phys. Rev., 182, 1267 (1969).
4) I. Kohno, S. Nakajima, T. Tonuma, and M. Odera: J. Phys. Soc. Japan, 30, 910 (1971).
5) T. Wada: IPCR Cyclotron Progr. Rep., 2, 87 (1968).

4-2. The $^{100, 98}$Mo (t, p) $^{102, 100}$Mo Reactions and Low-Lying 0^+ States in Even Molybdenum Isotopes

K. Matsuda, S. Takeda, N. Nakanishi, I. Kohno,
Y. Awaya, S. Yamaji, and S. Kusuno

A low-lying 0^+ state at 736 keV of ^{98}Mo has been found experimentally by the E0 transition,[1] the ^{97}Mo (d,p) ^{98}Mo reaction[2] and the ^{100}Mo (p,t) ^{98}Mo reaction.[3] In the experiment of inelastic scattering of protons on the ^{98}Mo target,[4] this 0^+ state has been unable to find because of its small cross section compared with that of a close 2^+ state. On the contrary, the large cross section leading to the 0^+ state makes the 2^+ state undetectable in the ^{100}Mo (p,t) ^{98}Mo reaction.[3] The inelastic scattering of protons by ^{100}Mo also reveals a level at 700 keV being 0^+ state.[4]

Although the ground states of ^{98}Mo and ^{100}Mo appear to be describable under consideration of a simple shell-model by closed $2d_{5/2}$ and $3s_{1/2}$ neutron subshells respectively, configuration-mixing of neutron shells will play an important role not only in the ground states but also in the excited 0^+ states because of $2d_{3/2}$, $1g_{7/2}$ and $1h_{11/2}$ neutron orbits lying fairly close to those shells. Cheifetz et al. provided experimental

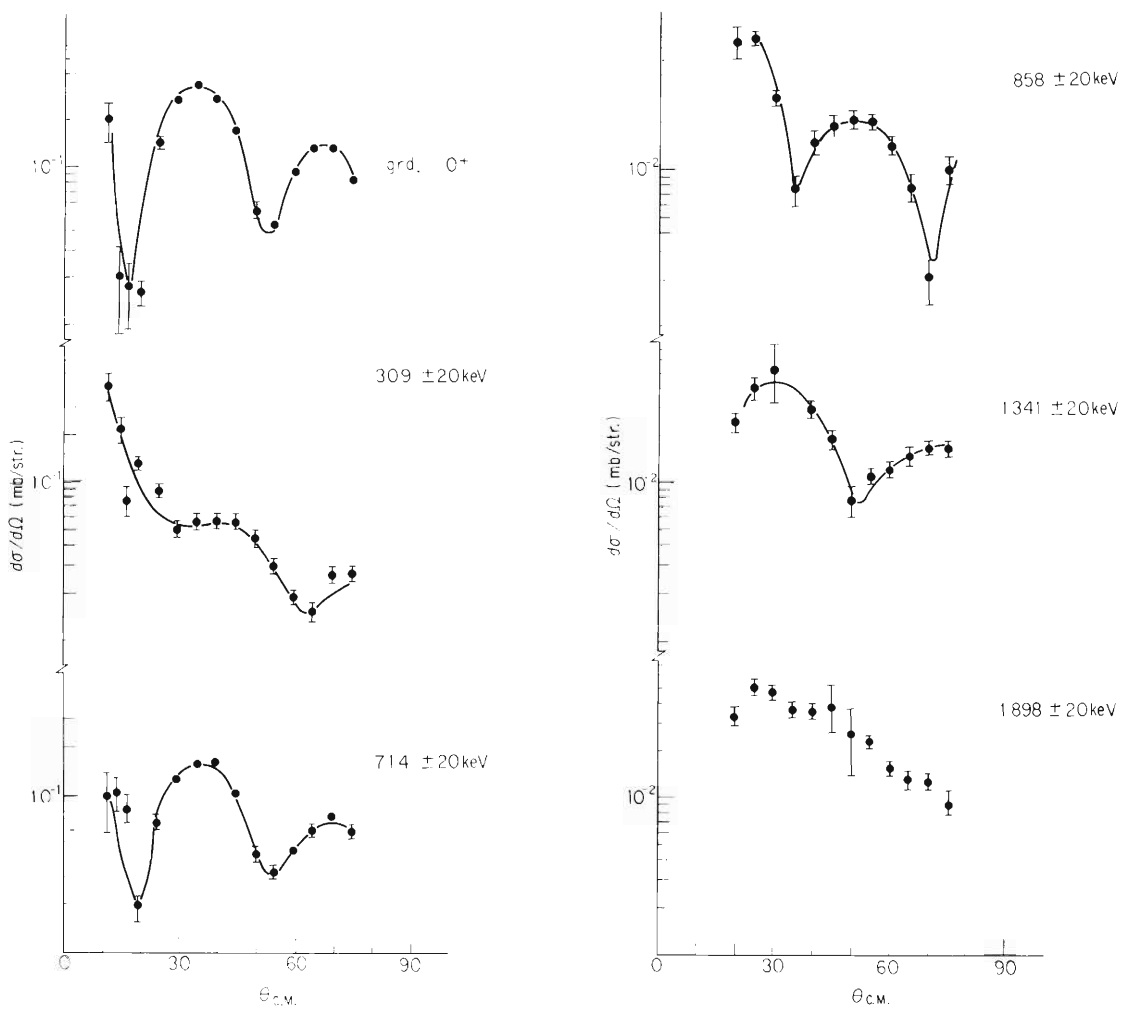

Fig. 1. Angular distributions for the transitions leading to the first six states seen in the reaction ^{100}Mo (t,p) ^{102}Mo. The solid curves are drawn through the experimental data points as a guide to the eye.

evidence as a new deformed region near A ~ 100.[5] According to their work, the deformed region will begin from ^{102}Mo for the molybdenum isotopes. The investigation of the low-lying states of ^{102}Mo and ^{100}Mo will then give some useful information on the study of nuclear structure of molybdenum isotopes in connection with other experimental results. Measurements of differential cross sections of the ^{100}Mo (t,p) ^{102}Mo and ^{98}Mo (t,p) ^{100}Mo reactions have been done under these backgrounds.

The experimental technique has been described elsewhere.[6] A triton beam of 15.8 MeV from the cyclotron was used in the experiments.[7] Angular distributions of emitted protons were obtained with a ΔE-E counter-telescope having semiconductor detectors.* Six peaks were observed corresponding to the low-lying states of ^{102}Mo, that is, 0, 309, 714, 858, 1341, and 1898 keV excitations. The uncertainty in the Q values is $\pm$20 keV due to the energy resolution. The angular distributions for these levels are shown in Fig. 1. The ground and 714 keV states are strongly excited, showing the same angular distribution pattern. These angular distributions are also similar to those of L=0 transition of (t,p) reactions in this mass region and energy ranges. Then, the excited 0^+ state at about 700 keV is also found in ^{102}Mo nucleus. Figure 2 shows the low-lying states of molybdenum isotopes for comparison. It is of interest that no excited 0^+ states are observed in $^{92, 94, 96}$Mo in contrast with the 0^+ states at about 700 keV in $^{98, 100, 102}$Mo. Blair et al. have reported that several 0^+ states above the ground state were observed in $^{92, 94, 96}$Zr, though there is no 0^+ state observed up to an excitation energy of 3.2 MeV in ^{98}Zr.[10] Since the neutron numbers of ^{100}Mo are equal to those of ^{98}Zr, the low-lying states excited by (t,p) reaction are expected to be in resemblance between them. Figure 3, however, shows very different spectrum except for the level positions of 3^- states. This difference in the low-lying states is to be ascribed to the two-proton addition. The differential cross sections of 0^+ states in ^{100}Mo and ^{102}Mo observed at 35° are as follows:

grd. (0^+) ---------- 440-μb/str.
700 keV (0^+) ---------- 80-μb/str.
} for ^{100}Mo,

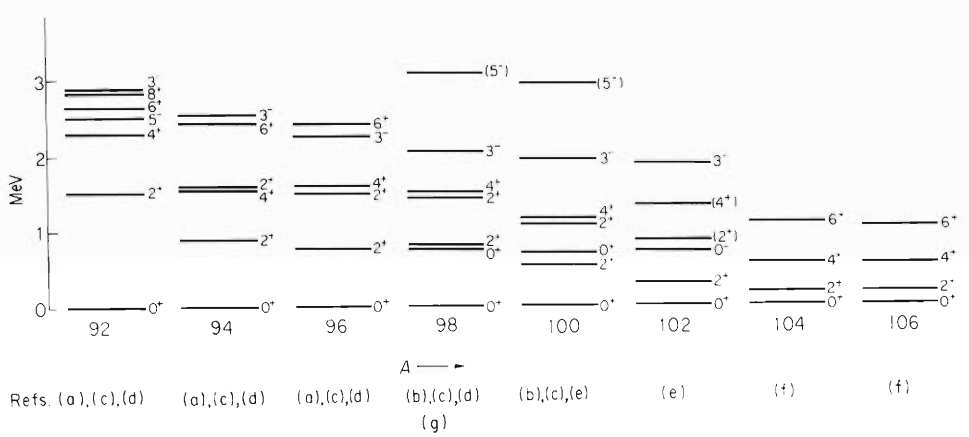

(a) : (p,p') experiment, Ref. 8).
(b) : (p,p') experiment, Ref. 4).
(c) : (α,α') experiment, Ref. 9).
(d) : (p,t) experiment, Ref. 3).
(e) : (t,p) experiment, present results.
(f) : fission fragment, Ref. 5).
(g) : γ transition, Ref. 1).

Fig. 2. Level schemes of even molybdenum isotopes.

* Surface barrier detectors obtained from ORTEC INC.

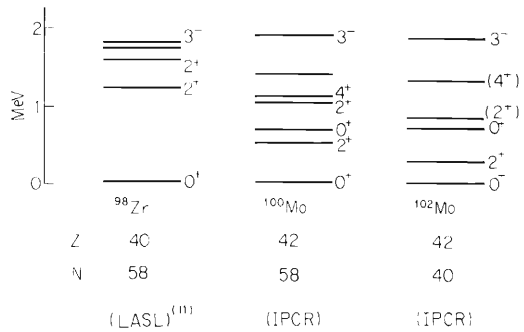

Fig. 3. Level schemes of ^{98}Zr, ^{100}Mo and ^{102}Mo.

grd. (0^+) ---------- 340-μb/str.

714 keV (0^+) ---------- 160-μb/str.

} for ^{102}Mo .

In order to investigate the sensitivity of the transition strengths to the mixing of configuration, DWBA calculations are performed including $2d_{5/2}$, $2d_{3/2}$, $3s_{1/2}$, $1g_{7/2}$, $1h_{11/2}$, $2f_{7/2}$, and $1h_{9/2}$ neutron shells. The form factors for the DWBA calculations are obtained by the harmonic oscillator wave function joining smoothly with a tail of the correct decaying wave function, the Hankel function. The QRPA (quasi-particle random phase approximation) was used for the calculation of phonon states. The optical potential parameters used in the distorted wave calculation are given in Table 1. Preliminary results of the DWBA analyses for the ground (0^+), 309 keV (2^+) and 1859 keV (3^-) states are shown in Fig. 4. They give quite good fitting for the experimental results. Any good fits for the experimental angular distributions of 858 keV and 1341 keV states, however, cannot be obtained from the present calculations of the form factors.

Since there is a close resemblance in the experimental angular distributions between the 309 keV and 858 keV states, the spin-parity of the 858 keV state may be assigned to 2^+. The angular distribution of the 1341 keV state has no resemblance to the other ones. Considering the systematics of the level schemes of ^{98}Mo and ^{100}Mo, the 858 keV and 1341 keV states of ^{102}Mo may be assigned to 2^+ and 4^+, respectively. On the one hand, however, the 1080 keV (2^+) and 1150 keV (4^+) states of ^{100}Mo excited by inelastic scattering of protons [4] could not be found by any observable cross section in the present (t,p) reaction, but the 858 keV and 1341 keV states of ^{102}Mo were excited by the (t,p) reaction as show in Fig. 1. Considering this behavior and the differences in the cross sections leading to the 0^+ states, a nuclear structure of ^{102}Mo may be somewhat different from ^{100}Mo.

Table 1. Optical parameters calculated with an automatic parameter search computer code "SEARCH" [1].

	V (MeV)	r_o (F)	a_o (F)	W (MeV)	r_i (F)	a_i (F)	r_c (F)
Triton	173.5	1.22	0.730	30.45[a]	1.22	0.868	1.25
Proton	49.3	1.27	0.825	20.3[a]	1.32	0.468	1.25

a-Saxon derivative well

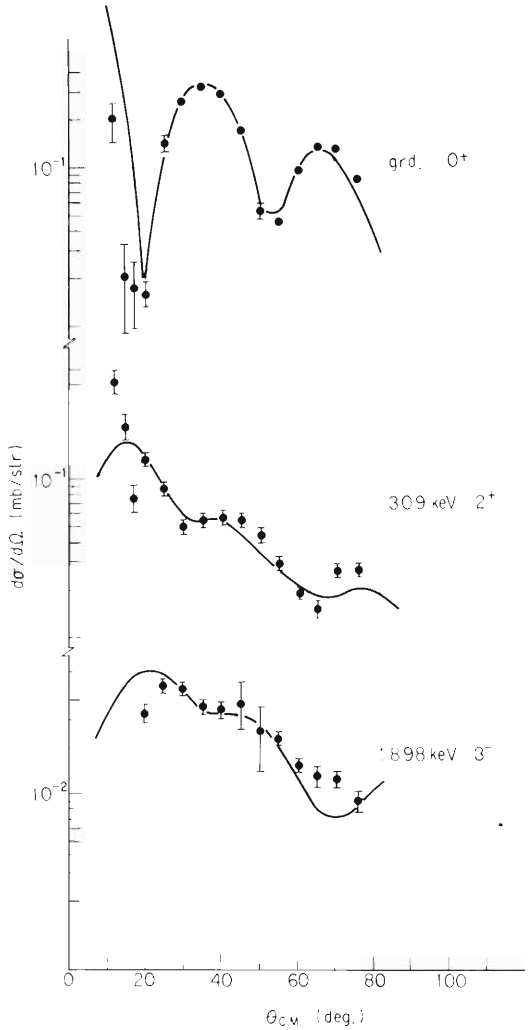

Fig. 4. Angular distributions for the transitions which are fitted with L = 0, L = 2 and L = 3 predictions of DWBA.

References

1) K. Hubenthal, E. Monnand, and A. Moussa: Nucl. Phys., A128, 577 (1969).
2) K. R. Evans and F. Ajzenberg Selove: Phys. Rev., 165, 1327 (1968).
3) H. Taketani et al.: to be published.
4) Y. Awaya et al.: to be published.
5) E. Cheifetz, R. C. Jared, S. G. Thompson, and J. B. Wilhelmy: Phys. Rev. Letters, 25, 38 (1970).
6) S. Takeda, K. Matsuda, Y. Awaya, N. Nakanishi, T. Wada, M. Odera, and I. Kohno: IPCR Cyclotron Progr. Rep. 3, 25 (1969); M. Odera, S. Takeda, and I. Kohno: ibid., 4, 29 (1970).
7) I. Kohno, A. Shimamura, I. Sakamoto, T. Tonuma, S. Takeda, N. Nakanishi, K. Matsuda, K. Koda, and T. Hamada: ibid., 4, 11 (1970).
8) T. Wada et al.: to be published.
9) K. Matsuda et al.: to be published.
10) A. G. Blair, J. G. Beery, and E. R. Flynn: Phys. Rev. Letters, 22, 470 (1969).
11) T. Wada: Reports of I.P.C.R., 46, 21(1970).

4-3. The ^{27}Al (^{3}He, p) ^{29}Si Reaction at 21.89 MeV

N. Nakanishi, S. Takeda, Y. Awaya, and K. Matsuda

Measurements of differential cross sections of the ^{27}Al (^{3}He,p) ^{29}Si reaction were done again under the same conditions as in the previous experiment[1] except that a set of solid state detectors was changed.

Emitted protons were detected by a ΔE-E solid-state counter telescope in both experiments. In the previous experiment the counter was composed of a 300 μm (ΔE-counter) and two 3000 μm (E-counter) totally depleted Li-drifted Si-detectors, and therefore we were afraid of an influence from dead layers between two detectors. Proton spectra obtained in the previous experiment show the depression at the energy region corresponding to about 26 MeV. A Q-value of the reaction to the ^{29}Si ground state is of 12.3 MeV energy, and thus 26 MeV protons correspond to the excitated states at an energy of 8 MeV. Unfortunately the levels excited through the (^{3}He,p) reaction are relatively small in the vicinity of excitation energy 8 MeV and it is not

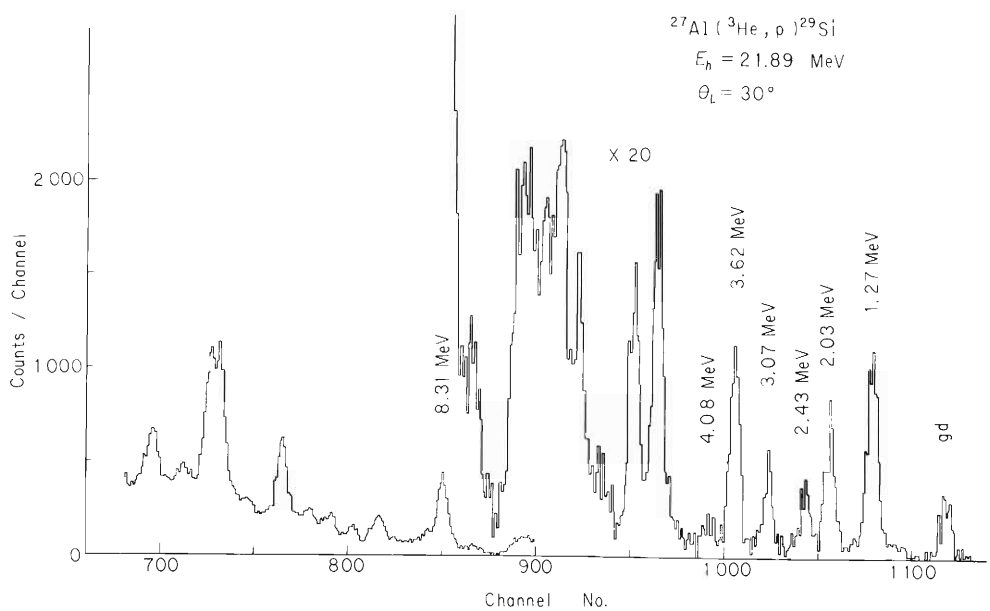

Fig. 1. Spectrum of emitted protons by the reaction ^{27}Al (^{3}He, p) ^{29}Si.

Table 1. Optical-model potential for the ^{27}Al (^{3}He, ^{3}He) ^{27}Al elastic scattering.

V	W_{vol}	r	a	r'	a'	X^2
145.6	24.9	1.05	0.749	1.40	0.982	42.7
190.2	21.2	1.14	0.599	1.37	1.286	50.5

rare in the (^{3}He,p) reaction that the differential cross sections corresponding to low-lying levels decrease rapidly with scattering angles so the influence is not distinguishable.

From the above view point we repeated the same measurements using an E-counter which was a 5000 μm Li-drifted Si detector. Fig. 1 shows a typical spectrum of emitted protons. It is seen that an analogue level of the ^{29}Al ground state at an excitation energy of 8.31 MeV is excited strongly.[2] Angular distributions of several low-lying levels[3] are shown in Fig. 2.

Analysis on the reaction will be done in the future. Incidentally the optical-model parameters of ^{3}He elastic scattering are summarized in Table 1, and the angular distribution are shown in Fig. 3. Optical-model parameters was obtained using an automatic search code.[4]

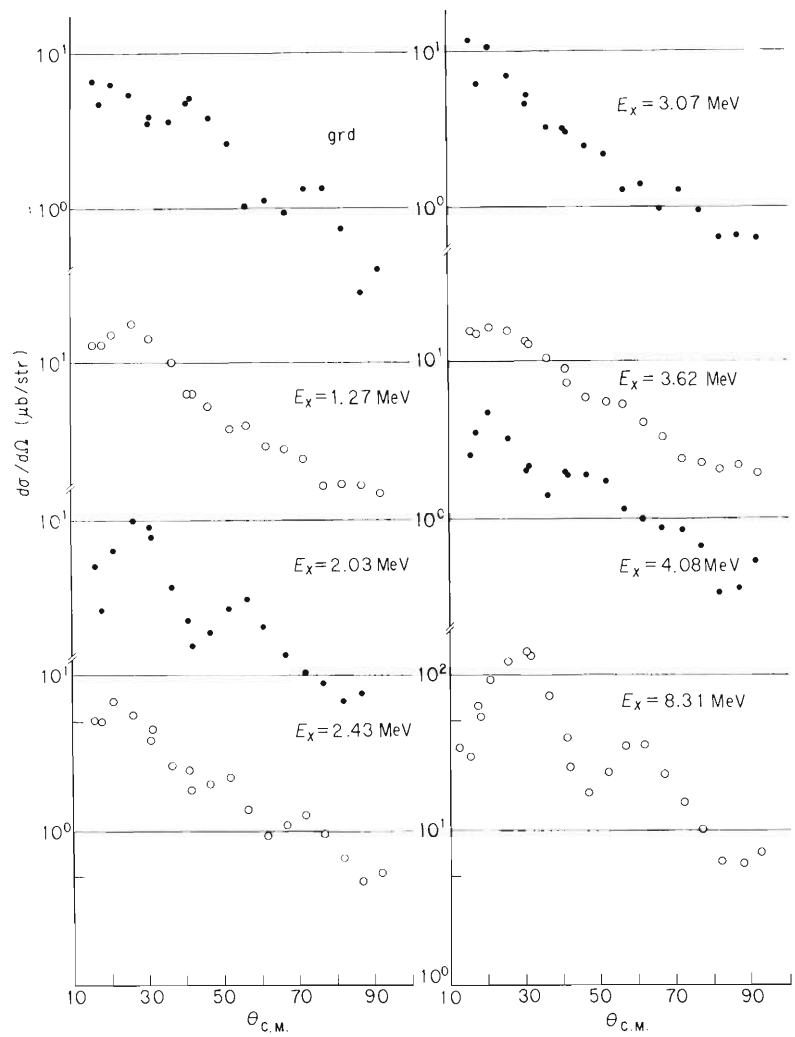

Fig. 2. Angular distributions for low-lying levels of ^{29}Si.

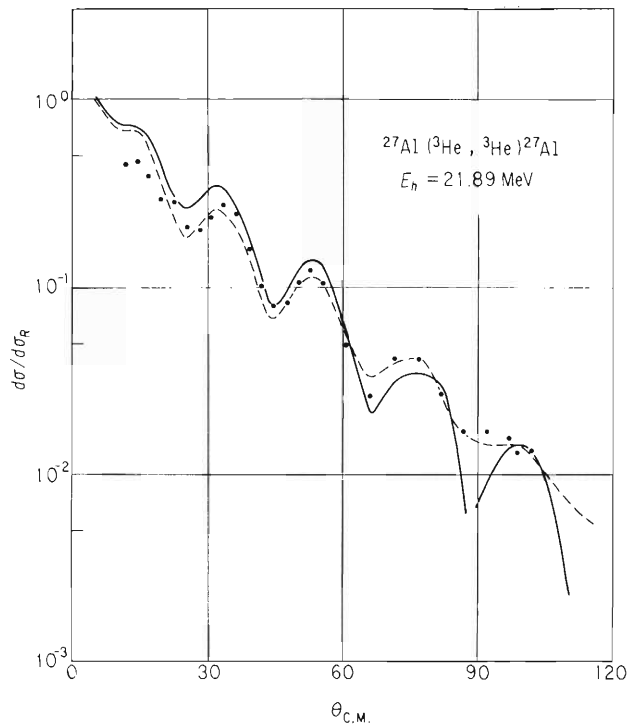

Fig. 3. Differential cross section ratio of elastically scattered ^{3}He particles by ^{27}Al. A broken line and a solid line give predicted differential cross section ratios corresponding to the potential families I and II, respectively.

References

1) N. Nakanishi, S. Takeda, T. Wada, Y. Awaya,and K. Matsuda: IPCR Cyclotron Progr. Rep., 2, 74 (1968).
2) L. Meyer-Schützmeister et al.: Phys. Rev., 187, 1210 (1969).
3) P.E. Endt and C. Van der Leun: Nucl. Phys., A105, 1 (1967).
4) T. Wada: IPCR Cyclotron Progr. Rep., 2, 87 (1968).

4-4. Elastic Scattering of Alpha Particles from Even-Mass Molybdenum Isotopes

K. Matsuda, N. Nakanishi, Y. Awaya, and S. Takeda

Angular distributions of alpha particles elastically and inelastically scattered of even mass molybdenum isotopes were measured at the incident energy of 30.87 MeV. Preliminary results were already described in Ref.1). It will be necessary to analyze systematically the elastic scattering data in order to perform the DWBA analysis of inelastic scattering data in detail. Therefore the angular distributions have been re-measured over a wider angular range that is between 16 degrees and 72 degrees in the C.M. system. Experiments have been done under the same condition as in the previous ones for each isotope. Ratios of measured elastic scattering to Rutherford scattering cross sections are shown with dots in Fig. 1.

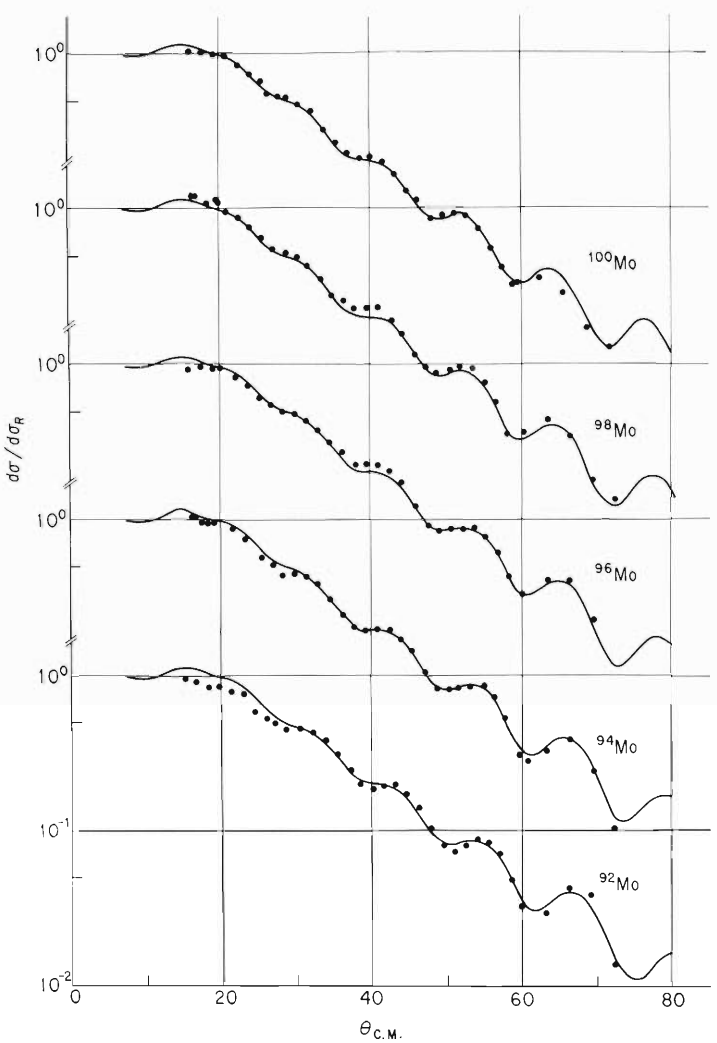

Fig. 1. Differential cross section ratio of elastic scattering to Rutherford scattering. Experimental data are shown with dots. Solid lines give predicted curves by optical model.

Optical-model analysis has been made using an automatic search code.[2] An optical potential form-factor is of Woods-Saxon type. The Coulomb potential is of a uniformly charged sphere type and the radius parameter r_c is fixed at 1.3 fm. A few criteria are introduced in searching optical model parameters. (1) Values of χ^2 should be as small as possible under the condition that fluctuation between each isotope would not be very large. (2) Geometrical parameters of the real and imaginary parts are equal to each other and moreover common to all isotopes. (3) The isobaric dependence of potential depth V and W_{vol} will show a smooth variation.

Table 1. Optical-model parameters.

	Real potential V (MeV)	Imaginary potential of volume type W (MeV)	χ^2-value	Recommended normalization constant
^{100}Mo	186.91	26.90	1.88	0.997
^{98}Mo	186.40	26.45	2.20	0.950
^{96}Mo	185.86	26.09	2.24	0.993
^{94}Mo	185.42	25.62	2.24	1.049
^{92}Mo	184.91	25.17	6.60	1.051

Geometrical parameters are fixed as follows: Radius parameter of optical potential r = 1.396 fm, diffuseness parameter a = 0.562 fm, Coulomb radius parameter r_c = 1.3 fm.

In the first step, four parameters V, W_{vol}, r and a were searched to give the best fit to each of the isotopes, and averaged geometrical parameters $\bar{r}$ and $\bar{a}$ were obtained from five r's and a's, respectively. The parameters, $\bar{r}$ and $\bar{a}$, were used for all isotopes. In the second step, the trend of variation of each of the parameters V and W_{vol} was examined to get a smaller χ^2-value using fixed parameters $\bar{r}$, $\bar{a}$ and r_c for each isotope. In the last step, the four parameters V, W, $\bar{r}$ and $\bar{a}$ were searched by the trial and error method according to the above criteria for all isotopes.

Optical-model parameters obtained are given in Table 1 and predicted differential cross section ratios are shown in Fig. 1 with solid curves. If fluctuations of potential depth V and W_{vol} are neglected, the values of χ^2 can be obtained as about 2 except ^{100}Mo and ^{92}Mo isotopes. Particularly, for ^{92}Mo isotope a comparable value with others is not obtained, and is not improved by normalization. The DWBA analysis is now in progress.

References

1) K. Matsuda, Y. Awaya, N. Nakanishi, and S. Takeda: IPCR Cyclotron Progr. Rep., 4, 38 (1970).
2) T. Wada: ibid., 2, 87 (1968).

4-5. The Manual of the Code for the Form Factor Computation of the Two-Nucleon Transfer Reaction

S. Yamaji

This is a brief account of the code to calculate the form factor of the two-nucleon transfer reaction such as (^{3}He,p), (t,p), (^{3}He,n), and (α,d). The expression of the form factor and the outline of the code are given in the Ref. 1) and details about the method to prepare the input data will be given elsewhere.[2] The characteristic points of this code are as follows:

(1) Two different treatments are available about the inducing interaction

a) The interaction between the outgoing and the captured particles is approximated as that acting between the center-of-masses of both particles. This treatment was first formulated by Glendenning[3] which is called "cluster" in this code.

b) The interaction is treated without above approximation, i.e., as a sum of two-body interactions between nucleons in the outgoing and captured particles. This treatment was first formulated by Lin and Yoshida,[4] which is called "micro".

(2) Three different treatments are available about the bound state of each nucleon in the captured particle

a) The bound state of each nucleon is a harmonic oscillator wave function.

b) The form factor of the internal region is obtained by the method (a), and that of the external region is a bound Coulomb wave function adjusted to the separation energy of the captured particle. Both wave functions are smoothly joined by varying the matching radius.

c) The bound state of each nucleon is a wave function solved in a given Woods-Saxon well.

(3) The form factor of the (α,d) reaction can be calculated as well as those of the (^{3}He,p), (t,p) and (^{3}He,n) reactions

Using the expression $A^{(n,N)}_{\ell sj}$, 1) the form factor $F_{\ell sj}(r)$ for the zero-range DWBA calculation is given in the following form.

$$F_{\ell sj}(r) = \sum_{n,N} A^{(n,N)}_{\ell sj} \; R_{N1}(r).$$

As we made mistakes in the Ref. 1), the following corrections must be done:

a) $\delta \rightarrow \frac{1}{\sqrt{2}}\delta$ in the expression of Ω_b.

b) $D(s) = \begin{cases} \{-1 + 1.5(B+H)\}/\sqrt{2} & \text{for } s = 1 \\ \{1 - 0.5(B+H)\}/\sqrt{2} & \text{for } s = 0. \end{cases}$

c) $\beta^4 \rightarrow B^2$ in the expression of C_n for "zero-range" and "micro".

If we use the form factor $F_{\ell sj}(r)$ obtained in this code into the DWBA 1 or DWBA 2* codes, we obtain $\sigma^{DWBA}_{\ell sj}(\theta)$. The absolute value of the differential cross section $\sigma_{\ell sj}(\theta)$ in a unit mb/str is related to $\sigma^{DWBA}_{\ell sj}(\theta)$ as follows.

$$\sigma_{\ell sj}(\theta) = \frac{(2J_B + 1)}{(2J_A + 1)(2s_a + 1)} \frac{1}{5.093 \times 10^3} \sigma^{DWBA}_{\ell sj}(\theta).$$

References

1) S. Yamaji: IPCR Cyclotron Progr. Rep., 2,83 (1968).
2) S. Yamaji: Sci. Papers I.P.C.R., 65, 79 (1971)
3) N. K. Glendenning: Ann. Rev. Nucl. Sci., 13,191 (1963); Phys. Rev., 137, B102 (1965).
4) C. L. Lin and S. Yoshida: Progr. Theor. Phys., 32,885 (1964).

* T. Udagawa, H. Yoshida, K. Kubo, and G. Yamaura: Code INS-DWBA 1; M. Kawai, K. Kubo, and G. Yamaura: Code INS-DWBA 2.

4-6. The Spin-Flip Probability in the ^{92,94}Mo (p, p′) Reaction

T. Wada, H. Kamitsubo, S. Motonaga,
Y. Chiba, T. Fujisawa, and M. Koike*

In the (p,p′) reaction, the cross section (σ), polarization (P), asymmetry (A) and spin-flip probability (S) can be expressed as follows:

$$\sigma = (\sigma_{++} + \sigma_{--} + \sigma_{+-} + \sigma_{-+})/2$$

$$P = (\sigma_{++} + \sigma_{+-} - \sigma_{-+} - \sigma_{--})/2\sigma$$

$$A = (\sigma_{++} + \sigma_{-+} - \sigma_{+-} - \sigma_{--})/2\sigma$$

$$S = (\sigma_{+-} + \sigma_{-+})/2\sigma,$$

where the subscripts for the σ mean the spin projection on Z-axis, which is the normal direction to the reaction plane. Plus sign (+) means spin up and minus (−) down. The left is for incident channel and right for final channel. In Fe region, the nuclei with N = 28 and N = 30 give different angular distributions of cross section and asymmetry,

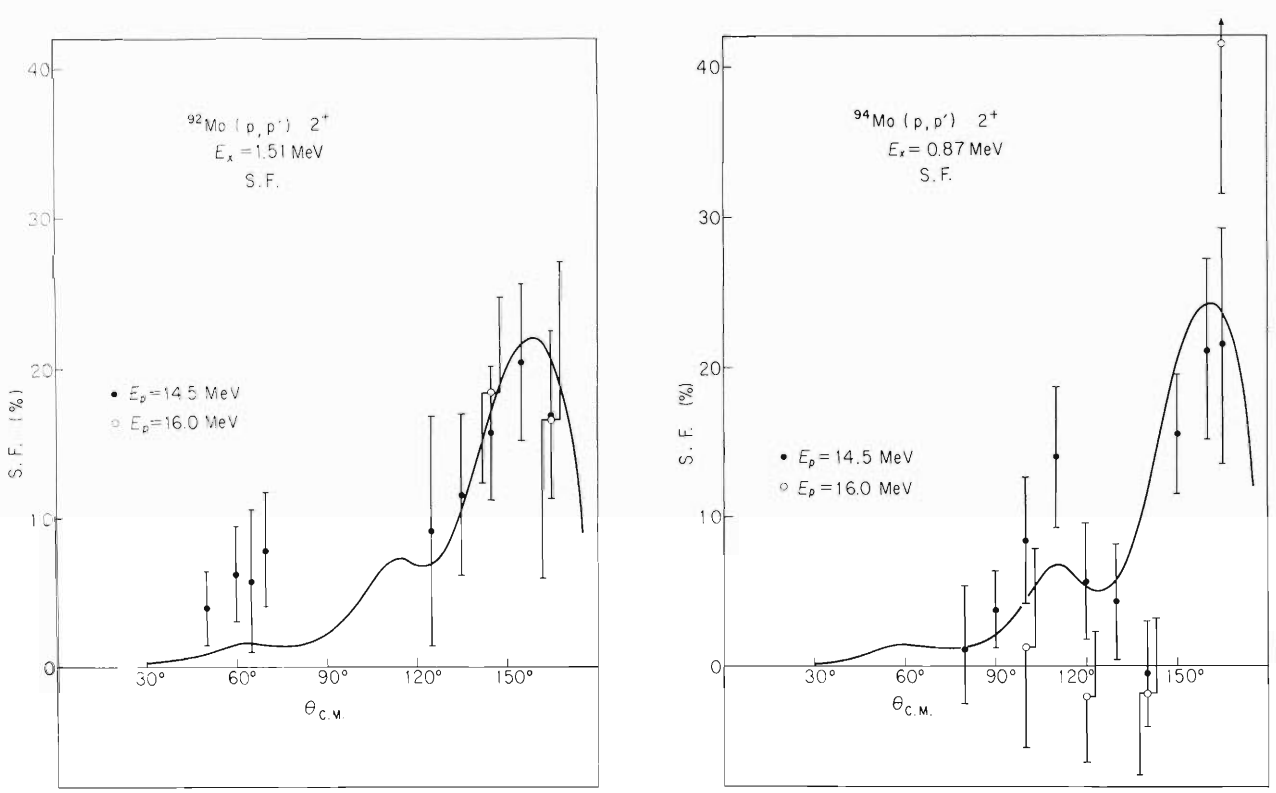

Fig. 1 Spin-Flip Probabilities in ^{92,94}Mo (p,p′) reaction. The solid lines are the results of collective model DWBA by Sherif code.[4]

* Institute for Nuclear Study, University of Tokyo.

but the angular distributions of spin-flip probability are not different so much. [1] For lighter or heavier nuclei, no good data of spin flip exist to investigate the dependence on the nuclear structure. The cross sections of (p,p′) for ^{92}Mo and ^{94}Mo give different angular distributions. [2] The spin-flip probabilities for these nuclei were also measured. The experimental conditions were the same as previously reported. [3] Fig. 1 shows the results. The ^{92}Mo nuclei has 50 neutrons and then the first 2^+ state is considered to be mainly composed of proton particle-hole states. But ^{94}Mo nucleus has the component of neutron states as well and then more collective characters. The angular distribution of cross section can be well predicted by collective model DWBA, but not so well for ^{92}Mo. But about the spin-flip probabilities, the DWBA predicts the result for ^{92}Mo fairly well. The angular distribution for ^{94}Mo has a sharp valley around $\theta_{c.m.} = 140^{o}$ which cannot be predicted by collective model DWBA. In order to see the resonance or compound effects the proton energy was increased to 16 MeV, but the valley was insisted. The major shell of proton and neutron differs in Mo region but not in Fe region. This may have some effects on the spin-flip probabilities. It may be interesting to measure the spin-flip probabilities for heavier nuclei.

References

1) D. L. Hendrie: Phys. Rev., 186, 1188 (1969).
2) T. Wada et al.: IPCR Cyclotron Progr. Rep., 3, 42 (1969).
3) S. Kobayashi et al.: J. Phys. Soc. Japan, 29, 1 (1970).
4) H. Sherif and J. S. Blair: Phys. Letters, 26B, 489 (1968).

4-7. Spin Flip in the Inelastic Scattering of ^{3}He on ^{12}C

T. Fujisawa, S. Motonaga, H. Kamitsubo,
Y. Chiba, and T. Wada

Spin flip probabilities of ^{3}He-particles in the reaction ^{12}C (^{3}He, $^{3}He'$) $^{12}C^{*}$ (4.43 MeV) were measured at an incident energy of 34.7 MeV. The experiment was carried out by the particle-γ correlation method that has been proposed first by Schmidt,[1] and the detail of the apparatus has been already reported.[2] The spin flip probability was measured in order to study the spin orbit term of the optical potential of ^{12}C for ^{3}He-particle. The study of optical potential has been done concerning elastic scattering[3] and the depth of the spin-orbit potential was selected to fit the experimental data at backward angles. The same potential gives the spin flip probability shown in Fig. 1. It was calculated by DWBA with the full-Thomas type distortion of spin-orbit potential proposed by Sherif and Blair.[3] The potential that has been determined in order to fit the elastic scattering cross sections does not predict the measured spin flip probabilities and the potential of which the spin orbit potential depth is 2.5 MeV gives better agreement.

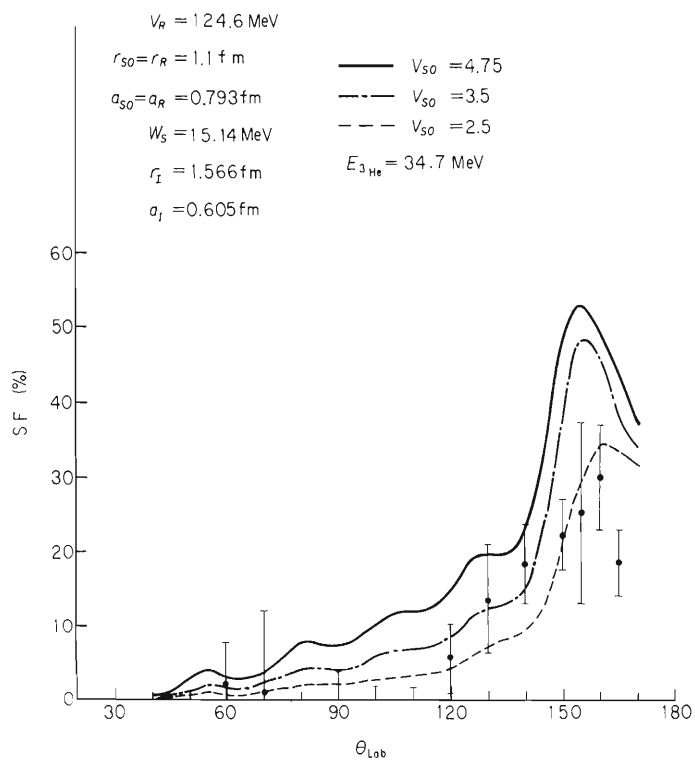

Fig. 1. The angular distribution of spin flip probabilities of ^{3}He for ^{12}C and the prediction of DWBA.
A spin orbit potential of which depth is 4.75 MeV gave the good agreement for elastic scattering crosssections.

References

1) F. H. Schmidt, R. E. Brown, J. B. Gerhart, and W. A. Kolasinski: Nucl. Phys., 52, 353 (1964).
2) S. Kobayashi, S. Motonaga, Y. Chiba, K. Katori, A. Stricker, T. Fujisawa, and T. Wada: J. Phys. Soc. Japan, 29, 1 (1970).
3) T. Fujisawa, H. Kamitsubo, S. Motonaga, K. Matsuda, F. Yoshida, H. Sakaguchi, and K. Masui: IPCR Cyclotron Progr. Rep., 4, 46 (1970).
4) H. Sherif and J. S. Blair: Phys. Letters, 26B, 489 (1968).

5. NUCLEAR PHYSICS
Nuclear Spectroscopy

5-1. The Level Structures of Light Even Strontium Isotopes Produced by $^{70,72,74,76}Ge(^{12}C, 4n)$ Reactions

T. Inamura, S. Nagamiya, A. Hashizume, and Y. Tendow

Since Talmi and Unna[1] studied the level structure of nuclei in the vicinity of ^{90}Zr, the ^{88}Sr nucleus has been taken as an inert core in the shell model calculations for this region. It is, however, still an open problem to what extent the matrix elements of the effective interaction in proton configurations can reproduce those in the corresponding neutron configurations. Recently Kitching et al.[2] have indicated that seniority of the $g_{9/2}$ neutron shell remains a useful quantum number within a few mass units of the ^{88}Sr core. In addition, the simple shell theory of Talmi and Unna[1] has been proved to be successful in describing the ^{86}Sr level structure.[3] On the other hand, Zaitseva et al.[4] have suggested that the level structure of ^{84}Sr may be interpreted as the quasi-rotational band, although they did not find positive parity states with spin 6 or higher. Thus, it is of value to investigate experimentally how low-lying high-spin states appear in ^{84}Sr; its level structure is expected to be similar to that of ^{92}Mo in the framework of the simple shell theory.[1]

It is also of interest to study the level structure of ^{78}Sr which should manifest the existence or non-existence of a magic gap at N = 40 (or 38). In this connection it might provide a useful information to study the level systematics of ^{80}Sr, ^{82}Sr and ^{84}Sr isotopes.

(1) ^{84}Sr

Gamma-rays from the $^{76}Ge(^{12}C, 4n)^{84}Sr$ reaction were identified by excitation functions, and time distributions were measured in the nanosecond region. No isomeric states in ^{84}Sr were found having half-lives of more than 5 ns; if the level structure of ^{84}Sr was analogous to that of ^{92}Mo, the 8^+ isomer should be observed in the present measurement. Anisotropies $W(45^\circ)/W(90^\circ)$ of these γ-rays were also measured with

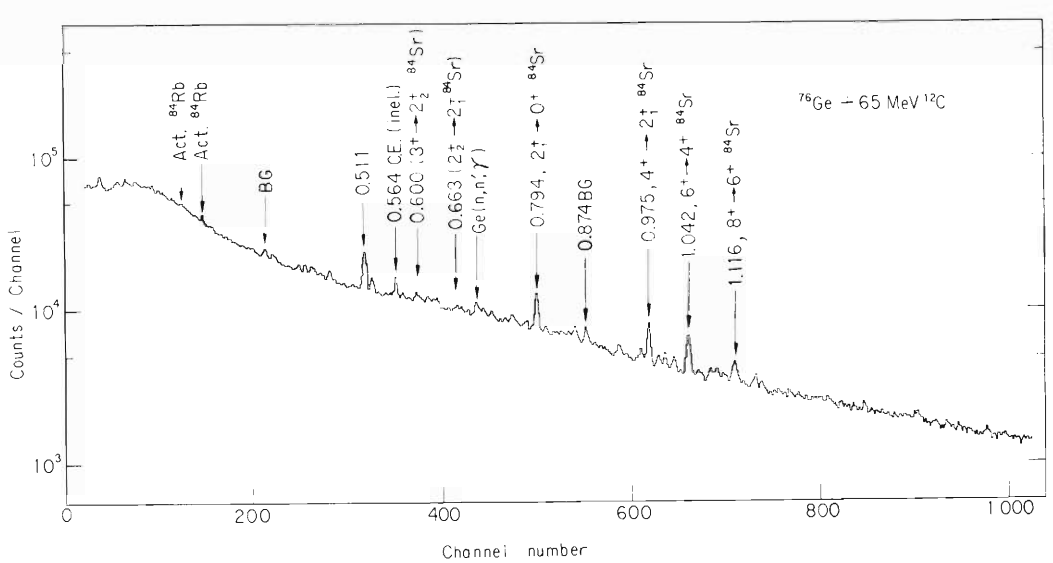

Fig. 1. Gamma-rays observed in the ^{76}Ge + 65 MeV ^{12}C reaction.

Table 1. Gamma-rays identified as belonging to the $^{76}Ge(^{12}C, 4n)^{84}Sr$ reaction.

E_γ(MeV)	Relative intensity	Anisotropy $W(45^o)/W(90^o)$	Assignment
0.794	100 ± 7	1.36 ± 0.14	$2_1^+ \rightarrow 0^+$ *
0.975	96 ± 14	1.34 ± 0.13	$4^+ \rightarrow 2_1^+$ *
1.042	87 ± 9	1.39 ± 0.14	$6^+ \rightarrow 4^+$
1.116	56 ± 9	1.35 ± 0.14	$8^+ \rightarrow 6^+$

* Ref. 4)

respect to the beam direction, and the 1.042 and 1.116 MeV γ-rays were found to be of E2 by referring to the anisotropies of the 0.794 ($2_1^+ \rightarrow 0^+$), and 0.975 ($4^+ \rightarrow 2_1^+$) MeV γ-rays already known.[4] In Fig. 1 is shown the energy spectrum of γ-rays observed in the bombardment of the ^{76}Ge target with 65 MeV ^{12}C ions by using a 30 cc Ge(Li) detector. Relative intensities and anisotropies of these γ-rays are listed in Table 1; γ-ray energies have been determined within less than 1 keV. The ordering of the two new E2 transitions of 1.042 ($6^+ \rightarrow 4^+$) and 1.116 ($8^+ \rightarrow 6^+$) MeV has been made according to intensity.

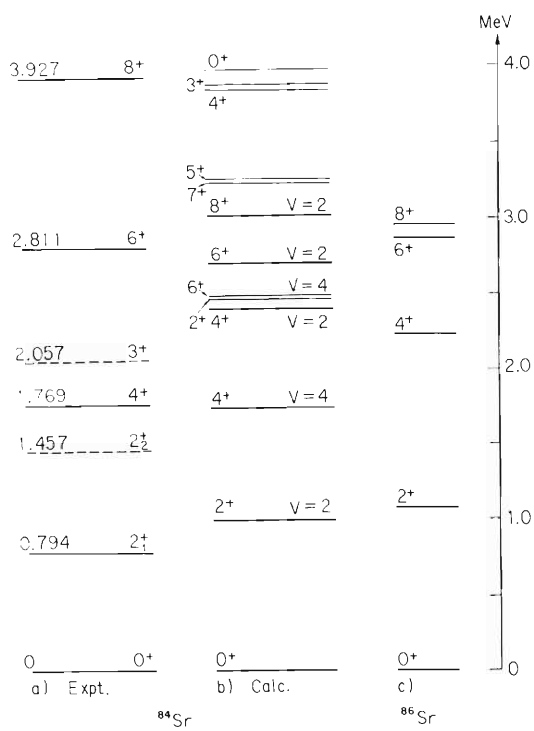

Fig. 2. Level scheme of ^{84}Sr a) observed in the present experiment, b) calculated by the shell model and c) excited levels of ^{86}Sr used in the determination of the effective interaction.

On the basis of the present results low-lying excited levels in ^{84}Sr have been constructed as shown on the left of Fig. 2. The placement of the 6^+ level at 2.811 MeV and of the 8^+ level at 3.927 MeV has revealed the marked quasi-rotational band structure of ^{84}Sr, which strongly supports the suggestion of Zaitseva et al.[4)]

We have tried to interpret the ^{84}Sr level structure observed in the framework of the shell model, introducing seniority up to v = 4 in the $(p_{1/2})^{-2}$ $(g_{9/2})^{-2}$ and $(g_{9/2})^{-4}$ neutron configurations. We used the energies of the positive parity states up to spin 8 in ^{86}Sr[3)] in the determination of the effective interaction. Results of our calculation are shown in Fig. 2. On the right the states of ^{86}Sr are presented for comparison. The present calculation, as can be seen from Fig. 2, has ended in a complete failure in describing the 8^+ level at 3.927 MeV. Consequently, it can be concluded that, so long as the ^{88}Sr nucleus is assumed to be an inert core, the ^{84}Sr level structure cannot be interpreted by the shell model calculation.

The observed quasi-rotational band of ^{84}Sr is likely to be interpreted by introducing the p-n interaction,* in view of the fact that the $7/2^+$ ground state of ^{83}Sr seems to be an anomalous coupling state.[5)]

(2) ^{78}Sr, ^{80}Sr, and ^{82}Sr

Targets of ^{70}Ge, ^{72}Ge and ^{74}Ge were bombarded with 68 MeV ^{12}C ions and γ-rays from the (^{12}C, 4n) reactions were studied. The choice of the beam energy was made in view of Q-values of the relevant reactions which are a little larger than the Q-value of ^{76}Ge(^{12}C, 4n) reaction. For identification of γ-rays from these (^{12}C, 4n) reactions the data on Kr isotopes[6)] were very helpful because these isotopes could be produced by the decay of the (^{12}C, p3n) reaction products as well as by the (^{12}C, 2p2n) or (^{12}C, α) reactions.

Gamma-rays identified as belonging to ^{78}Sr, ^{80}Sr,and ^{82}Sr are listed in Tables 2, 3,and 4, respectively. Transition assignments were made on the basis of the observed anisotropies and relative intensities. Time analyses of these γ-rays were also made, and no isomers were found as in the case of ^{84}Sr. The cascade relation of $4^+ \rightarrow 2^+ \rightarrow 0^+$ was checked by a Ge(Li) - NaI(Tl) coincidence measurement in each case.

The level structures of ^{78}Sr, ^{80}Sr,and ^{82}Sr proposed on the basis of the present preliminary results are shown in Fig. 3. These nuclear structures appear to be of quasi-rotational bands. Therefore, a magic gap at N = 40 (or 38) is not likely to exist.

Table 2. Gamma-rays identified as belonging to the ^{70}Ge(^{12}C, 4n)^{78}Sr reaction.

E_γ(MeV)	Relative intensity	Anisotropy $W(45^o)/W(90^o)$	Assignment
0.505	100 ± 11	1.32 ± 0.12	$2^+ \rightarrow 0^+$
0.758	60 ± 7	1.28 ± 0.15	$4^+ \rightarrow 2^+$
0.827	53 ± 7	1.30 ± 0.17	$6^+ \rightarrow 4^+$

* Private communication.

Table 3. Gamma-rays identified as belonging to the $^{72}Ge(^{12}C, 4n)^{80}Sr$ reaction.

E_γ(MeV)	Relative intensity	Anisotropy $W(45^o)/W(90^o)$	Assignment
0.455	100 ± 6	1.27 ± 0.06	$2^+ \rightarrow 0^+$
0.666	67 ± 5	1.31 ± 0.09	$4^+ \rightarrow 2^+$
0.860	52 ± 7	1.36 ± 0.17	$6^+ \rightarrow 4^+$

Table 4. Gamma-rays identified as belonging to the $^{74}Ge(^{12}C, 4n)^{82}Sr$ reaction.

E_γ(MeV)	Relative intensity	Anisotropy $W(45^o)/W(90^o)$	Assignment
0.576	100 ± 6	1.10 ± 0.22	$2^+ \rightarrow 0^+$
0 756	100 ± 8	1.33 ± 0.27	$4^+ \rightarrow 2^+$
0.822	36 ± 5	1.49 ± 0.36	$(6^+ \rightarrow 4^+)$

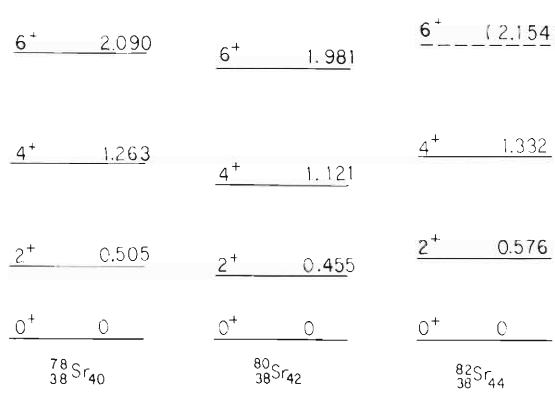

Fig. 3. Proposed level schemes of ^{78}Sr, ^{80}Sr and ^{82}Sr.

The authors are indebted to Dr. K. Ogawa, the University of Tokyo, for making the shell model calculations.

References

1) I. Talmi and I. Unna : Nucl. Phys., 19, 225 (1960).
2) J. E. Kitching, W. Darcey, W. G. Davies, W. McLatchie, and J. M. Morton : Phys. Letters, 32B, 343 (1970).
3) M. Ishihara, H. Kawakami, N. Yoshikawa, M. Sakai,and K. Ishii : ibid., 35B, 398 (1971).
4) N. G. Zaitseva, B. Kratsik, M. G. Loshchilov, G. Muziol, Chang Tkhan Min, and Kh. Shtrusnyi : Izv. Akad. Nauk, SSSR, Ser. Fiz. , 33, 1283 (1969).
5) R. C. Etherton, L. M. Beyer, W. H. Kelley, and D. J. Horen : Phys. Rev., 168, 1249 (1968).
6) E. Nolte, W. Kutschera, Y. Shida,and H. Morinaga : Phys. Letters, 33B, 294 (1970).

5-2. Magnetic Moment of the 8^+ State of ^{206}Po

S. Nagamiya, Y. Yamazaki, T. Nomura,
K. Nakai, and T. Yamazaki

At present, one of the most interesting problems in the study of nuclear magnetic moment is to check the additivity of g-factors between one-particle state and two-particle state, especially for high-spin states around doubly-closed shell regions. Since the magnetic moment is very sensitive to the wavefunction of the state, the study of additivity is a powerful approach for determining the configuration of the state of interest. Furthermore, it gives much information on the magnetic core polarization, the mesonic effect, and so on.

Recently, many high-spin isomeric states in the ^{208}Pb region have been found and identified, and the magnetic moments of such high-spin states have begun to be measured. The present study is one of our work in series in this region.[1)~3)] According to the studies by Yamazaki et al.[4)] and by Nagamiya and Inamura,[5)] the $(\pi h_{9/2}^2)$ 8^+ isomeric states have been systematically identified in even-A Po-isotopes with mass number A of 200 ~ 210 and half-life ranging from 100 to 400 ns. These 8^+ isomeric states are of particular interest for the study of the magnetic core polarization in the ^{208}Pb region especially of the effect of the polarization of neutron on the $\pi h_{9/2}$ orbital.

Measurement was made by the ordinary time-differential PAD method. The γ-rays following the ^{204}Pb (α, 2n) reaction, with E_α = 29 MeV, were detected by two NaI(T1) counters placed at angles 60 and 135°, and the time distributions of the

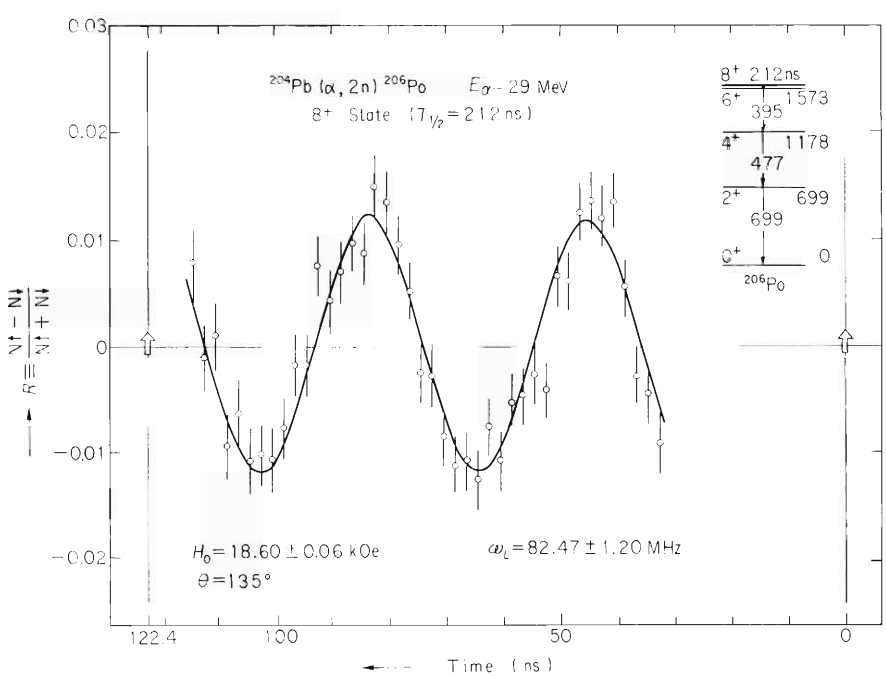

Fig. 1. Levels of ^{206}Po and a typical example for the time-differential pattern for the 8^+ isomeric state. Solid line is the best-fit. Since the setting of the strength of the applied field is not so good, the amplitude is reduced to one-fifth of that at a matched field and the phase changes largely.[6)]

Table 1. Summary of the observed g-factors of the $(\pi h_{9/2}^2)\ 8^+$ states of even-A Po-isotopes.

Nuclei	I^π	$T_{1/2}$ (ns)	g_{exp}	$g_{Schmidt}$	δg_{core} [f]	δ_{LS} [g]	δg_{vib}	g_{cal}	$g_{exp} - g_{cal}$
^{210}Po	8^+	110 ± 10 [a]	0.925 ± 0.010 [c]	0.583	0.174	0.009	0	0.766	0.159 ± 0.010
^{208}Po	8^+	380 ± 10 [a]	0.915 ± 0.006 [d]	0.583	0.183	0.009	−0.003	0.772	0.143 ± 0.006
^{206}Po	8^+	212 ± 5 [b]	0.926 ± 0.016 [e]	0.583	0.185	0.009	−0.003	0.774	0.151 ± 0.016
^{209}Bi	$9^-/2$	stable	0.9067	0.583	0.180	0.009	0	0.772	0.135

a) Ref. 4).
b) R. Broda et al. : Dubna Report, E6-5197 (1970).
c) Ref. 1).
d) Ref. 3).
e) Present result. (Note that corrections of the Knight shift are not made for the values c), d), and e) listed above, since the diamagnetic correction is estimated (Ref. 7)) to compensate the Knight shift correction)
f) Calculated by the formula of Arima and Horie (Ref. 8))by use of the calculated V_j^2 values for the neutron orbitals (L. S. Kisslinger and R. A. Sorensen : Mat. Fys. Medd. Dan. Vid. Selsk., 27, No. 16 (1953)).
g) Calculated by the formula of Chemtob (Ref. 9)).

$6^+ \rightarrow 4^+$ (395 keV) plus $4^+ \rightarrow 2^+$ (477 keV) composite peak were measured. A magnetic field of 18.60 ± 0.06 kOe was applied up and down perpendicularly to the beam-detector plane. Level scheme of ^{206}Po together with a typical result are shown in Fig. 1, from which we obtain

$$g\,(8^+;\ ^{206}\mathrm{Po}) = 0.926 \pm 0.016.$$

In this measurement we have unfortunately set the strength of the magnetic field larger than the matched strength at which the n = 3 stroboscopic resonance occurs.[6] Thus, the observed amplitude shown in Fig. 1 is highly reduced into one-fifth of that expected at the matched field. Because the present value includes a relatively large error, we are planning to remeasure this g-factor again.

Nevertheless, the present value is still meaningful for the rough theoretical discussion. In Table 1 we list the present result together with the known g-factors of the $(\pi h_{9/2}^2)\ 8^+$ states of ^{208}Po and ^{210}Po. Theoretically calculated g-factors, g_{cal}, derived from

$$g_{cal} = g_{Schmidt} + \delta g_{core} + \delta g_{LS} + \delta g_{vib}$$

are listed in the 9th column of the table, where $g_{Schmidt}$ is the Schmidt value, δg_{core} is the correction to g-factor due to the magnetic core polarization,[8] δg_{LS} is the correction due to the two-body L·S force[9] and δg_{vib} is the correction due to the surface vibration of the Pb core.[10] The order of magnitudes of the latter two are not so large.

From the table the followings are to be noted:

(1) Both values of g_{exp}'s and g_{cal}'s are almost constant for all measured values, whereas,

(2) the absolute values of $(g_{cal} - g_{exp})$'s are still large for all the cases.

The fact (1) implies that the 8^+ state of ^{206}Po certainly has the $\pi h_{9/2}$ configuration, and in addition that the effect of the magnetic core polarization of the neutron on the proton g-factor is small, which is in good agreement with theoretical predictions.[8]

As for the fact (2), it can be explained, as is well known,[2),11)] by the anomalous g_ℓ factor of the proton.

References

1) T. Yamazaki, T. Nomura, T. Katou, T. Inamura, A. Hashizume, and Y. Tendow: Phys. Rev. Letters, 24, 317 (1970).
2) T. Yamazaki, T. Nomura, S. Nagamiya, and T. Katou : ibid., 25, 547 (1970).
3) S. Nagamiya, T. Nomura, and T. Yamazaki : Nucl. Phys., A159, 653 (1970).
4) T. Yamazaki : Phys. Rev., C1, 290 (1970).
5) S. Nagamiya and T. Inamura : Nucl. Phys., A182, 84 (1972).
6) J. Christiansen, H. E. Mahnke, E. Recknagel, D. Riegel, G. Weyer, and W. Witthuhn : Phys. Rev. Letters, 21, 554 (1968) ; S. Nagamiya and K. Sugimoto : Osaka University Report, OULNS, 69-3 (1969).
7) F. D. Feiock and W. R. Johnson : Phys. Rev. Letters, 21, 785 (1968).
8) A. Arima and H. Horie : Progr. Theor. Phys., 12, 623 (1954).
9) M. Chemtob : Nucl. Phys., A123, 449 (1969).
10) A. Bohr and B. R. Mottelson : Mat. Fys. Medd. Dan. Vid. Selsk., 27, No. 16 (1953).
11) S. Nagamiya and T. Yamazaki : Phys. Rev., C4, 1961 (1971).

5-3. Magnetic Moment of the Lowest 6^+ State in ^{42}Ca

T. Nomura, T. Yamazaki, S. Nagamiya, and T. Katou

The lowest 6^+ state in ^{42}Ca is considered to be mainly of $\nu f_{7/2}^2$ configuration. In fact the recent measurement of E2 transition probability between the 6^+ and 2750 keV 4^+ states has proved very pure character of this configuration.[1] Then the g-factor of the 6^+ state is expected to give the g-factor of the $0f_{7/2}$ neutron in its two-particle state and thus to throw a new light on the g-factor of the ^{41}Ca ground state ($g(7/2^-: {}^{41}Ca) = -0.4556$) which is known to deviate largely from the Schmidt value for the $0f_{7/2}$ neutron ($g_{sp} = -0.546$).

The g-factor of the 6^+ state has been measured with the time-differential perturbed angular distribution method. The experimental method has been fully described earlier.[2] The results are shown in Fig. 1 (a part of these results has been reported in Ref. 2)), from which we obtain

$$g(6^+ : {}^{42}Ca) = -(0.50 \,{}^{+0.02}_{-0.03})$$

It is a remarkable fact that the g-factor of the ^{42}Ca 6^+ state is closer to the Schmidt value for the $0f_{7/2}$ neutron than that of the ^{41}Ca ground state is. If we assume the wave function of the 6^+ state to be

$$0.99 f_{7/2}^2 + 0.13 f_{7/2} f_{5/2}$$

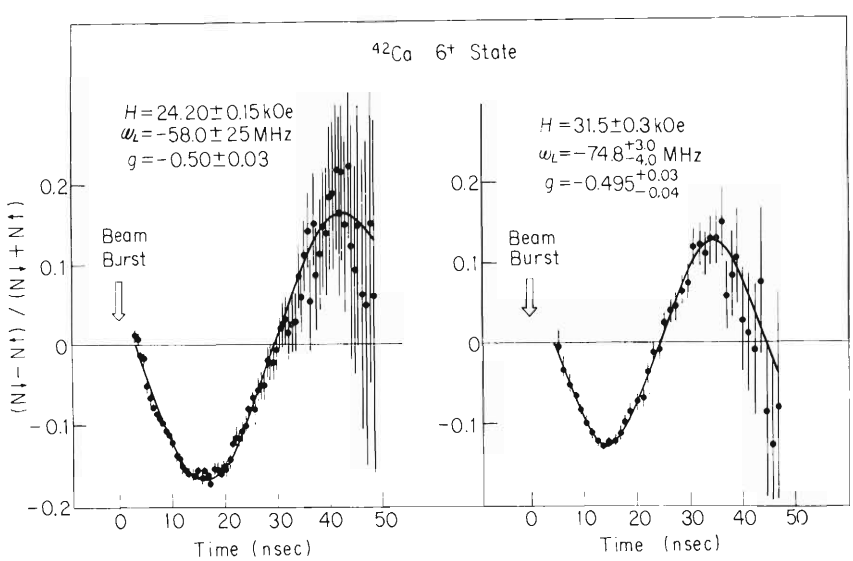

Fig. 1. Normalized time-differential patterns of the de-exciting gamma-rays from the 6^+ state in ^{42}Ca excited by the ^{40}Ca (α, 2p) ^{42}Ca reaction. A thick metallic Ca (natural) target was used. The data were taken at 135 degrees with respect to the beam direction. The solid curves show the best fits for $(N\downarrow - N\uparrow)/(N\downarrow + N\uparrow) = a^+ b \sin 2(W_M t + \theta)$, where W_M is the Larmor frequency and θ is the beam deflection angle due to the magnetic field.

as calculated by Kuo and Brown,[3] we can deduce the g-factor carried by the $0f_{7/2}$ neutron itself to be −0.57, which is nearly equal to the Schmidt value. The strong violation of the additivity of the effective magnetic moments for these states can be ascribed to the fact that a mixing of the core excited deformed states such as those given by Gerace and Green[4] is larger in the ^{41}Ca ground state than in the ^{42}Ca 6^+ state (see Table 1).

Table 1. The experimental g-factors for the $\nu f_{7/2}^n$ configuration in comparison with the theoretical estimates.

	$7/2^-(^{41}\mathrm{Ca})$	$6^+(^{42}\mathrm{Ca})$
Main Configuration	$f_{7/2}$	$f_{7/2}^2$
g_{exp}	-0.4556[a]	$-0.50\ ^{+0.02}_{-0.03}$[b]
g_{sp} (Schmidt estimate)	−0.546	−0.546
δg_{1st} (1st-order correction)		0.07
δg_{def} (correction due to the deformed states)[c]	0.13	0.02
g_{cal} $(= g_{sp} + \delta g_{1st} + \delta g_{def})$	−0.42	−0.46
$g(\nu f_{7/2})$[d]	−0.59	−0.59
δg_{2nd} (2nd-order correction)	0.08[e]	0.08[f]
g_{cal} $(= g_{sp} + \delta g_{1st} + \delta g_{2nd} + \delta g_{def})$	−0.34	−0.38
$g(\nu f_{7/2})$[d]	−0.67	−0.67

a) From Ref. 9). b) Present result.

c) Calculated for the wave functions given in Ref. 4) and Ref. 11).

d) g-Factor carried by the $0f_{7/2}$ neutron itself $(= g_{exp} - \Sigma \delta g)$.

e) Taken from Ref. 6).

f) The same value as for the $7/2^-$ state is assumed.

Table 2. The g-factors of $f_{7/2}$ proton and neutron.

	Theoretical		Empirical[a]
	Schmidt value	Single-particle value with $\delta g_\ell = 0.1\,\tau_z$	
$\nu f_{7/2}$	−0.546	−0.632	−0.67[b]
$\pi f_{7/2}$	1.655	1.741	1.76[c]
Sum	1.109	1.109	1.09

a) The g-factor carried by the $0f_{7/2}$ proton or neutron empirically deduced in the text.

b) Present result. c) Taken from Ref. 10).

If we take into account the correction due to the configuration mixing in the second-order perturbation theory,[5),6)] the empirical g-factor of the $0f_{7/2}$ neutron deduced from the present result falls outside the Schmidt limits. Recent empirical analysis[7)] shows that the orbital g-factor in a nucleus is enhanced by $0.1\,\tau_z$ (τ_z is +1 for proton and −1 for neutron), which agrees with theoretical consideration based on the mesonic exchange theory.[8)] The present result seems to support the anomaly of the g_ℓ-factor also in the ^{40}Ca region (see Table 2).

References

1) T. Nomura, C. Gil, H. Saito, T. Yamazaki, and M. Ishihara : Phys. Rev. Letters, 25, 1342 (1970).
2) T. Yamazaki, T. Nomura, T. Katou, and S. Nagamiya : IPCR Cyclotron Progr. Rep., 4, 74 (1970).
3) T. T. S. Kuo and G. E. Brown : Nucl. Phys., A114, 241 (1969).
4) W. J. Gerace and A. M. Green : ibid., A93, 110 (1967).
5) M. Ichimura and K. Yazaki : ibid., 63, 401 (1965).
6) H. A. Mavromatis et al. : ibid., 80, 545 (1966).
7) T. Yamazaki, T. Nomura, S. Nagamiya, and T. Katou : Phys. Rev. Letters, 25, 547 (1970) ; S. Nagamiya and T. Yamazaki : Phys. Rev., C4, 1961 (1971).
8) For example, H. Miyazawa : Progr. Theor. Phys., K, 6, 801 (1951).
9) E. Brun et al. : ibid., 9, 166 (1962).
10) K. Nakai et al. : Phys. Rev. Letters., 27, 155 (1971).
11) B. H. Flowers and L. D. Skouras : Nucl. Phys., A136, 353 (1969).

5-4. Decay of ^{87}Zr and ^{85}Zr

Y. Awaya, T. Katou, Y. Tendow,
A. Hashizume, and T. Hamada

The decay of ^{87}Zr and ^{85}Zr has been investigated to study the level structure of the neutron deficient yttrium nuclei systematically. The isotopically separated ^{86}Sr (NO_3) target was bombarded by ^3He particles from the cyclotron. The bombarding energy was 18.5 MeV for the $^{86}Sr(^3He, 2n)^{87}Zr$ reaction and 44 MeV for the $^{86}Sr(^3He, 4n)^{85}Zr$ one. The zirconium component was chemically separated by the solvent extraction.

The measurement of single spectrum of gamma-rays was made by using a 23 cm^3 Ge(Li) or an anti-Compton spectrometer which consists of the 23 cm^3 Ge(Li) and an annular type 6 inch × 6 inch NaI(Tl) longitudinally split by halves.[1] The gamma-gamma coincidence measurement was made by the 23 cm^3 Ge(Li) and a 3 inch × 3 inch NaI(Tl). The energy spectra of positrons and conversion electrons were obtained by using a Si(Li) detector with a depletion layer of 3 mm. The spectrum of X-rays was measured by a Si(Li) detector specially designed for X-ray measurements.[2] The preliminarily obtained gamma-ray spectrum of ^{87}Zr was reported previously by the authors.[3]

(1) Zr-87

Though the spin-parity of the ground state of ^{87}Zr has not been assigned, the value of $9/2^+$ is most plausible from the standpoint of the shell model. In this mass region, many nuclei have an isomer which originates in the shell configuration of the 2pl/2 and the lg 9/2 orbits. If the ^{87m}Zr ($J\pi = 1/2^-$) exists during the measurement, it should be taken into account when the decay scheme is discussed. But as the X-rays of the zirconium could not be found definitely about an hour after the bombardment and in most cases the measurement was begun at that time, out present study is considered to concern only the ground state decay of ^{87}Zr.

The half-life of ^{87}Zr has been determined to be 104.0 ± 0.5 min from the decay of the positron spectrum and to be 103 ± 4.5 min from the decay of the 1.227 MeV gamma-ray, whereas the previously reported value is 1.6 h.[4] The maximum energy of the positrons has been estimated to be 2.28 ± 0.05 MeV. The spectrum of gamma-rays obtained by the anti-Compton spectrometer is shown in Fig. 1. The energies of gamma-rays assigned to ^{87}Zr and their relative intensities are listed in Table 1. In addition to the gamma-rays listed in Table 1, the 200 keV, 921 keV, 1147 keV, 1590 keV, 2434 keV, and 2720 keV gamma-rays were also detected but because of their weak intensities the definite assignment was difficult. The results of gamma-gamma coincidence measurement are summarized in Table 2. The cascade gamma-rays were also checked from the comparison of the single gamma-ray spectrum with that obtained by the anti-Compton spectrometer with the source on the Ge(Li) detector. In the latter case, the intensity of gamma-rays which coincide with any others decreases relatively to those in the single spectrum. The coincidence measurement between the positrons (and conversion electrons) and the gamma-rays which coincide with the annihilation gamma-ray was made, but because of the low counting rate, a definite result as to the end-point energy of each positron branch has not been obtained yet in the present stage. In this meas-

Table 1. Gamma-rays of ^{87}Zr.

Previous work[5]		Present work	
E_γ (keV)	I_γ (rel.)	E_γ (keV)	I_γ (rel.)
		611 ± 1	4 ± 1
		633 ± 1	2 ± 1
771 ± 2	4 ± 2	772 ± 1	8 ± 1
793 ± 2	20 ± 3	794 ± 1	10 ± 2
		797 ± 1	6 ± 2
		836 ± 1	2 ± 1
973 ± 2	6 ± 3	973 ± 1	4 ± 1
		1024 ± 1	28 ± 2
		1048 ± 1	2 ± 1
1160 ± 2	7 ± 3	1159 ± 1	8 ± 1
1202 ± 3	12 ± 5	1203 ± 1	5 ± 1
1210 ± 1	35 ± 3	1210 ± 1	33 ± 2
		1216 ± 1	3 ± 2
1228 ± 1	100	1227 ± 1	100
		1388 ± 1.5	3 ± 1
		1400 ± 1.5	4 ± 1
		1410 ± 1.5	1 ± 0.5
		1657 ± 2	3 ± 1
		1692 ± 1.5	1 ± 0.5
1806 ± 2	5 ± 2	1808 ± 1.5	3 ± 1
1820 ± 2	3 ± 2	1821 ± 1.5	3 ± 1
		1857 ± 1.5	2 ± 1
		1862 ± 1.5	1 ± 0.5
2165 ± 5	3 ± 2	2172 ± 2	2 ± 1
2183 ± 5	3 ± 2	2183 ± 1.5	3 ± 1
2220 ± 3	10 ± 2	2222 ± 1.5	9 ± 2
2615 ± 3	5 ± 1	2615 ± 1.5	3 ± 2
		2883 ± 2	2 ± 1.5

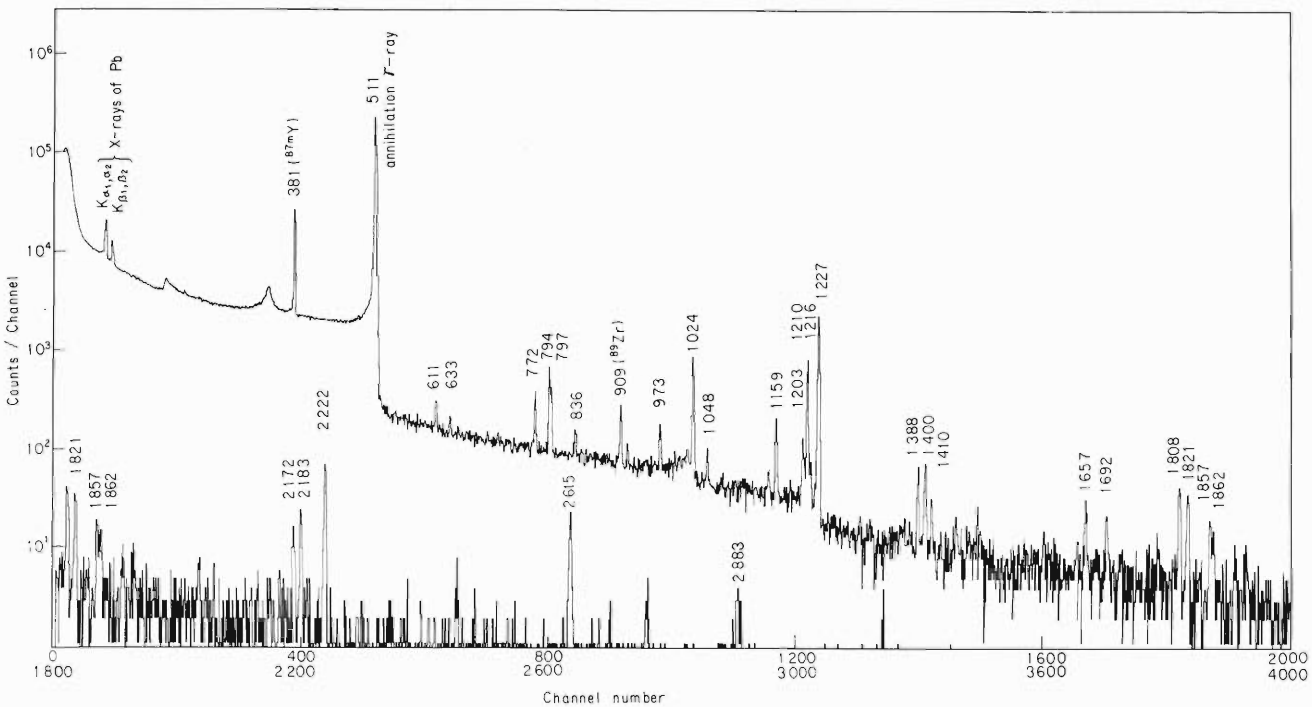

Fig. 1. The gamma-ray spectrum of ^{87}Zr. Energies are in keV.

Table 2. Results of the gamma-gamma coincidence.

Gate / $E\gamma$	511	730 ~ 780	760 ~ 840	940 ~ 1030	1030 ~ 1060	1110 ~ 1170	1180 ~ 1220	1220 ~ 1260	1350 ~ 1500
611	?						+		
772					+		+		+
794, 797	+			+	+		+	+	+
973			+				?		
1024	+	+	+	+	+	+	?		?
1048							?		
1203		+	+	?	?		?		+
1210, 1216	+								
1227	+			?	?				?
1388							+	?	
1400, 1410		+	+				+		
1693	+								
1808		+	+						
1857		+	+						

urement, however, the conversion electron of 345 keV was detected when the gate for the gamma-rays was opened at 710~820 keV. This suggests the existence of the transition of about 362 keV though the gamma-transition is too weak to be detected.

On the basis of the present results and the result of the $^{86}Sr(^{3}He, d)\ ^{87}Y$ reaction obtained by Maher et al.,[6] a tentative decay scheme of ^{87}Zr is proposed in Fig. 2. The spin-parities are based on the assignment of Ref. 6). On the analogy of ^{89}Y the spin-parity of the 1405 keV state and/or the 1591 keV state is considered to be $7/2^{+}$. A few

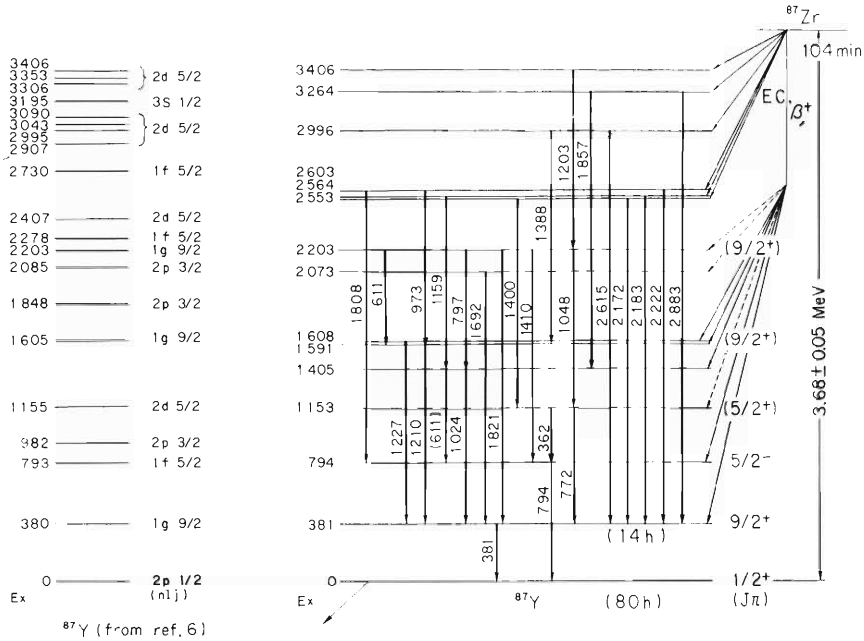

Fig. 2. The proposed decay scheme of ^{87}Zr. The levels excited by the ^{86}Sr (^{3}He, d) ^{87}Y[6] are also shown for comparison.

Table 3. Gamma-rays of ^{85}Zr.

From Ref. 9)		Present work	
E_γ (keV)	I_γ (rel.)	E_γ (keV)	I_γ (rel.)
265.8	7	265.9	6.6
		357.8	3.3
415.9	63	416.1	58
454.0	100	454.1	100
		621.7	2.2
		636.4	3.5
		781.6	7.8
		798.7	4.5
		1199.0	9.9
		1414.9	2.2
		1769.1	3.9

gamma-rays are not included in the decay scheme. Although the values of the transition energy differ by 1 keV or so from those of gamma-ray energy in Table 1 for some cases, the values in Table 1 are used in the decay scheme. In order to make the decay scheme more definite, the study is still in progress.

(2) Zr-85

Various half-lives of ^{85}Zr ranging from 6～8 min to 1.5 h have been reported[7),8)] based on observations of the activity of the daughter nuclide, ^{85}Y. Recently, Doron and Blann[9)] assigned three gamma-rays to ^{85}Zr and proposed a half-life of 7.7 ± 0.5 min. Their assignment was based on the measurements on three different heavy ion reaction products and their excitation functions.

In our experiment Zr isotopes of mass number from 85 to 89 were separated by the solvent extraction, and the measurement was started usually about 6 min after the end of bombardment. Many gamma-rays were assigned to ^{85}Zr and the half-life was determined to be 8.0 ± 0.5 min. The assignment was made on the basis of their decay periods. Energies and relative intensities of the gamma-rays are summarized in Table 3. In addition to the gamma-rays listed in Table 3, the 1720 keV, 1865 keV, 1920 keV, 1923 keV, 1993 keV, and 2127 keV gamma-rays were also detected, but a definite assignment was difficult because of their weak intensities. The gamma-ray spectrum of ^{85}Zr is shown in Fig. 3. The study is still in progress.

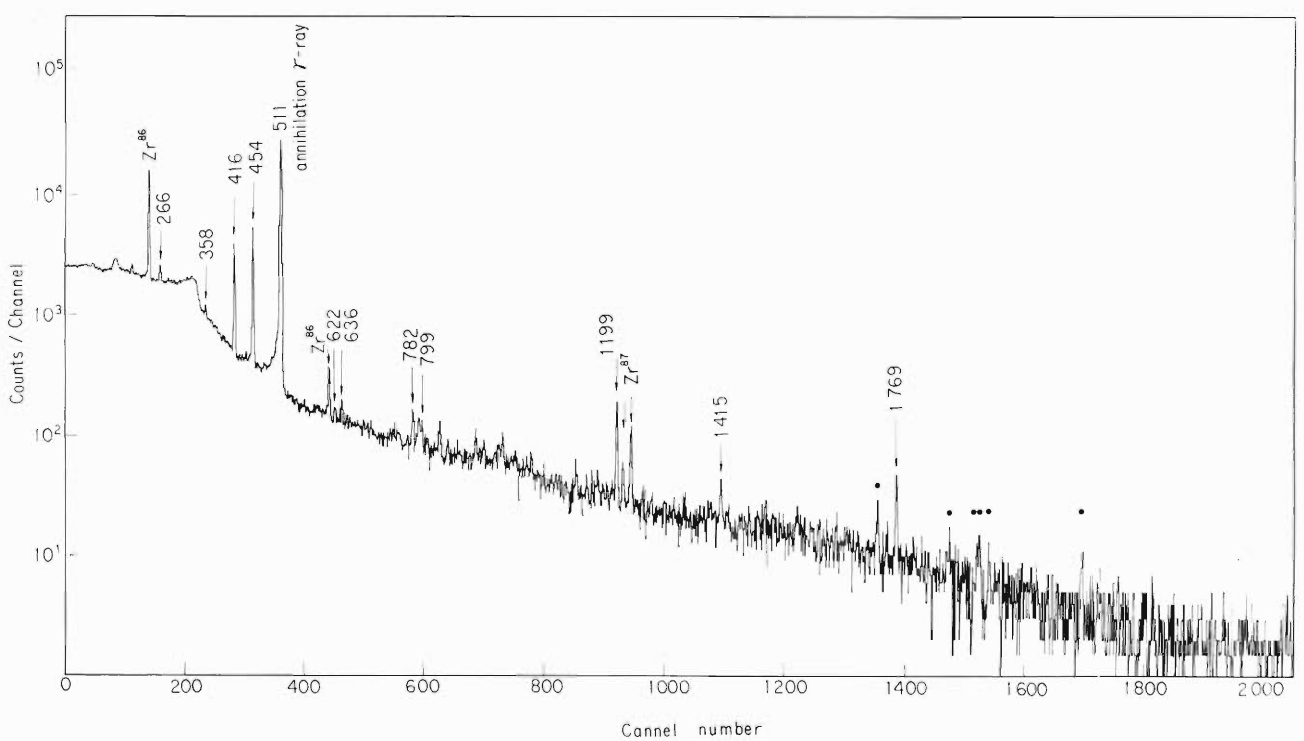

Fig. 3. The gamma-ray spectrum of ^{85}Zr. Energies are in keV.

References

1) M. Okano et al. : IPCR Cyclotron Progr. Rep., 2, 110 (1968).
2) M. Okano et al. : ibid., 5, 75 (1971).
3) Y. Awaya et al. : ibid., 2, 109 (1968).
4) C.M. Lederer et al. : "Table of Isotopes", John Wiley and Sons, N.Y., p. 222 (1967).
5) R. Arlt et al. : Contrib. Intern. Conf. Nucl. Struct., Dubna, p. 10 (1968).
6) J.V. Maher et al. : Phys. Rev., C3, 1162 (1971).
7) F.D.S. Butement and G.B. Briscoe : J. Inorg. Nucl. Chem., 25, 1699 (1969).
8) N.G. Zaitseva et al. : Sov. J. Nucl. Phys., 1, 273 (1965).
9) T.A. Doron and M. Blann : Nucl. Phys., A161, 12 (1971).

5-5. New Isomer in ^{148}Gd

A. Hashizume, Y. Tendow, T. Katou, and T. Inamura

In the course of an investigation of new isomeric states by the detection of delayed γ-rays between the natural beam bunches of the cyclotron, it has been found that an isomeric state exists in ^{148}Gd. Most of the features of the experimental method have been described in a previous report.[1] Essentially it consists of taking nanosecond timing distribution of the reaction γ-rays detected by a Ge(Li) detector.

A ^{147}Sm target enriched to 97.9 % and deposited on a 4 μm Mylar film and a target of natural isotope of La in a metallic form were bombarded by 20 to 45 MeV α-particles to induce (α, xnγ) reactions and 65 to 88 MeV nitrogen ions to induce (N, xnγ) reactions respectively. Figure 1 shows single γ-ray spectra from the former reaction for several bombarding energies. Figure 2 shows the relative excitation function for the γ-rays attributed to the (α, 3n) reaction (except 940 keV γ-rays). An excitation curve taken with a 786 keV γ-ray in Fig. 2 shows a very broad peak which is interpreted by the existence of two unresolved γ-rays, assuming that one of them gives a similar excitation curve to that of 940 keV. Normalizing the curve from 27.5 to 32.5 MeV of 940 keV to that of 786 keV, one obtains the dashed curve which gives the characteristic of (α, 3n) reaction. The energies and intensities of these γ-rays at 40 MeV bombarding energy is shown in Table 1.

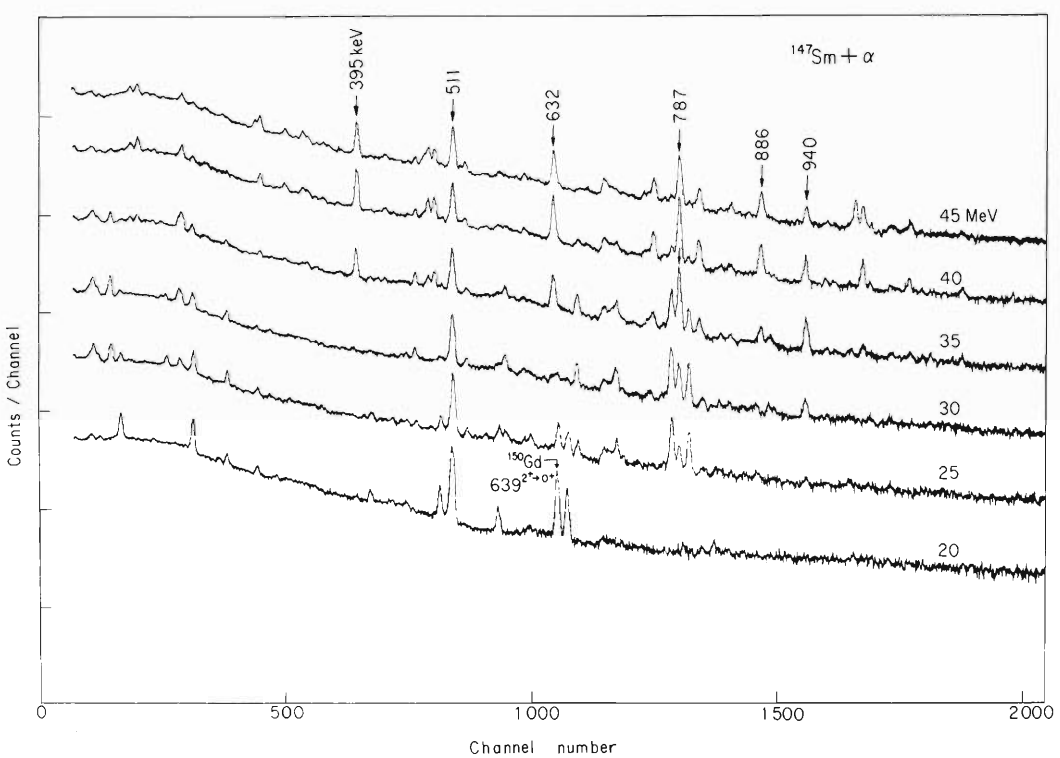

Fig. 1. Single γ-ray spectra from the ^{147}Sm (α, xn) reactions.

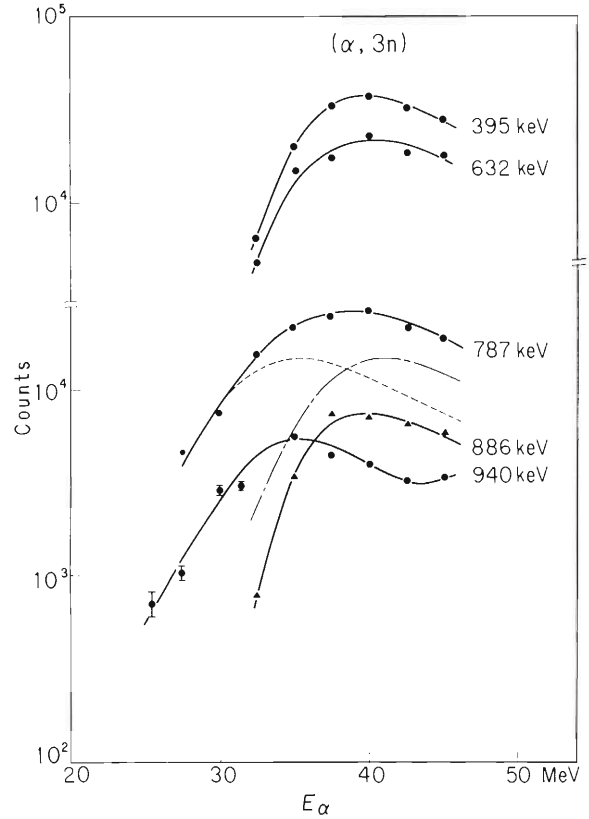

Fig. 2. Typical excitation curves for the ^{147}Sm (α, 3n) ^{148}Gd reaction.

Table 1. γ-ray intensities and anistropies.

E_γ (keV) ΔE	$I_\gamma \pm \Delta I$	$W(43^o)/W(90^o)$
394.9 ± 1.0	82 ± 17	1.36 ± 0.03
632.0 ± 1.0	101 ± 21	1.28 ± 0.02
784.3 ± 1.0	100	1.32 ± 0.02
882.9 ± 1.0	44 ± 9	1.30 ± 0.05

The γ-ray spectra from the reaction induced by the heavy ions are so complex that one could not distinguish clearly those γ-rays from (N, 5n) reaction. Though the most intensive ones observed in ^{147}Sm (α, 3n) reaction are also found when the incident energies of nitrogen ions were 80 and 85 MeV (Fig. 3). Figures 4 and 5 show prompt and delayed γ-ray spectra from the interested reactions. The decay curves of each delayed γ-rays are shown in Figs. 6 and 7. These curves were analyzed by the least square method using a program (UNIDEC) and the half-life was determined to be 16.2 ± 0.9 ns for the curves in Fig. 6 and 17.9 ± 2.5 ns for Fig. 7. Comparing the curves in Fig. 6 with those in Fig. 7 the ratios of intensities for delayed to prompt

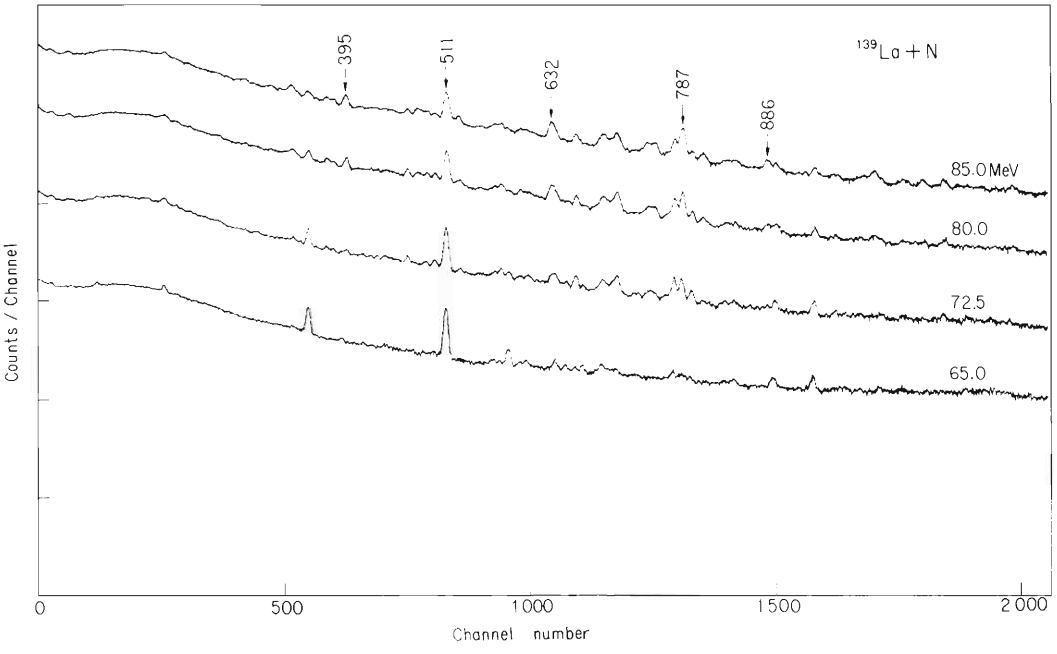

Fig. 3. Single γ-ray spectra from the ^{139}La (N, xn) reactions.

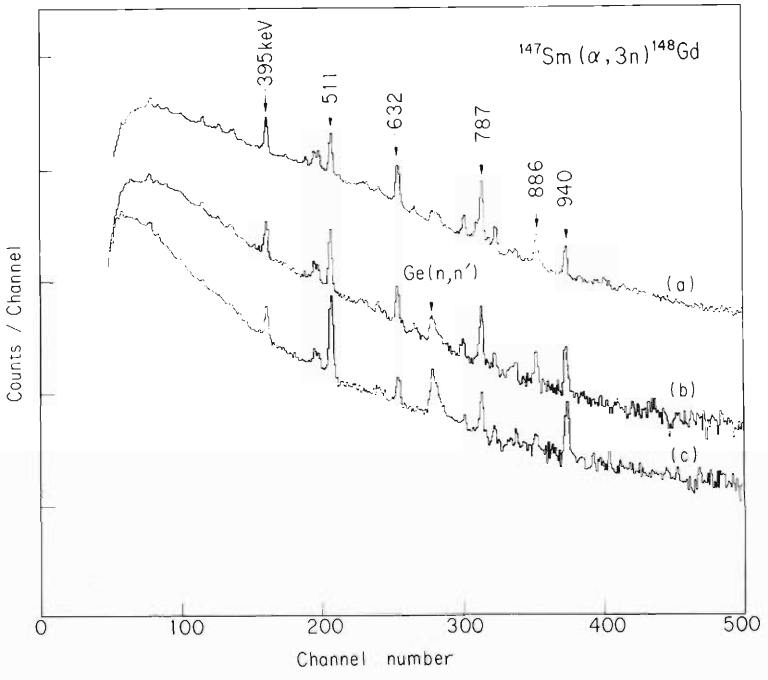

Fig. 4. Prompt and delayed γ-ray spectra observed in a ^{147}Sm + 38 MeV α reaction. Spectrum (a) shows prompt and spectra (b) and (c) show delayed (about 50 ns and 75 ns) γ-rays. The ordinate of each spectrum are relatively normalized.

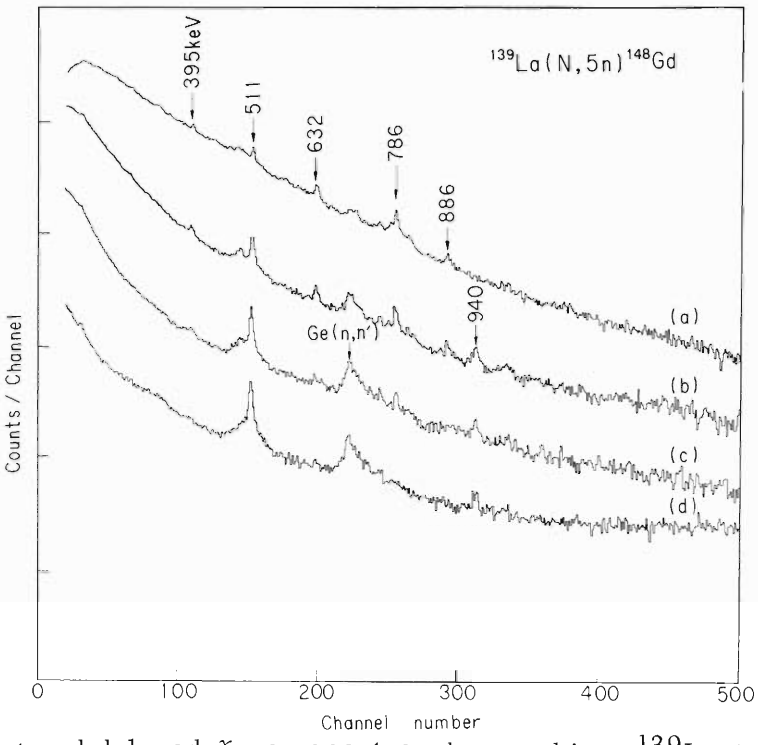

Fig. 5. Prompt and delayed γ-ray spectra observed in a ^{139}La + 87 MeV N reaction. Spectrum (a) shows prompt and spectra (b), (c) and (d) shows delayed (about 27, 54 and 81 ns respectively) γ-rays.

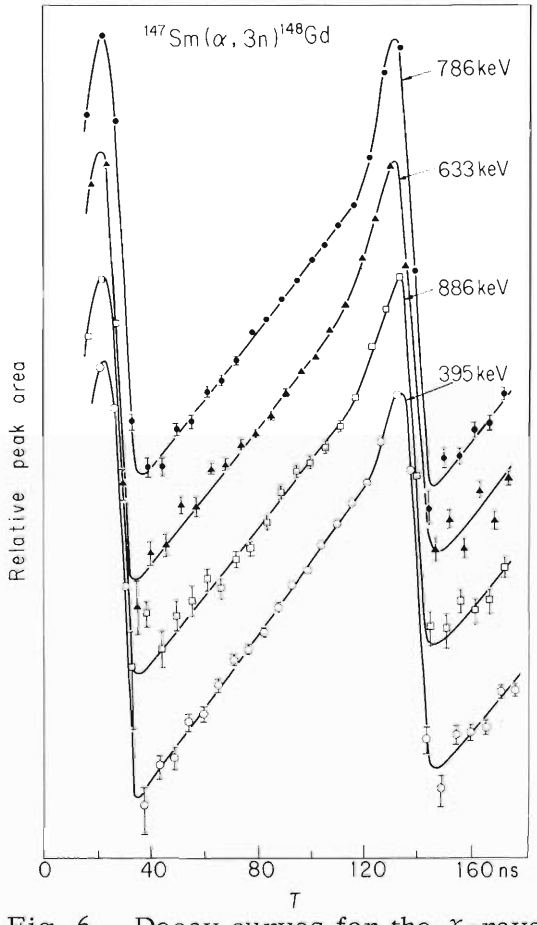

Fig. 6. Decay curves for the γ-rays from ^{147}Sm (α, 3n) reaction.

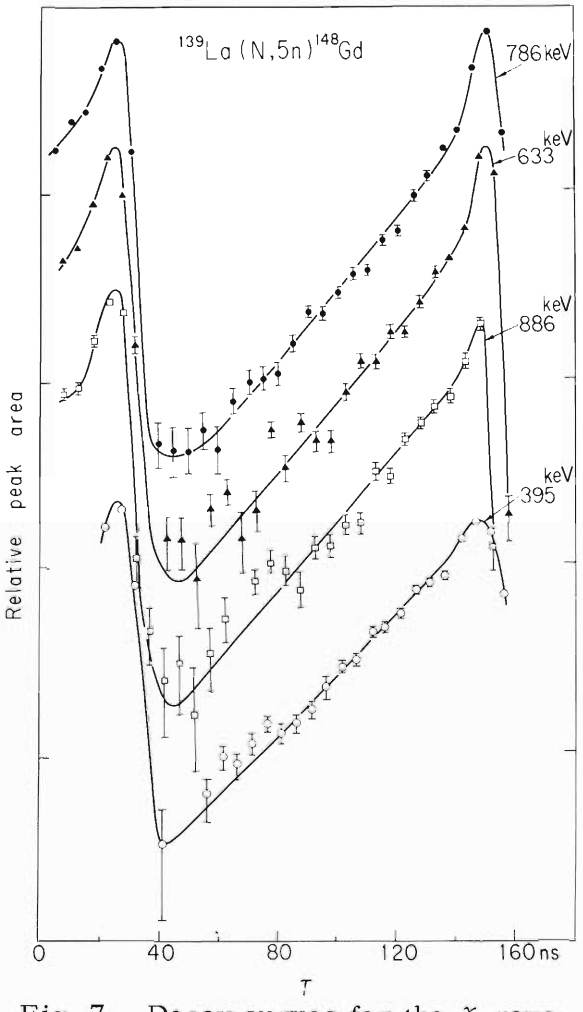

Fig. 7. Decay curves for the γ-rays from ^{139}La (N, 5n) reaction.

γ-rays corresponding to the same energies are greater for ^{147}Sm (α, 3n) reaction than those from ^{139}La (N, 5n) reaction. This fact indicates that the isomeric state has high angular momentum, because, in the de-exciting process from the compound nucleus with higher angular momentum made by heavy ions, the high spin states have a chance to be excited more often than the lower spin states if their energies are comparable.

Very little is known about the excited states in ^{148}Gd. Toth and Rasmussen[2] has only observed 0.780 and 1.12 MeV γ-rays by a scintillation spectrometer in the decay of ^{148}Tb. Though the ratios of the intensities of prompt to delayed γ-rays, the intensities of each single γ-rays and their anisotropies have been observed, we are not yet certain about the order of de-exciting γ-rays from the isomeric state except 633 ($4^+ \rightarrow 2^+$) and 786 keV ($2^+ \rightarrow 0^+$) transitions, because some inconsistency exists on the relative intensities of delayed γ-rays. The isomeric state lies at least above 1.814 MeV and the half-life is 16.7 ± 0.9 ns. The analysis is in progress.

Though there are some theoretical approaches on the level structure in this region[3),4)], no prediction has been obtained on the levels in ^{148}Gd. The extra protons outside the Z = 50 closed shell are distributed among the five available single-particle levels, i.e. $1g_{7/2}$, $2d_{5/2}$, $2d_{3/2}$, $3s_{1/2}$, and $1h_{11/2}$. Among them, $1h_{11/2}$ could contribute to the isomer. For the orbits of two extra neutrons outside the Z = 82 closed shell, $2f_{7/2}$, $1h_{9/2}$, and $1i_{11/2}$ are important for high spin states.

References

1) T. Inamura, S. Nagamiya, A. Hashizume, Y. Tendow, and T. Katou : IPCR Cyclotron Progr. Rep., 4, 67 (1970).
2) K.S. Toth and J.O. Rasmussen : J. Inorg. Nucl. Chem., 12, 236 (1960).
3) M. Rho : Nucl. Phys., 65, 497 (1965).
4) P. Haapakoski, T. Honkaranta, and P.O. Lipas : Phys. Letters, 31B, 493 (1970).

6. NUCLEAR INSTRUMENTATION

6-1. Development of a Wire Spark Chamber with Ferrite Cores for a Broad Range Magnetic Spectrometer

J. Fujita and S. Takeda

(1) Introduction

Several methods[1] have been developed in order to detect positions of charged particles in a broad range magnetic spectrometer. In a previous paper[2] we reported a method performed by many solid state detectors aligned on the magnetic focal plane. This multi-detector system will be used in heavy ion experiments. For experiments of lighter particles such as proton, deuteron and α-particle, another method was considered.

A model of a wire spark chamber with ferrite memory cores has been built and is going to be tested. Waters[3] reported that conventional ferrite memory cores could be used with a wire spark chamber for recording spark locations. Galster[4] obtained spatial resolution of approximately ± 0.3 mm in a wire spacing of 1 mm.

(2) Principle

Two wire planes are faced each other but the directions of wires on the two planes are orthogonal, that is, vertical and horizontal. Vertical wires pierce through the memory cores and fall down to the ground. A negative high voltage pulse is supplied to the horizontal plane. Then, if a charged particle passes through the spacing between the wire planes and ionizes gas atoms along its passage, there occurs a spark and the spark current magnetizes a memory core to one stable state. Then a current opposite to the spark current is made to flow. The memory core undergoes transition to the other stable state and at the same instant, information of spark location is perceived by a sense lead.

(3) Structure

Outline of the chamber is shown in Fig. 1.

A stainless steel wire with a diameter of 0.1 mm is used. Twenty horizontal and 50 vertical wires are aligned and the interval between wire planes is 2 mm. This space is made by inserting an epoxy frame 2 mm thick between wires. The wire spacing is 1 mm. So the operating area of the chamber is 20×50 mm^2. One end of the horizontal wires is pasted with electrically conductive glue and connected to a clearing voltage source via a RC high pass filter. The other end and Al plate of 30×30 mm^2 in area are separated by a Mylar film 9 μm thick and form a coupling condenser of about 30 pF. A high voltage pulse is supplied on this Al plate.

Ferrite cores used here are R456 manufactured by TDK Electronics Co. The dimensions of core are 0.76 mm in inner diameter, 1.27 mm in outer diameter and 0.39 mm in height. Transition current of the core is more than 400 mA and then a counter electromotive force of 80 mV occurs in a sense lead.

The epoxy frame with wires and cores is set into an acryl chamber with an inner volume of $150 \times 95 \times 25$ mm^3. Windows of 20×50 mm^2 are opened on the front and

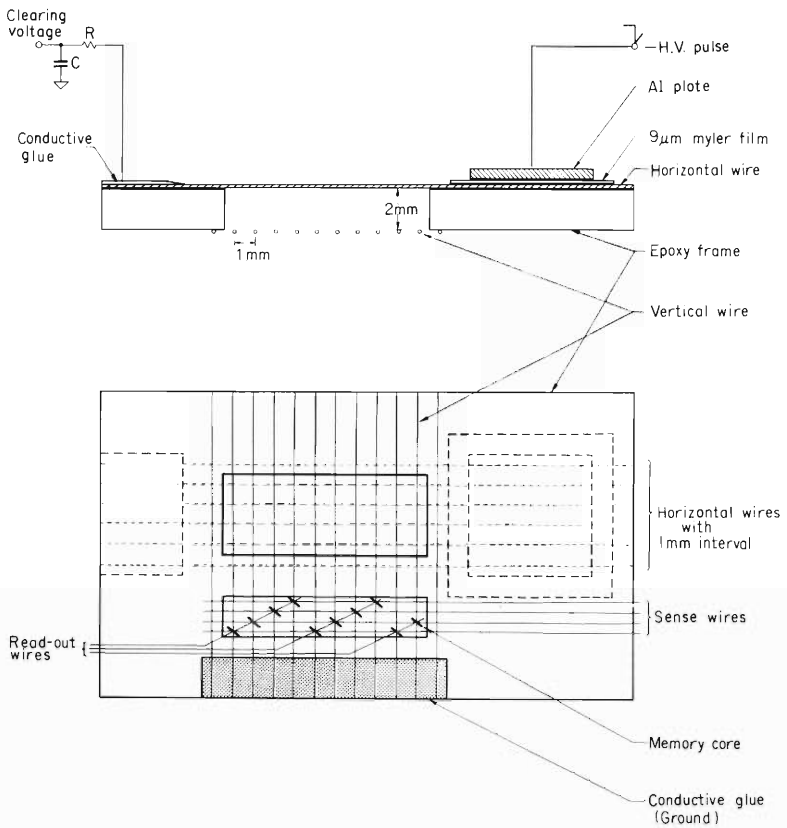

Fig. 1. Outline of wire spark chamber with memory cores.

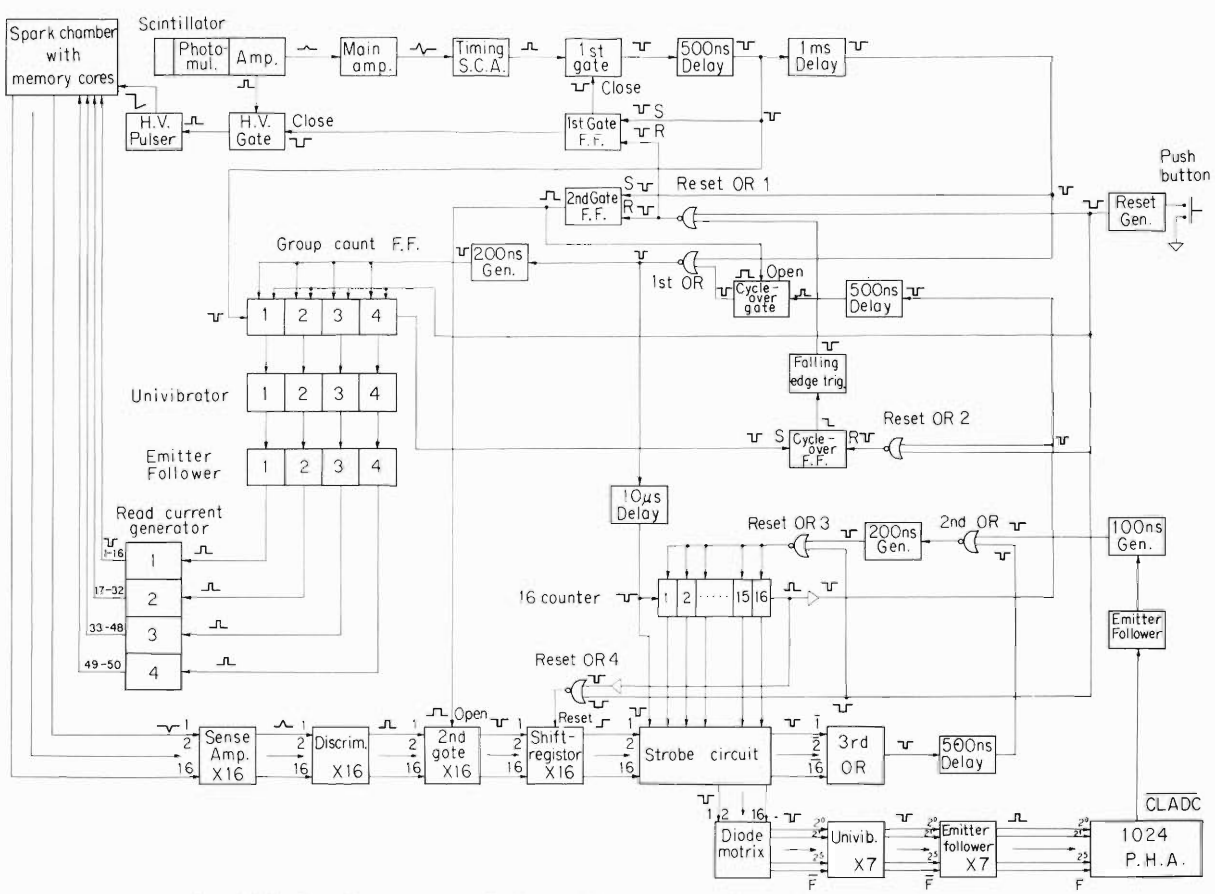

Fig. 2. Block diagram of electric system in wire spark chamber.

rear walls. Thin duralmin foil makes the interior of the chamber gas-tight. Two small holes are prepared for gas flow. Terminals for a high voltage pulse, a clearing voltage, 4 read-out and 16 sense wires are also provided on the rear wall. The outer size of the chamber is $180 \times 125 \times 55$ mm^3.

(4) Electronics

A block diagram of the whole electric system is shown in Fig. 2. A charged particle passing through the chamber produces an electric pulse in a photomultiplier with a plastic scintillator. The pulse triggers a high voltage pulser. Spark occurs at a position of particle track on the wire planes and a core threaded by a sparking wire stores information of the position. While the pulse fed through the 1st gate is delayed for 500 nsec and sets the 1st gate and the 1st group count flip-flop. The 1st gate F.F. closes the 1st and H.V. gates. In addition, the pulse delayed for 1 msec sets the 2nd gate F.F. which opens the 2nd gate, and is sent to group count F.F. and strobe circuit. Group count F.F. is composed of 4 digital counters and every pulse advances by one digit. At the same time with its count, each F.F. gives a selected pulse to read current generators. The cores consist of four groups with 16 cores threaded by read-out wires. There are 16 sense lines perpendicular to the vertical wires of chamber and if information exists in memory cores, it is transferred to 16 parallel shiftregisters by way of each sense amplifier, discriminator and opens the 2nd gate. Strobe circuit searches out the contents of the shiftregisters. If the register stores one bit, its address digit is transformed to a corresponding parallel binary code by diode matrix and sent to 1024 channel pulse height analyzer. A $\overline{\text{CLADC}}$ signal which indicates completion of memory function in the analyzer appears after several microseconds. $\overline{\text{CLADC}}$ passing through the 2nd OR advances the 16 counter by one count and also the contents of the next

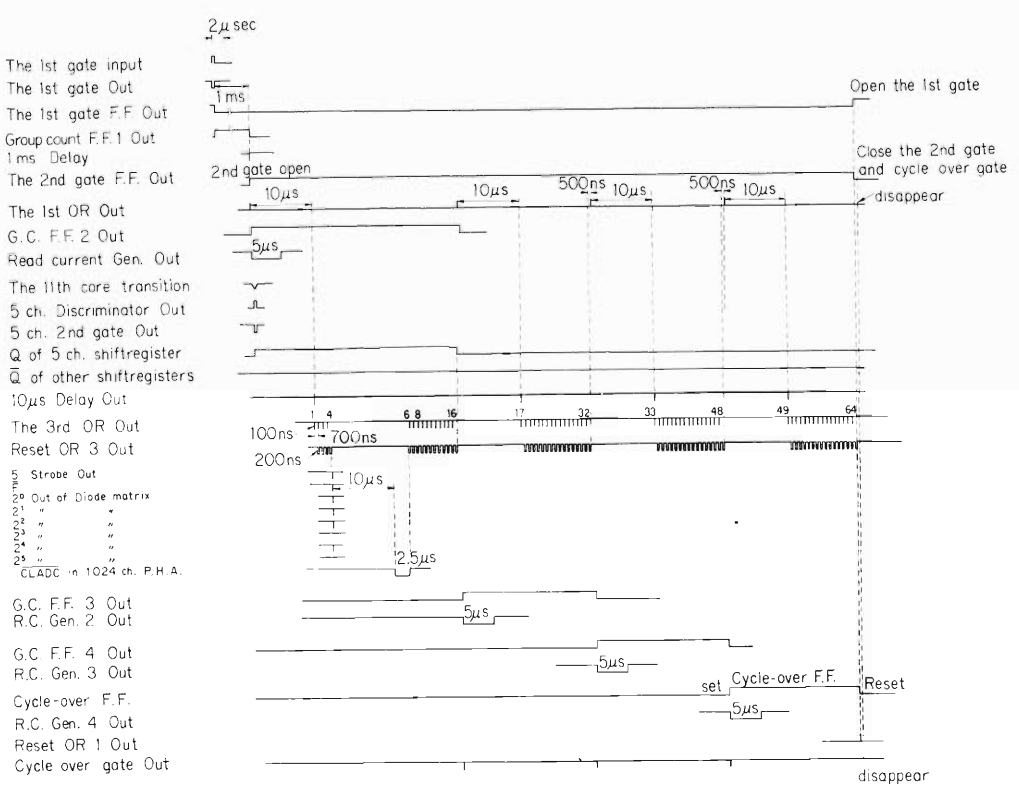

Fig. 3. Timing flow chart of pulses occurring in the electric system of a wire spark chamber.

register are strobed out. If there is no content, the 16 counter merely advances by one count via the 3rd OR, 500 nsec delay generator and the 2nd OR. When the strobe of the 16 registers finishes, the shiftregister is reset and at the same time next group of the cores is read out. The same work is repeated four times. At the instant when the last core group is read out, the cycle-over F.F. rises to high level. And it falls down to low level at the end of strobe function. The falling edge of cycle-over F.F. generates a reset pulse. This pulse resets the 1st and 2nd F.F. So the 1st and H.V. gates are opened, and the 2nd and cycle-over gates are closed. The cycle-over gate prevents the strobe system from free running. Thus the total cycle is over. The high voltage pulser has already recovered during this cycle. A timing flow chart is shown in Fig. 3. Almost all of the parts of this electric system are constructed by integrated circuits.

(5) Test results

Test results of the electric logic system using a pulse generator show a good performance. A high voltage pulse of 7 kV brings about visible sparks at several points in the gap. At present two difficult problems still remain. The first is that the logic system suffers disturbance from occurrence of spark. The second is the noise picked up by sense leads from the read current pulse.

References

1) G.L. Miller et al. : Nucl. Instr. Methods, 91, 389 (1971).
2) J. Fujita and S. Takeda : IPCR Cyclotron Progr. Rep., 4, 109 (1970).
3) J.R. Waters : Nucl. Instr. Methods, 21, 126 (1963).
4) S. Galster et al. : ibid., 46, 208 (1967).

6-2. A Mechanical Beam Chopper for Millisecond Beam Pulsing

A. Hashizume and H. Kumagai

In the determination of life of isomers or of very short-lived radioactive nuclei by a pulsed beam technique, the life to be measured is limited by the interval of the pulses. In the Cyclotron, the frequency of an oscillator varies between 6 Hz and 13.5 Hz depending on the kind of accelerating particles and their energy. This means if we utilize only the natural beam bunch, the range of half-lives to be measured is restricted from several nanoseconds to a few hundred nanoseconds. The shorter one is limited by the time jitter of pulsed beam originated in the acceleration mechanism and by the characteristics of fast responses of electronic circuits employed. A typical time resolution (FWHM) of fast component of γ-rays detected by a Ge (Li) detector and analyzed by a time-to-amplitude converter is about 10 ns.

To obtain a longer interval of pulsed beam, there are generally three methods: The modulation of an ion source, the deflection of a beam by a deflector and the mechanical chopper. A beam deflector operated by pulsed voltage is now under construction for measurement in the microsecond region. A mechanical chopper in this report is planned for the measurement of half-lives in the millisecond region. When compared to a neutron chopper a metal plate of proper thickness is sufficient to stop the accelerated particles, but there is a difficulty to generate a torque in vacuum. However, because of a recent development of precision D.C. motor which can be operated in vacuum, its realization becomes very easy.

A mechanical part is shown in Fig. 1. It consists essentially of an aluminum

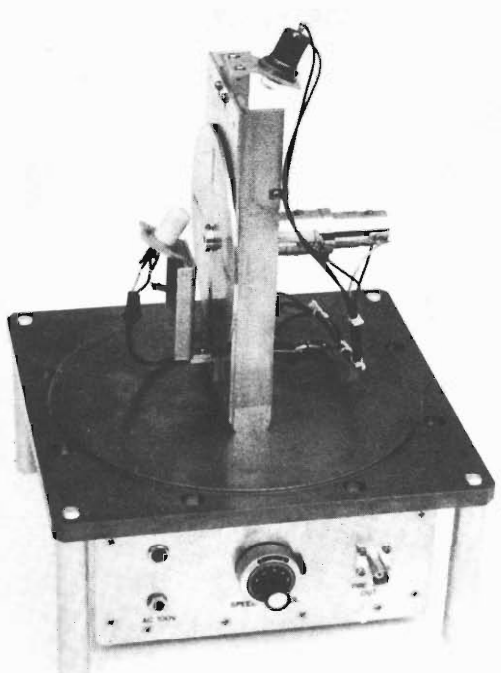

Fig. 1. Mechanical chopper.

disk of 115 mm in diameter and of 2 mm in thickness. The ratio of angles from the center of a disk to the window and the blind portion has been chosen to be one-eighteenth. There are two, four, or eight windows in a disk. The disk is attached to the axis of a precision D.C. motor designed specially for operation in vacuum. The speed of the motor can be controlled from 250 to 5700 r.p.m.; that is, we can obtain the interval of pulsed beam from 240 ms with one window to 1.3 ms with eight windows.

A lamp and a photo-transistor system send a triggering pulse in each time of beam passage to initiate a sawtoothed-wave generator. The output of the generator is D.C. coupled to the input of one of the axes of two-dimensional analyzer. Another axis is an energy spectrum of γ-rays detected with a Ge(Li) detector. A block diagram is shown in Fig. 2. A time calibration is given by a multivibrator of which the frequency is synchronized to a multiple of the triggering pulse frequency.

The chopper is placed just behind a slit of a beam course in the cyclotron facility, and is used to search for isomers decaying with half-lives in the millisecond region. Fig. 3 shows a typical spectrum of delayed γ-rays from excited states 2.954 MeV (7 or 8^-) in ^{132}Xe excited by ^{130}Te (α, n) reaction.

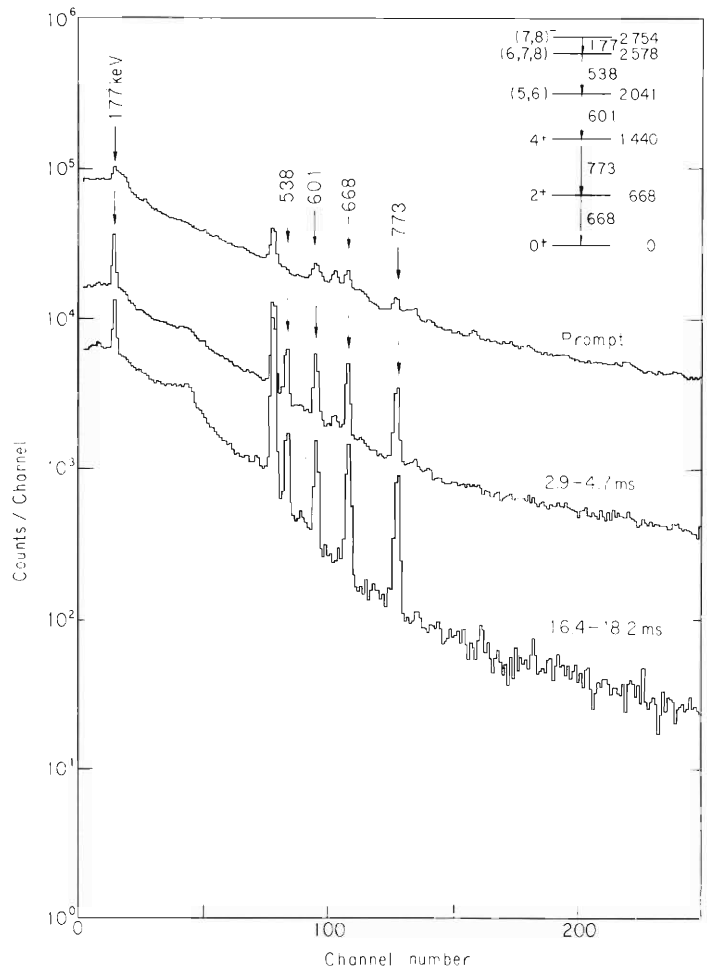

Fig. 2. Gamma-ray spectra from the ^{130}Te (α, 2n) ^{132}Xe reaction. Prompt and delayed (from 2.9 to 4.7 ms and from 16.4 to 18.2 ms) spectra are shown. The level scheme shown is that proposed by Brinckmann et al.[1)]

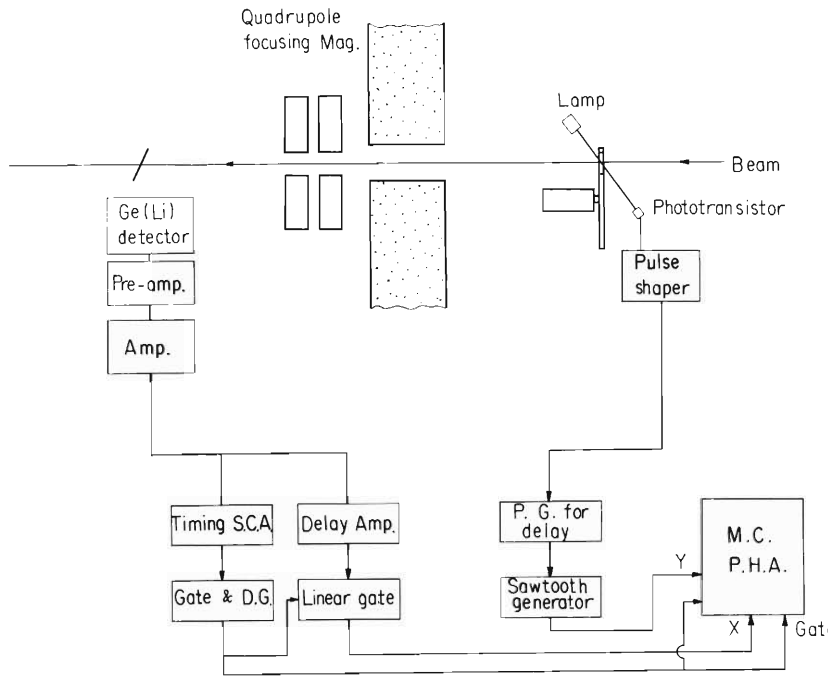

Fig. 3. A schematic diagram of the beam chopping system. The beam which passes through the chopper is guided to the target room. The size of the beam on the target is controlled by a quadrupole focusing magnet. The pulse from a photo-transistor is shaped and fed to the gate of a pulse generator to obtain a delayed pulse in the millisecond region.

Reference

1) H.F. Brinckmann, C. Heiser, and W.D. Fromm : Nucl. Phys., 96, 318 (1966).

6-3. A γ-Ray Spectrometer for Nuclear Study

M. Okano, Y. Tendow, T. Katou,
K. Izumo, and T. Hamada

A standard γ-ray spectrometer using semiconductor detectors has been employed for the measurements of radiations accompanying nuclear reactions as well as those from radioactive nuclides produced by the cyclotron.

Two commercially available solid-state detectors were used, one is a planar-type Si(Li) detector for X-ray measurements (Princeton Gamma-Tech) having 10 mm diameter and about 3 mm depletion depth. The other is a coaxial-type Ge(Li) detector (ORTEC) with an active volume of 23.1 cm^3. The guaranteed system resolutions of these detectors were 300 eV for 5.9 keV Fe K X-rays and 3 keV for 1332 keV ^{60}Co γ-rays, respectively. These detectors were operated in conjunction with the ND 2200 system multi-parameter pulse height analyser. The system resolution and the relative full energy peak efficiency were measured using several standard radioactive sources, and the results are shown in Fig. 1. Recently, the preamplifier for the Ge(Li) detector, ORTEC 118A type, has been replaced by ORTEC 120F type to improve the resolution.

The Si(Li) detector was mainly used for the detection of atomic excitation X-rays and of γ-rays of energy lower than 100 keV. The Ge(Li) detector was equipped in a 10 cm thick lead cave together with an annular type 6 in $\times$ 6 in NaI(Tl) scintillator

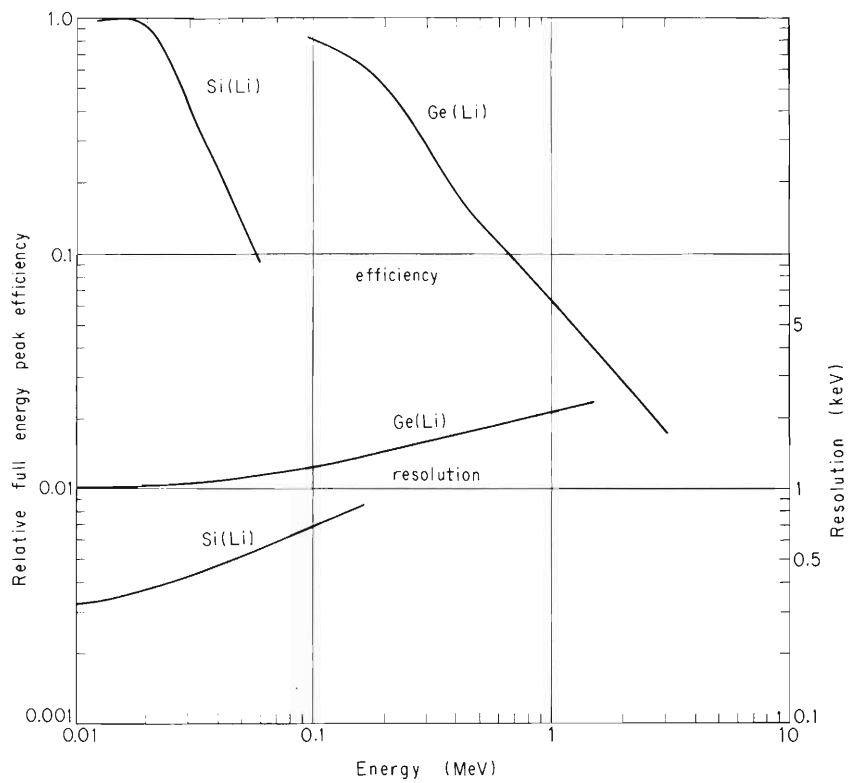

Fig. 1. Relative full-energy peak efficiency and energy resolution of the Si (Li) and Ge (Li) detectors as a function of photon energy.

Table 1. Background counting rate of the Ge(Li) detector placed in a 10 cm thick lead shield at energy intervals of full energy peaks of γ-rays from various nuclides.

Nuclides	Energy (keV)	Background counting rate without anti-Compton gate (cpm) (during 40 h)	Background counting rate with anti-Compton gate (cpm) (during 65 h)
annihilation photon	511	0.148 ± 0.011	0.027 ± 0.004
Tl-208	583	0.026 ± 0.007	0.026 ± 0.007
Bi-214	609	0.016 ± 0.006	0.030 ± 0.004
Cs-137	662	0.010 ± 0.006	0.011 ± 0.003
Ac-228	908	0.013 ± 0.005	0.011 ± 0.003
(Zn-65) (Bi-214)	(1115 1120)	0.021 ± 0.006	0.010 ± 0.002
K-40	1462	0.025 ± 0.005	0.044 ± 0.004
Bi-214	1764	0.007 ± 0.003	0.005 ± 0.002
Tl-208	2614	0.007 ± 0.003	0.007 ± 0.002

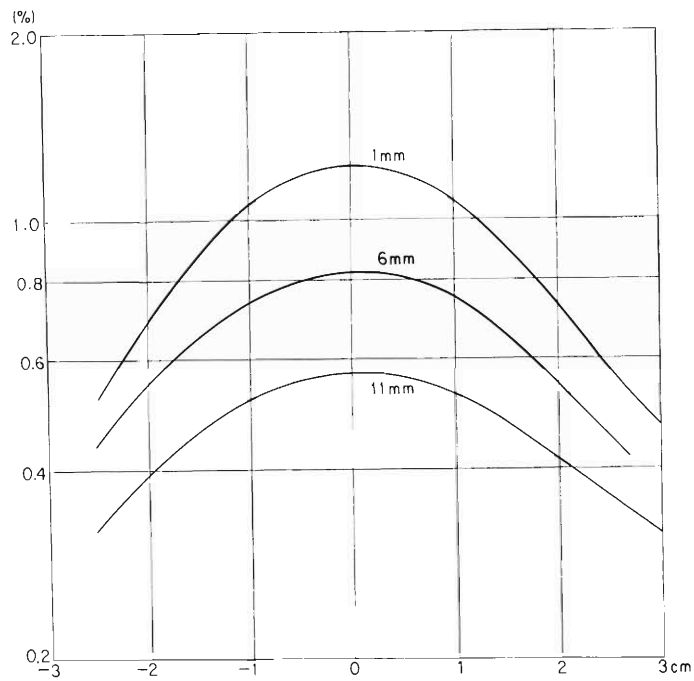

Fig. 2. Absolute full energy peak efficiency of the Ge (Li) detector for Cs-137 662 keV gamma-rays. Abscissa: radial distance of the source from the detector axis. Parameter: vertical distance from the detector end cap.

split by halves, and the system is used as an anti-Compton or pair-spectrometer.[1] The Compton spectrometer reduces not only the Compton background but also the cosmic-ray background. The very low inherent background of the system was achieved by selecting the construction material of low radioactivity. Background counting rates with and without anti-Compton gate are shown in Table 1. The absolute full energy peak efficiency at 662 keV ^{137}Cs line as a function of radial distance of the source from the axis of the detector near the detector end cap, and that as a function of vertical distance along the axis from the end cap are shown in Fig. 2 and in Table 2, respectively.

This spectrometer system enables us to make energy and intensity measurements of X-rays and γ-rays over an energy range from 2 keV to several MeV and also to detect gamma-emitting nuclides of extremely low activity down to the order of pCi.

Table 2. Absolute full energy peak efficiency of the Ge(Li) detector for Cs-137 662 keV γ-ray as a function of distance from source to top of end cap.

Distance (mm)	Efficiency (%)
1	1.21
2	1.08
5	0.87
10	0.61
20	0.344
50	0.123
100	0.044
200	0.0133
500	0.00205

6-4. Data Processor

T. Wada, Y. Chiba, and F. Yoshida

(1) On-line PHA System

The interface [1] of two ADC units to the DDP-124 computer was improved to reduce the dead time. An one-word (24 bits) buffer-register was introduced and the contents of it could be read into the accumulator directly. The 12-bit data lines from one ADC was connected to the lower 12 bits of the buffer-register, and the other 12-bit data lines to the upper 12 bits. Figure 1 shows the block diagram of this new system. For simplicity, only the connection for AND mode (Interrupt will occur when two buffer-full flip-flops are set) is shown. In the real system there is a switch to change the mode. There are four modes, each ADC single, OR and AND modes. For OR mode, one more gated flip-flop is needed to gate/hold the buffer-full signal (B in the figure). This is not shown in the figure. The dead time of this system is (ADC dead time + 1.5μsec), when the average interval between input signals is longer than the processing time of computer program.

The computer program to write the address data from ADC on a magnetic tape was made. This is useful for the identification of isotopes in the experiment of heavy ion reaction.

(2) Software

Many programs for the DDP-124 computer has been produced for four years.

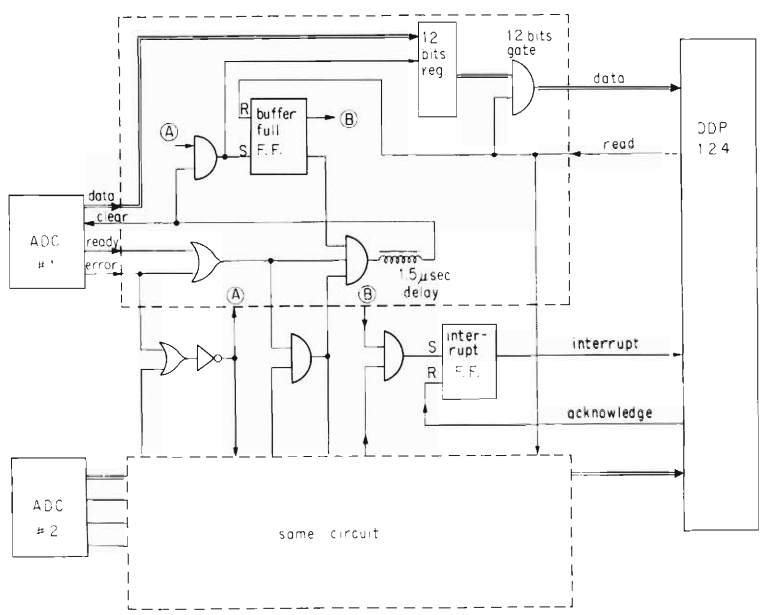

Fig. 1. The block diagram of the new interface for two ADCs to DDP-124 computer.

Their contents are variable. About 10 programs are produced for plotting, printing and simple calculation of data of PHA system and so on. There are four programs which calculate orbits of cyclotron or magnets. Using other programs, we can calculate kinematics, Q value, charge exchange, etc. There are also some programs for listing, conversion and instruments test.

Reference

1) T. Wada, Y. Chiba, K. Matsuda, and M. Yoshimizu : IPCR Cyclotron Progr. Rep., 1, 62 (1967).

7. RADIOCHEMISTRY

7-1. Chemical Behavior of Carbon in Semiconductor Silicon in the Dissolution and Fusion of the Matrix

T. Nozaki, Y. Yatsurugi, and N. Akiyama

Our study of carbon in semiconductor silicon has been continued for 4 years and some results were reported already.[1)~6)] Thus, the following is now known : (1) the solubility of carbon in solid silicon is about 2.5 wt ppm at the melting point, and carbon with a concentration higher than this value forms SiC precipitate ; (2) most kinds of commercial semiconductor silicon contain from 50 ppb to 2 ppm of carbon ; and (3) carbon dissolved in silicon occupies the substitutional site in the silicon crystal lattice. In the present report, the chemical behavior of carbon in semiconductor silicon in the dissolution and fusion of the matrix is described.

The ^{11}C-tracer technique was used, with the nuclear reaction for the production of ^{11}C being $^{11}B(p,n)^{11}C$. Three kinds of ^{11}C-containing silicon samples were prepared by the following methods. (1) A silicon wafer (3 cm diameter, 2 mm thickness) containing boron from 50 to 100 ppm was bombarded (13 MeV proton, a few μA, 20 min), and then left for 40 min to allow the ^{30}P formed by the $^{30}Si(p,n)^{30}P$ reaction to decay out. (2) A B_2O_3 target was bombarded (13 MeV proton, about 10 μA, several min) in a helium stream from a cylinder to a chemistry room. A noticeable portion of the ^{11}C formed was evolved into the stream as oxides and carried to the chemistry room, where it was caught in a liquid-nitrogen trap. A part of a small silicon rod sustained in an evacuated Pyrex tube was fused by radio-frequency heating, and the ^{11}C was introduced into the tube. After being kept molten for a few min, the silicon was left to cool, and then its surface was removed by etching. (3) The process was similar to that in (2), but the silicon melt was brought into contact with a small quantity of graphite powder or with gaseous carbon oxide. The ^{11}C atom in the sample prepared

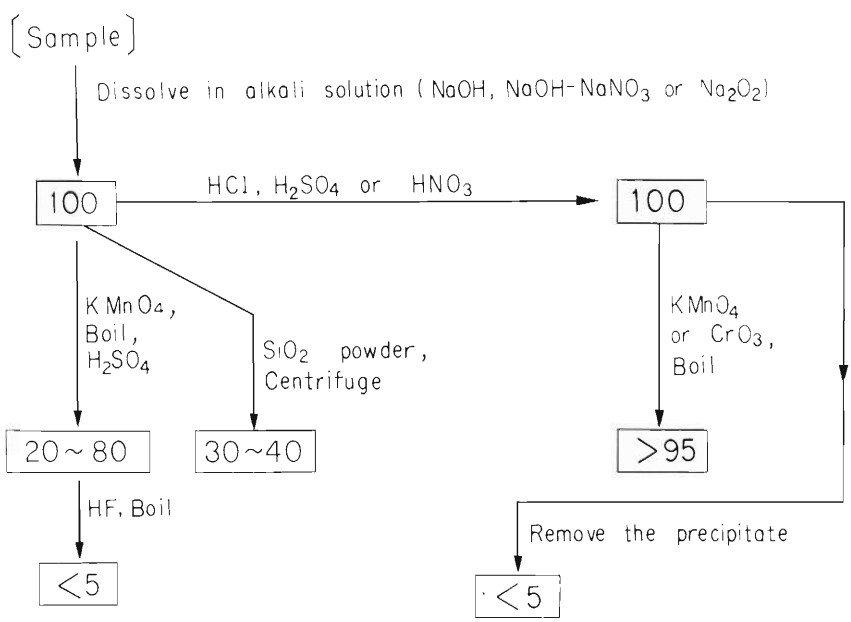

Fig. 1. Behavior of homogeneously dispersed ^{11}C —— fraction of ^{11}C remaining(%).

by Method 1 can occupy a higher-energy site in the silicon crystal, because it was provided with the nuclear recoil energy at its nascent stage. The samples given by Methods 1 and 2 contain carbon homogeneously dispersed atomistically, but the SiC precipitate is present in the sample obtained by Method 3.

After the measurement of radioactivity, the sample was decomposed by the following treatments : (1) dissolution in an alkaline solution, (2) dissolution in a HF-HNO_3 solution, (3) alkali fusion with NaOH, and (4) acidic fusion with Pb_3O_4-B_2O_3. Then, the product was treated with various reagents, and the behavior of the ^{11}C was examined. The quantity of the reagent used was at least 50 % excess in all cases.

The results are shown in Figs. 1, 2, and 3. No difference was observed in the behavior of ^{11}C between the sample prepared by Method 1 and that prepared by Method 2. From Figs. 1 and 2, the carbon homogeneously dispersed is found to behave quite similarly to elementary carbon in minute grains. In the acidification of the alkaline

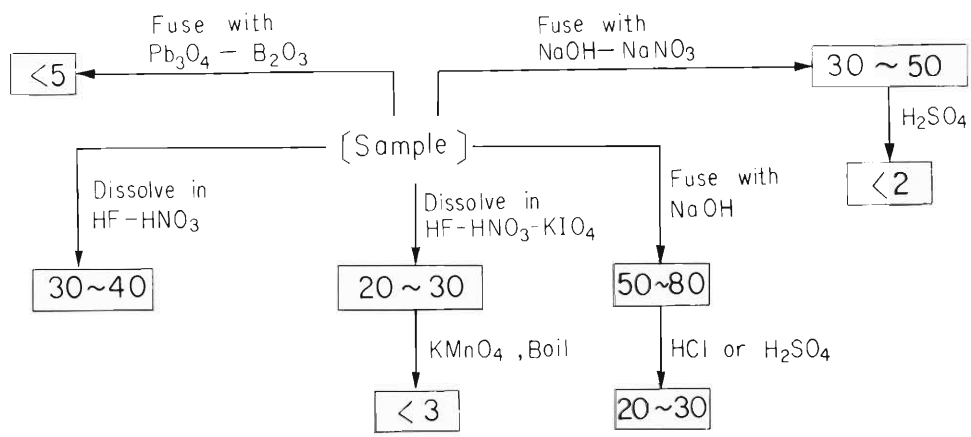

Fig. 2. Behavior of homogeneously dispersed ^{11}C— fraction of ^{11}C remaining (%).

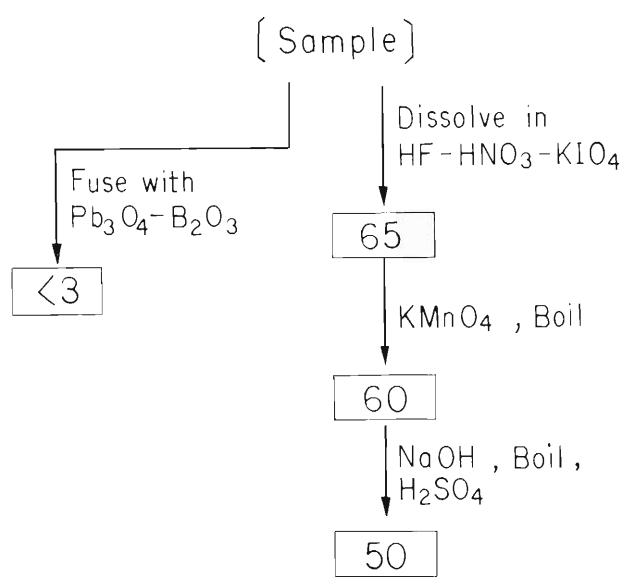

Fig. 3. Behaviour of coagulated ^{11}C — fraction of ^{11}C remaining (%).

solution, it is quite probable that hydrated silicon oxide is precipitated embracing almost the entire part of the carbon.

Table 1 indicates the sensibility of the three analytical methods to the homogeneously dispersed carbon and to the SiC precipitate. The fraction of carbon in SiC determined as carbon in the second method in Table 1 is dependent on the degree of coagulation of the SiC precipitate. Therefore, by the use of the three methods in Table 1, it is possible, though high accuracies are needed in the determination, to get information about the dispersion state of carbon in silicon.

Table 1. Sensibility of the three methods to the different physical states of Carbon in silicon.

Method		Homogeneously dispersed carbon	Coagulated carbon
Infrared spectrophotometry		+	−
Activation analysis	$HF-HNO_3-KIO_4-KMnO_4$ dissolution	+	±
	$Pb_3O_4-B_2O_3$ fusion (or nondestructive)	+	+

References

1) T. Nozaki, Y. Yatsurugi, and N. Akiyama : J. Radioanal. Chem., 4, 87 (1970).
2) T. Nozaki, Y. Yatsurugi, and N. Akiyama : J. Electrochem. Soc., 117, 1566 (1970).
3) T. Nozaki, Y. Makide, Y. Yatsurugi, N. Akiyama, and Y. Endo : Int. J. Appl. Radiat. Isotopes, 22, 607 (1971).
4) T. Nozaki : IPCR Cyclotron Progr. Rep., 1, 66 (1967).
5) T. Nozaki, Y. Yatsurugi, and N. Akiyama : ibid., 2, 121 (1968).
6) T. Nozaki, Y. Yatsurugi, and N. Akiyama : ibid., 3, 88 (1969).

7-2. Excitation Function for Some Triton-induced Reactions

T. Nozaki, M. Okano,
M. Furukawa, S. Kume, and R. Seki

The excitation functions for the reactions of $^{27}Al(t,2p)^{28}Mg$, $^{26}Mg(t,p)^{28}Mg$, Si + t → ^{28}Mg, Al + t → ^{24}Na, Si + t → ^{24}Na, and $^{16}O(t,n)$ ^{18}F were measured up to the triton energy of 23 MeV. The stack foil method was used, the target stack for aluminum, magnesium, silicon, and oxygen being of aluminum foil (about 25 mg/cm^2), magnesium foil (15 to 20 mg/cm^2) or vacuum-sublimated magnesium (about 1 mg/cm^2) on tantalum foil, silicon wafers (about 60 mg/cm^2), and quartz plates, respectively. The induced radioactivity was measured by a Ge(Li) detector and a NaI detector of calibrated efficiencies.

The results are shown in Figs. 1, 2, and 3. Their cross sections are for the target substances of the natural isotopic composition. The uncertainty in the absolute cross section can be regarded as 15 % for all the reactions except for the reaction of

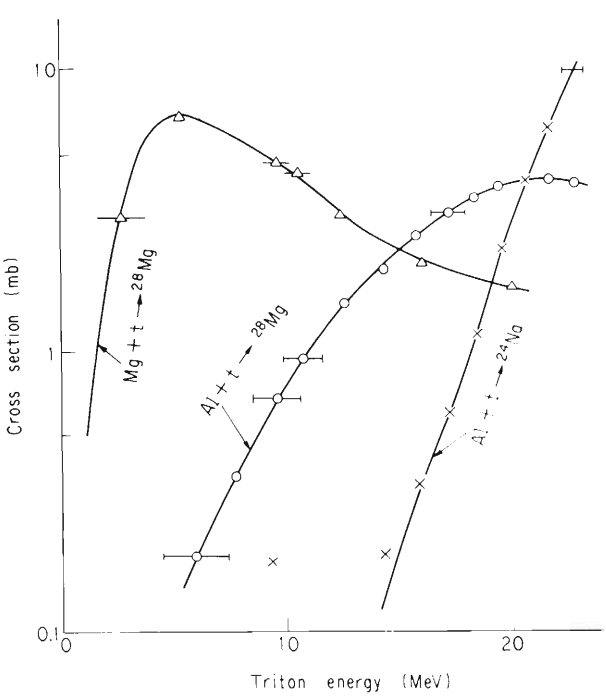

Fig. 1. Excitation functions for the reactions of Al+t → ^{28}Mg, Al+t → ^{24}Na, and Mg+t → ^{28}Mg.

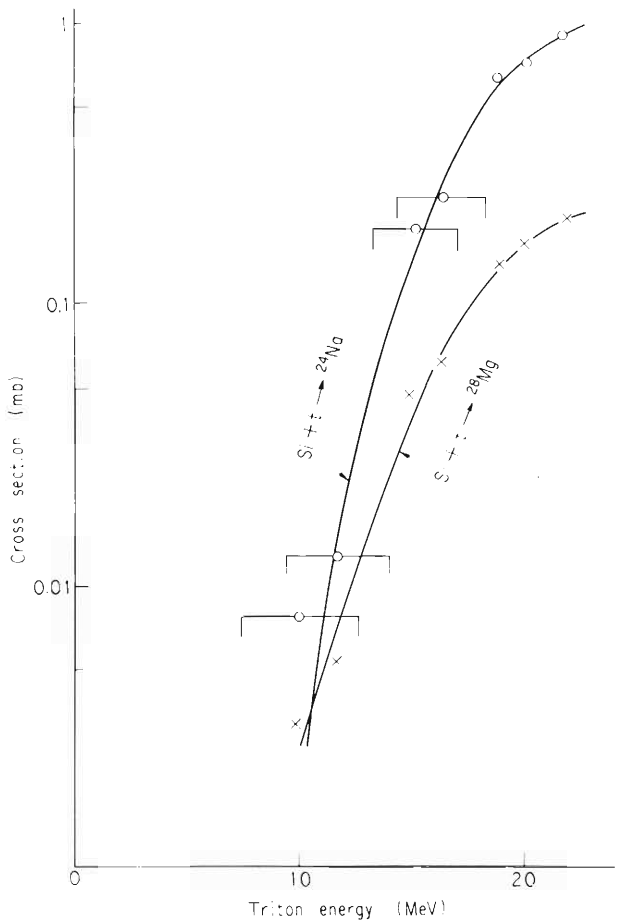

Fig. 2. Excitation functions for the reactions of Si+t → ^{28}Mg and Si+t → ^{24}Na.

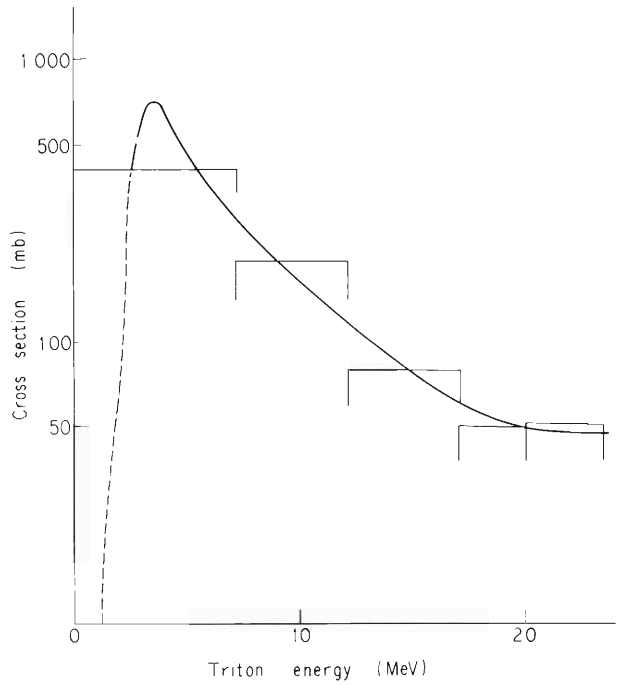

Fig. 3. Excitation function for the reaction of O+t $\rightarrow {}^{18}F$. (The dotted line region is given in Ref. 1))

$^{16}O(t,n)\,^{18}F$. The excitation function for this reaction has a fairly sharp peak in the low-energy region ; thus, the precise measurement of the maximum cross section and the peak shape requires a more elaborate work with thinner target plates.

Reference

1) P. E. Wilkniss and H. J. Born : Int. J. Appl. Radiat. Isotopes, 18, 59 (1967).

7-3. A Mössbauer Spectroscopic Study of Chemical States of ^{119}Sn after EC Decay of ^{119}Sb in Antimony Chalcogenides

F. Ambe, H. Shoji*, S. Ambe, M. Takada**, and N. Saito

Measurement of the Mössbauer emission spectra gives valuable information concerning the after-effect of nuclear decay as well as concerning the chemical behaviour of atoms in a dilute solid solution. We have been studying application of ^{119}Sn-Mössbauer emission spectroscopy, using cyclotron-produced ^{119}Sb (38.0 h) and ^{119m}Te (4.7 days) as source nuclides. Here we will report the results recently obtained on antimony chalcogenides. A partial description of the experiments has already been made. [1)]

The ^{119}Sb and ^{119m}Te were produced by the p-, d-, or α- irradiation of a tin plate with a natural isotopic abundance. The source nuclides were separated from the tin target by radiochemical procedures consisting of solvent extraction, ion exchange, and precipitation. Antimony chalcogenides labelled with the nuclides were prepared by well-established methods reported in the literature. The ^{119}Sn-Mössbauer emission spectra were measured with the labelled compounds as the source at liquid nitrogen temperature against a barium stannate standard absorber. In Table 1 are summarized the Mössbauer parameters derived from the observed emission spectra by least-squares computer fitting. The values of the isomer shift versus barium stannate are shown in the Table, the sign being as in usual absorption spectra.

Table 1. ^{119}Sn-Mössbauer parameters of the emission spectra in antimony chalcogenides.

Source compounds	Isomer shift (mm/sec)	Quadrupole splitting (mm/sec)	Assigned valence
$^{119}Sb_2O_3$	3.2	1.8	Sn(II)
$^{119}Sb_2S_3$	3.8	---	Sn(II)
	1.4	---	Sn(IV)
$^{119}Sb_2Se_3$	3.7	---	Sn(II)
	1.7	---	Sn(IV)
$^{119}Sb_2Te_3$	3.4	---	Sn(II)
$Sb_2{}^{119m}Te_3$	2.6	0.6	———

* Visitor from Tokyo University of Education.
** Visitor from the University of Tokyo.

Antimony trioxide in the cubic form was prepared by hydrolysis of a solution of trivalent antimony and sublimation of the product in a vacuum. Its emission spectra consisted of a doublet, which may be assigned to the divalent state of tin on the basis of the data of the absorption spectra of tin oxides.

For antimony trisulfide, measurements were made on samples in the crystalline black form prepared by three different methods. In the wet method, the sample in the crystalline form was prepared by heating the amorphous orange sulfide in dilute hydrochloric acid and then drying the product over phosphorus pentoxide in a vacuum. The emission spectrum of this sample is shown at the top of Fig. 1. In the Henz method, [2] shown in the middle of the figure, amorphous sulfide was heated in an argon atmosphere in order to obtain the crystalline form. In the last method, the crystalline sulfide prepared by the Henz method was sublimed in a vacuum. As can be seen in Fig. 1, the emission spectra of the sulfides consisted of two emission peaks, one corresponding to the divalent state of tin, and the other to the tetravalent state of tin, their isomer shifts being almost independent of the method of preparation. The most striking finding with regard to this compound is the change in the intensity ratio the two peaks as the method of preparation is changed. Further experiments are in progress to find out the factors influencing the intensity ratio.

Antimony selenide and telluride were prepared by fusing a stoichiometric mixtrue of antimony and selenium or tellurium in an argon atmosphere. Antimony selenide gave two emission peaks which can be assigned to the divalent and tetravalent states of tin, as in the case of sulfide. In this compound, however, the ratio of intensity of the two peaks was not reproducible, even for the samples prepared by the same method.

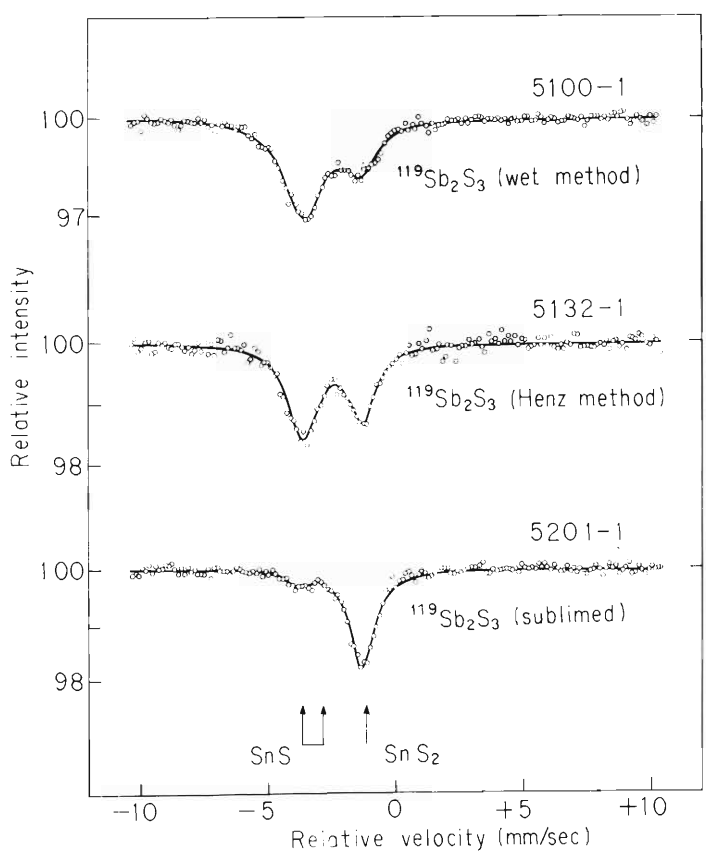

Fig. 1. ^{119}Sn-Mössbauer emission spectra in antimony trisulfides.

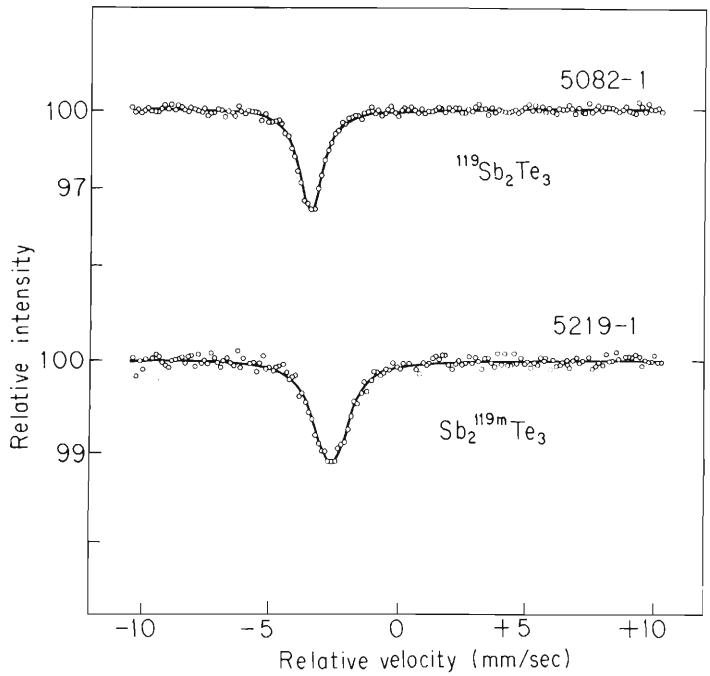

Fig. 2. ^{119}Sn-Mössbauer emission spectra in antimony tellurides.

For antimony telluride, a comparative study of novel type was made taking advantage of the fact that ^{119}Sb can be incorporated in the lattice of this compound in two different ways, directly as ^{119}Sb in the antimony site ($^{119}Sb_2Te_3$) or as the decay product of ^{119m}Te labelled in the tellurium site ($Sb_2{}^{119m}Te_3$). As can been seen in Fig. 2, a clear difference was observed between the emission spectra of the two types of labelled compounds, $^{119}Sb_2Te_3$ and $Sb_2{}^{119m}Te_3$. $^{119}Sb_2Te_3$ gave a single line peak with an isomer shift very close to that of tin telluride, while $Sb_2{}^{119m}Te_3$ gave a broad emission peak with an isomer shift of 2.6 mm/sec, showing that the s-electron density at the tin nucleus is smaller in this case than in $^{119}Sb_2Te_3$. In Table 1 is shown the value of quadrupole splitting computed on the assumption that the peak is an unresolved symmetric doublet due to a quadrupolar hyperfine interaction of the ^{119}Sn nucleus.

References

1) F. Ambe, H. Shoji, S. Ambe, M. Takeda, and N. Saito : IPCR Cyclotron Progr. Rep., 4, 115 (1970).
2) F. Henz : Z. Anorg. Chem., 37, 18 (1903).

7-4. Charge States of Ions Produced by the Decay of ^{18}F

S. Yokoi*, M. Aratani, and T. Nozaki

Measurements have been made on the charge distribution of the ions produced by the decay of ^{18}F (100 m) trapped on the metal plates. The apparatus employed was the same as previously reported.[1] It was a magnetic spectrometer with an ion detector of a pulse-counting mode.

The radionuclide, ^{18}F, was produced by the ^{16}O (^{3}He, p) ^{18}F nuclear reaction. An oxygen stream was bombarded in a vessel designed for cyclotron bombardment by ^{3}He particles (14 ~ 15 MeV).[2] Metal plates of 0.5 × 10 × 20 mm were dried after surface cleaning and placed for exposing to the bombarded gas stream at the outlet of the vessel. A part of the ^{18}F formed in the gas stream was trapped on the surfaces of the metal plates.

The measurement of the half-life of the radioactivity on the metal plates showed that it consisted only of ^{18}F. The counting rates of the metal plates were measured by means of a scintillation counter.

It was shown that the ^{18}F on the metal plates was easily removed by washing in a water flow. For example, the counting rates for Ag and Cu plates decreased to 5.3 % and 4.8 % respectively after washing. On the other hand, it was shown that the ^{18}F on the metal plates was not removed by vacuum exhaustion. From these results, it was deduced that a major part of the ^{18}F was attached by chemisorption on the surface of the metal plates.

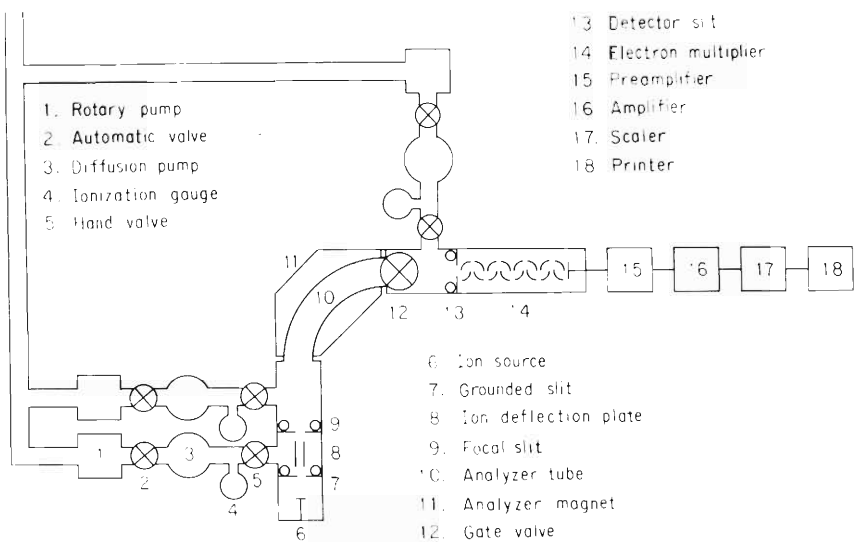

Fig. 1. Charge spectrometer for solid radioisotopes.

* Present address : Ota Pharmaceutical Co., Kawaguchi, Saitama Prefecture, Japan.

A metal plate with ^{18}F was employed as the ion source of the spectrometer. The ion-expelling voltage was 4500 ~ 5000 V. The metal exposed to the bombarded gas stream was immediately mounted in the ion-source chamber of the spectrometer, and the apparatus was exhausted to 2×10^{-6} Torr. When the ion-expelling voltage was applied, the ^{18}F on the metal plate behaved as a pulsed-ion emitter due to its decay. The ions produced by the decay of the ^{18}F on the metal surface were expelled through a grounded slit with stainless steel meshes, analyzed by the magnetic field, and counted by a 16-stage Cu-Be electron multiplier.

The charge distribution of the atoms produced by the decay of the ^{18}F on the Cu plate was as follows : Singly-charged ion, 9.5 ; +2-charged ion, 1.0 ; +3-charged ion, 1.4 ; +4-charged ion, 2.5 ; +5-charged ion, 2.8 ; +6-charged ion, 4.0. In this range the ion yields increased with a decrease in the number of 2s and 2p electrons of the $(1s)^2 (2s)^2 (2p)^4$ of ^{18}O with the exception of the singly-charged ion. The yields of both the +7- and +8-charged ions were less than that of the +6-charged ion in every run, although the values fluctuated. The positron decay of ^{18}F and the inner-shell ionization of the ^{18}O formed from ^{18}F may be responsible for this type of charge distribution.

References

1) M. Aratani and N. Saito : Mass Spectros., 18, 906 (1970).
2) T. Nozaki, Y. Tanaka, A. Shimamura, and T. Karasawa : Int. J. Appl. Radiat. Isotopes, 19, 27 (1968).

8. RADIATION CHEMISTRY AND RADIATION BIOLOGY

8-1. Radiolysis of Ketones in High LET Region

M. Matsui, M. Imamura, and T. Karasawa

In the systematic studies of the LET effects on the radiolysis of liquid organic compounds, some ketones were subjected to the study using heavy-ion beams.

Ketones used were acetone, methyl-ethyl ketone, and diethyl ketone. Heavy ions were ^{12}C of 53.5 MeV and ^{14}N of 22.4 ~ 68.0 MeV; instantaneous LET-values of these ions were 29 and 32~61 eV/Å, respectively. Experimental procedures have been described previously.[1),2)]

In this report, the results with diethyl ketone are described. The radiolytic gaseous products from diethyl ketone are H_2 and CO as principal products and saturated and unsaturated C_1-C_4 hydrocarbons as minor products. These products were determined gaschromatographically using silica gel-Al_2O_3 and Molecular Sieve 5A columns. Great care was taken for collecting the hydrocarbons produced from irradiated samples.

The yields (G) of H_2 and CO are plotted as a function of the energy-loss parameter of radiation defined by $z = (1/E_S)\int_0^{Es} (-dE/dx)\, dE$ in Fig. 1. (E_S is the energy of ions entering solution ; $-dE/dx$ is LET). The yields of hydrocarbons are summarized in Table 1. These data include the results for ^{60}Co-γ- and α-radiolyses. In the radiolyses with γ- and α-radiations, samples contained iodine of about 7×10^{-3}M, which serves as a radical scavenger. This means that the G-values for γ- and α-radiolyses represent the so-called molecular yields ; in the heavy-ion radiolysis, all the yields can be regarded as molecular ones.

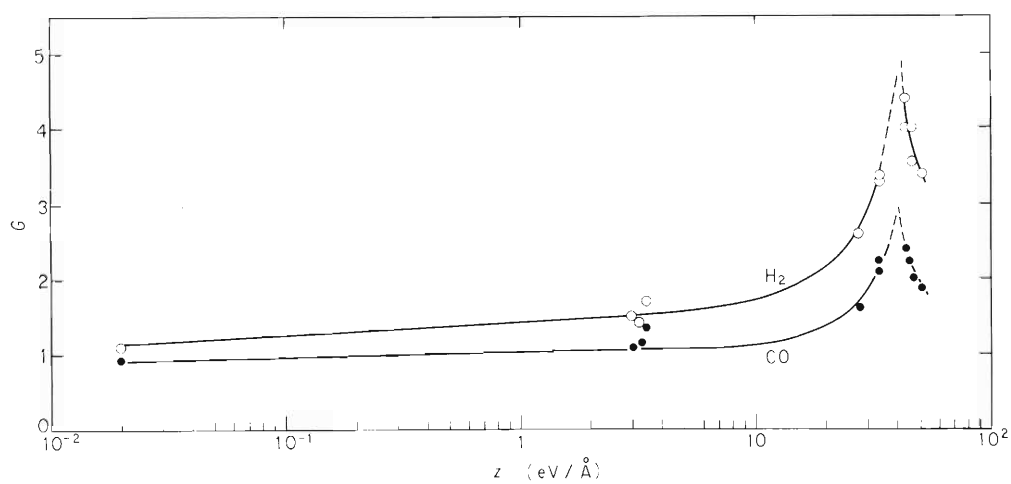

Fig. 1. Variations with LET (stopping-power parameter, z) of the yields of H_2 (○) and CO (●) in the radiolysis of liquid diethyl ketone. Maximum G (H_2) and G (CO) appear to be expected at z = 40 eV/Å.

Table 1. Radiolysis yields of hydrocarbons.

Radiation	$[I_2]$ M	LET (eV/Å)	G-Values					
			CH_4	C_2H_6	C_2H_4	C_2H_2	C_3H_8	n-C_4H_{10}
^{60}Co-γ	$\sim 7 \times 10^{-3}$	0.02	0.05	0.23	0.46	0.05	0.02	0.15
^{4}He	$\sim 7 \times 10^{-3}$	3~4	0.06	0.26	0.49	0.09	0.03	0.16
^{14}N	0	61.2	0.31	0.69	1.2	0.52	0.17	0.42

The important features of the experimental results are summarized as follows:

(1) As shown in Fig. 1, $G(H_2)$ and $G(CO)$ increase slowly from nearly 1 as LET increases in the region less than 10 eV/Å and then a steep increase takes place. The both yields seem to reach their maximum values in the vicinity of 40 eV/Å and then drop at higher LETs'. The yields of some hydrocarbons also appear to show similar behavior.

(2) The ratio of $G(H_2)$ to $G(CO)$ increases as LET increases : 1.1, 1.3, and 1.6~1.8 for γ-, α-, and heavy-ion radiolyses, respectively.

(3) The increase in $G(C_2H_2)$ with increase of LET is outstanding among increasing yields of hydrocarbons.

The slow increases of the molecular yields of H_2 and CO at LETs' less than 10 eV/Å may be explained on the basis of a simple diffusion-kinetics model. The steep increases in the higher LET region cannot be accounted for unless some contribution of the thermal spikes in the dense ionization tracks is assumed.

Although a definite evidence of the thermal-spike effects in the high-LET radiation tracks has not been demonstrated in liquid-phase radiolysis, the present results seem to offer a support for this hypothesis. The ratio, $G(H_2)/G(CO)$, increases with increasing LET from 1.1 for γ-rays to 1.6~1.8 for heavy ions. One molecule of CO should be produced from one molecule of ketone, and H_2 from alkyl radicals. If the thermal decomposition of alkyl radicals is assumed to be accelerated in the dense tracks where local temperature increase is sustained during the reactions, one could expect the simultaneous increases in the yields of H_2 and unsaturated hydrocarbons.

The increases in the yields of unsaturated hydrocarbons were also demonstrated by the experiments on the laser irradiation of diethyl ketone vapor, in which ketone molecules are believed to decompose thermally.

The steep decreases in the yields observed above 40 eV/Å is of great interest, a similar phenomenon has, to the authors' knowledge, not yet been reported. Insofar as the radiation track with a fixed radius is assumed, initial concentrations of excited molecules or radicals formed under the present conditions should exceed the orginal concentration of molecules confined in the track. This may result in the waste of energy endowed from radiations and in the apparent lowering of the yields in the very high LET region.

Similar phenomenon has also been observed in acetone and methyl-ethyl ketone and further studies are in progress.

References

1) M. Imamura, M. Matsui, and T. Karasawa : IPCR Cyclotron Progr. Rep., 4, 119 (1970).
2) M. Imamura, M. Matsui, and T. Karasawa : Bull. Chem. Soc. Japan, 43, 2745 (1970).

8-2. LET Effect in the Rediolysis of Some Organic Liquids

M. Matsui and M. Imamura

The LET effect on the radiolysis yields from various compounds has been a long-term subject in the radiation chemistry. However, owing to the limitation of the radiations available, the range of LET has scarcely exceeded 20~30 eV/Å. Uranium fission fragments have an extraordinarily high LET, but they are always confronted with some inevitable complexities.

We have been employing heavy ions, ^{12}C and ^{14}N, accelerated with the cyclotron to investigate the radiolysis of some organic liquids in the very high LET region. Here we wish to review these results along with a few results by other workers and discuss the general features of the LET effect. In addition to the usual diffusion-kinetics theory, some other factors seem to be required to explain the phenomena observed in the very high LET region.

The results are summarized in Figs. 1 and 2, where the results with benzene and cyclohexane obtained by Schuler[1] and Burns et al.[2] are also included. These figures show variations of the yields of only H_2, the principal gaseous product, as a function of the stopping-power parameter, z.

As is seen from Figs. 1 and 2, $G(H_2)$-values of cyclohexane and methanol show

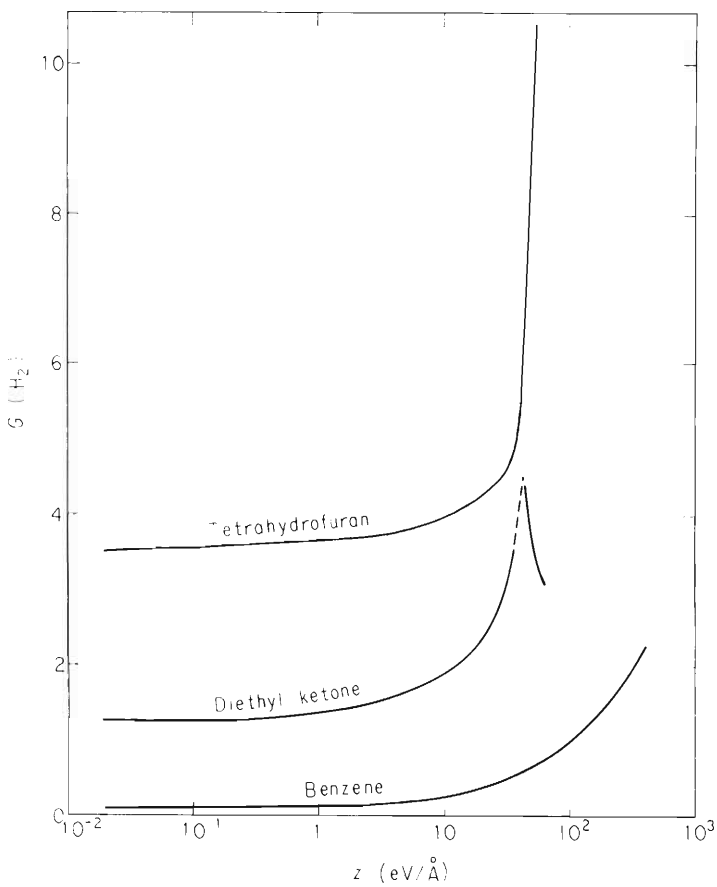

Fig. 1. Variation of G (H_2) with LET (stopping-power parameter, z) for methanol and cyclohexane.

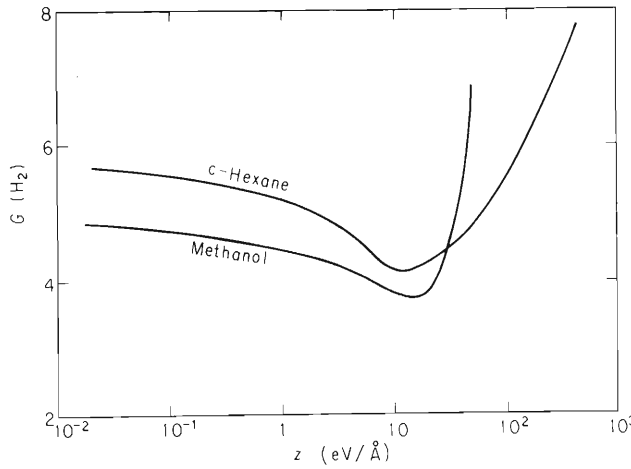

Fig. 2. Variation of G (H_2) with LET (stopping-power parameter, z) for tetrahydrofuran, diethyl ketone, and benzene.

their minima in the vicinity of 10 eV/Å, whereas those of tetrahydrofuran, diethyl ketone, and benzene do not. The former compounds have relatively large radical yields in the γ-radiolysis and the latters have low ones.

For methanol, the γ-yield of solvated electrons has been found to be 2 in G-unit[3] and to decrease with increasing LET. On the basis that the yield of the total ionization in methanol is invariant irrespective of the nature of radiations, the probability of recapturing electrons by positively-charged species in spurs or tracks increases with increasing LET. The recombination has been assumed to give rise to the formation of H-atoms and/or H_2 molecules. The gradual decrease in $G(H_2)$ for methanol cannot be explained by assuming that every recombination of electron produced the excited state, the precursor of H or H_2. Therefore, it is likely to consider that some parts of excited states thus produced may be deactivated without forming H or H_2.

The LET effect in cyclohexane, according to Burns,[2] has been interpreted by the competition of excited molecules. This model, in which LET effects are due to events prior to radical formation, is more successful than the radical model in the LET range less than 10 eV/Å.

On the other hand, in tetrahydrofuran, diethyl ketone, and benzene, most of H_2 are formed molecularly, i.e., in spurs or tracks. Therefore, the variations of $G(H_2)$ with LET below 10 eV/Å may be accounted for by the usual diffusion-kinetics model.

Above several tens of eV/Å, H_2 may be regarded to be produced by quite different modes as stated in the preceding section. In the high LET region, increases in $G(H_2)$ are observed for all compounds irrespective of the different behavior at lower LETs'. This similar dependence with LET may imply an important contribution of thermal spikes which accelerates the decomposition of free radicals. Recently, Voltz[4] observed the opposite variations of radiation-induced luminescence and $G(H_2)$ for toluene in the high LET region. He suggested that this effect may arise from the interaction of transient excited intermediates.

References

1) R. H. Schuler : Trans. Faraday Soc., 61, 100 (1965).
2) W. G. Burns and C. R. V. Reed : ibid., 66, 2159 (1970).
3) H. Seki and M. Imamura : J. Phys. Chem., 71, 870 (1967).
4) R. Voltz : Proc. Intern. Discussion on Progress and Problems in Contemporary Radiation Chemistry, Prague, p. 45 (1971).

8-3. LET Effects on Bacterial Cells

A. Matsuyama, T. Karasawa, T. Takahashi, and F. Masuda

(1) LET effects on cellular radiosensitivities of bacteria

Determinations of relative biological effectiveness (RBE) of different particles accelerated in the cyclotron for the induction of cell death in bacterial cells are still in progress. Bacterial strains used in this study were E. coli B_{s-1} and B/r, M. radiodurans, B. subtilis 168 thymine-requiring mutant and its spores. Vegetative cells were harvested during the log-phase of the bacterial culture and washed with 0.067 M phosphate buffer. As previously described,[1] a monolayer of bacterial cells prepared on a Millipore filter (type HA, 9 mm in diameter) which had been placed on a wet filter pad was irradiated with charged particles such as protons, α-particles, carbon-, nitrogen-, and oxygen-ions in air at room temperature. Two sets of experimental results obtained with E. coli B_{s-1} and B. subtilis spores are shown in Fig. 1.

The results indicate that the RBE largely varies with different LETs and types of ionizing particles. For all strains, the RBE of different particles were found to be different at the same total LET (L_∞). The $1/D_{37}$ value as a measure of RBE increased in the increasing order of α-particles, carbon-, nitrogen-, and oxygen-ions at the same L_∞. This increase in RBE observed in the energy range higher than unity in MeV per

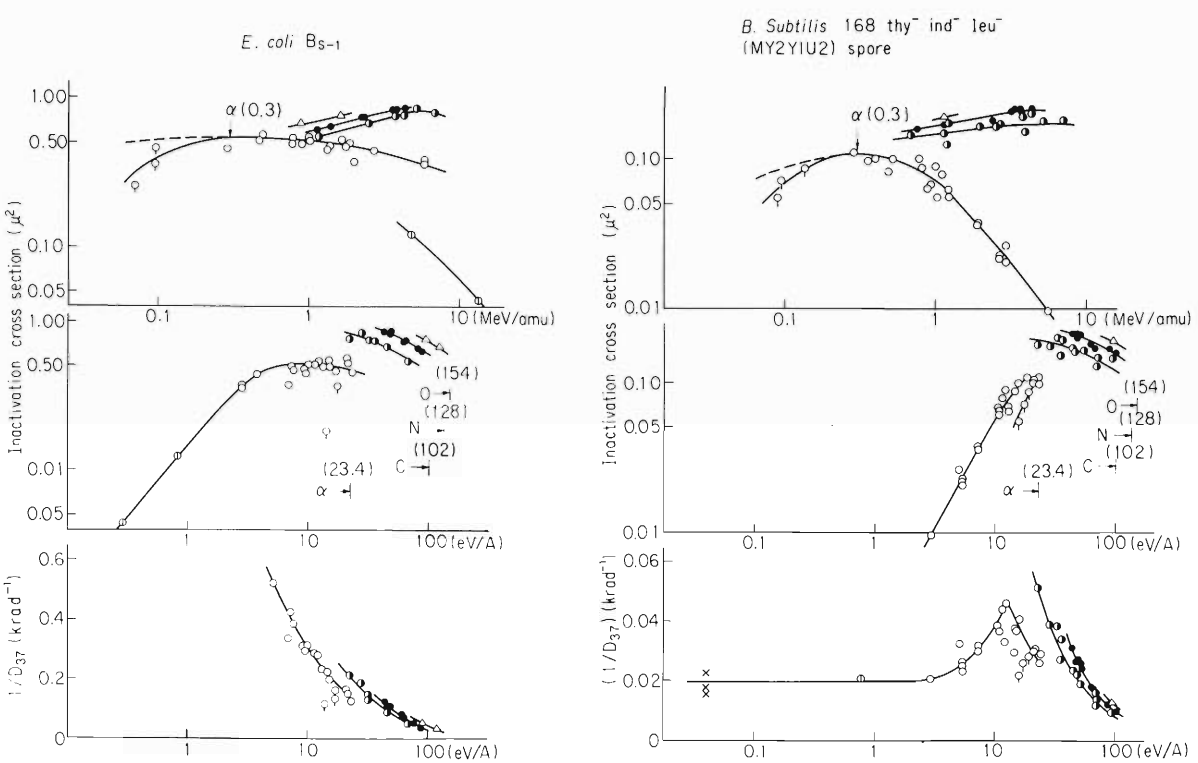

Fig. 1. Radiosensitivity and inactivation cross section as a function of L_∞ (eV/Å) or energy per nucleon (MeV/amu).

atomic mass unit (amu) can be explained by the δ -ray effect as described below.

The inactivation cross section for ionizing particles was estimated in cases of four strains which gave an exponential-type survival curve, except M. radiodurans. For α-particles, the inactivation cross section increased in the very lower energy region and then showed a remarkable decrease in the region more than 1 MeV/amu. The maximum value of the inactivation cross section for α-particles was found in cases of all four types of bacteria at the same energy (0.3 MeV/amu) which gave the maximum L_∞ in water (23.4 eV/Å). The value of the maximum inactivation cross section for α-particles was found to be smaller than the projected area of a nuclear body in bacterial cells observed by electron microscopy and it appeared to depend upon the capacity of the DNA repair.

In the relationship between L_∞ and $1/D_{37}$, a peak of the curve representing this relationship was observed at around 6 eV/A with E. coli B/r depending upon the age of the bacterial culture. This fact may indicate that the two-hit model is required to interpret the occurrence of this peak from a viewpoint of the target theory. Further determinations in the very low energy range (less than unity in MeV/amu) are now undertaken for heavy ions.

In the case of M. radiodurans,[2] the shoulder dose and D_{10} value for the exponential slope of a sigmoidal survival curve were similarly decreased at high LET.

(2) Analysis of data obtained with E. coli B_{s-1}

According to Dolphin and Hutchinson,[3] the inactivation cross section S can be represented by

$$S = S_0 + \frac{fL\rho V}{F\varepsilon} ,$$

where S_0 is the effective area of the target, f the fraction of energy dissipated by δ-electrons which depends upon cut-off energy W, L the total LET for the medium of $\rho = 1$, ρ the density of the medium, V the sensitive volume of the target molecule, 1/F the overlapping factor for the δ-electrons, and ε the energy per primary ionization (ε = 72 eV).

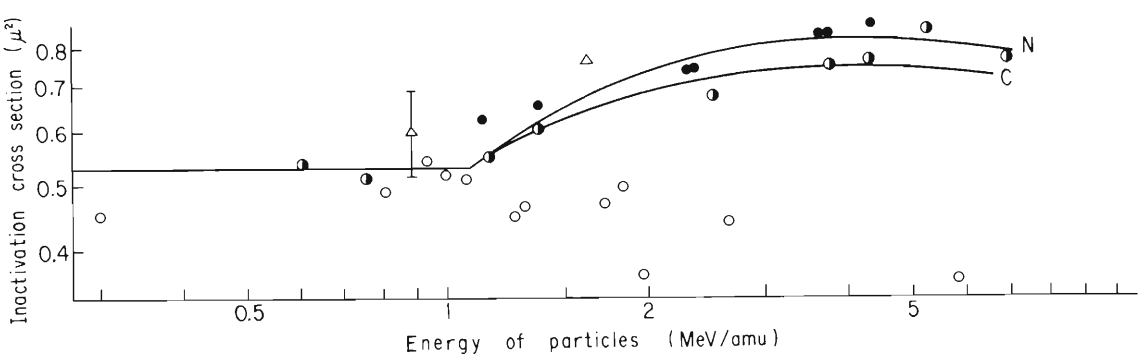

○ α-particles, ◑ Carbon ions, ● Nitrogen ions, △ Oxygen ions
Real lines indicate the calculated curves for carbon ions (C) and nitrogen ions (N).

Fig. 2. Inactivation cross section of E. coli B_{s-1} as a function of energy per nucleon.

The observed inactivation cross section was fairly well represented when the following constants and values of parameters were adopted (Fig. 2) : W = 2.75 keV, ρ = 1.71, V = $3.8 \times 10^{-3}\ \mu^3$, ε = 72 eV, 1/F = 1/14.0. The adopted value for the overlapping factor was less than that found for ^{60}Co γ-rays (1/F = 1/5.9).

References

1) A. Matsuyama, T. Karasawa, S. Kitayama, and R. Takeshita : IPCR Cyclotron Progr. Rep., 3, 101 (1969).
2) F. Suhadi, S. Kitayama, Y. Okazawa, and A. Matsuyama : Agr. Biol. Chem., 35, 1644 (1971) ; Radiat. Res., 49, No. 1(1972)
3) G. W. Dolphin and F. Hutchinson : Radiat. Res., 13, 403 (1960).

9. SOLID STATE PHYSICS

9-1. Electron Microscopic Observation on Helium Bubbles in Aluminum Irradiated by Alpha-Particles

H. Sakairi, E. Yagi, H. Shiraishi,
T. Karasawa, and R. R. Hasiguti

Observation on He bubbles in aluminum irradiated by alpha-particles is being continued. The method of He injection was improved so that the He atoms were distributed nearly uniformly in the specimens. The results obtained by the new method were different from those of the previous ones, that is, the size of the bubbles became smaller and the temperature for the bubble formation higher. Reasons for these have not been clarified.

The average size and the density of observable bubbles in each specimen are listed in Table 1. The helium contents calculated are also presented and compared with those calculated from the irradiation dose. Both values agree in an order of magnitude.

Fine bubbles and gross bubbles can appear in the grains and along the dislocations and on the grain boundaries. Some correlations exist between the various appearances of bubbles, which can been seen from Table 2.

Table 1. Calculation of the average bubble diameter and the bubble density. Helium content was derived from these data. Last column shows the total number of the bubbles used for the calculation.

Implant. He (ppm)	Cold work (%)	Heat treatment (^{o}C)	(h)	Aver. dia. (Å)	Density ($10^{13}cm^{-3}$)	Calculated He cont. (ppm)	N_b
43	0	550	100	142	4.9	34	337
43	0	600	1	157	2.0	16	138
43	0	600	1	183	3.0	29	408
43	0	600	1	1650	0.024	18	93
43	0	600	3	692	0.23	38	304
43	0	600	3	4140	0.010	49	36
43	0	600	100	168	2.8	16	145
43	0	645	1	167	2.4	19	182
43	0	645	1	142	4.8	27	653
43	0	645	1	814	0.22	39	69
87	0	550	1	70	6.0	11	198
87	0	600	1	99	9.8	34	1136
43	8	600	1	180	0.71	7	35
43	8	645	1.5	591	0.23	24	308

Table 2. Frequency of the bubble formation in the matrix and on some defects for the various treatments of the samples.

He cont. (ppm)	Tension (%)	Heat treatment (°C)	Heat treatment (h)	N. of* Speci.	N. of** Photo.	(A)*** Matrix Fine	(A)*** Matrix Gross	(B)**** Dislocation Fine	(B)**** Dislocation Gross	(C)***** Boundary Fine	(C)***** Boundary Gross
43	0	500	1	2	13	0	1	0	0	0	0
		550	1	4	32	0	3	0	0	0	0
		550	100	1	10	6	0	0	0	2	0
		600	1	3	82	28	22	6	9	0	6
		600	3	1	24	0	11	2	0	0	7
		600	100	2	32	5	1	4	0	1	0
		645	1	3	39	15	12	8	0	0	3
87	0	550	1	1	22	0	0	0	0	0	0
		600	1	2	35	19	2	2	2	0	0
		600	10	1	22	11	0	6	0	2	0
		600	100	1	33	0	26	0	10	0	18
		645	1.5	2	47	27	4	17	2	5	0
43	8	500	1	2	17	0	0	1	0	0	0
		550	1	3	29	0	0	0	0	0	0
		600	1	4	70	2	0	0	0	0	0
		600	10	1	18	4	1	0	0	0	0
		645	1.5	1	28	0	6	0	3	0	5

* The number of the specimens observed.

** The number of the photographs taken.

*** The column under "Fine" shows the number of the photographs in which the homogeneous nucleation of helium bubbles within the grain was observed. Bubbles of this type seem to be very fine. The column under "Gross" shows the number of the photographs in which random distribution of gross helium bubbles was observed within the grain.

**** The column under "Fine" shows the number of the lines of helium bubbles arranged in a row. The column under "Gross" shows the total number of the dislocations on which the bubbles larger than in the grain interior were located.

***** The column under "Fine" shows the number of the total number of grain boundaries on which those bubbles were located, the size of which was roughly the same as those distributed randomly in the grain interior. The column under "Gross" shows the total number of grain boundaries on which the bubbles larger than in the grain interior were located.

The characteristic features of the bubbling are summarized as follows:

(1) No bubble appears unless the annealing temperature reaches 550°C. This temperature is rather high compared with that for Al-Li alloys irradiated by pile neutrons.

(2) The bubbles are divided into two groups, fine bubbles and gross ones. The absence of bubbles of an intermediate diameter does not occur in Al-Li alloys.

(3) There are almost no gross bubbles in the sample in which many fine bubbles appear and vice versa. Especially in the sample in which no fine bubble can be found in the grain interior, many gross bubbles appear on the grain boundaries. In both cases, He content which is calculated from observed diameter and density of bubbles agree roughly with the content of injected He.

(4) In some samples the fine bubbles can survive with a density of $10^{13}cm^{-3}$ near the melting temperature.

(5) When the He content is increased, the density of the bubbles increased but their diameter is left unchanged or slightly decreases.

(6) In the samples which are strained after the He injection, there are few fine bubbles, especially around the sub-boundary dislocation network. This tendency is prominent in the samples which are heat-treated near the melting temperature.

Under normal conditions the bubbles in a grain interior cannot grow exceeding 200Å in diameter. As the content of He contributing to the bubble formation is estimated to be nearly equal to that of the injected He, it is evident that the growth must be stopped by the exhaustion of He in the matrix. Under these circumstances some mechanisms, such as random drift of the bubbles leading to the coalescence of them, must operate for further growth of the bubbles. There are some examples, however, that the fine bubbles can present stably near the melting temperature. Therefore we must consider that the random drift of bubbles does not occur under usual conditions and that the formation of the gross bubbles are helped by another mechanism.

It is remarkable in the samples strained plastically, that many gross bubbles can be found on the grain boundaries when there is no fine bubble in the grain interior. It is naturally considered that the fine bubbles are swept away by the migration of grain boundaries or dislocations.

Several examples that the fine bubbles form a line with no dislocation, suggest that an interaction between the bubbles and the dislocations is not strong. Such lines of bubbles should be a trace of the dislocation, by which the bubbles could once be pulled when they were finer.

There are also the examples of gross bubbles which are condidered to be left behing by the migrating grain boundaries. It can be said that the pinning of the dislocations and the boundaries by the bubbles is not strong in pure aluminum.

9-2. Point Defects in Irradiated Copper and Cu_3Au

H. Sakairi, E. Yagi, A. Koyama,
T. Karasawa, and R.R. Hasiguti

In the irradiation experiments of metals, the physical properties of pure metals are not affected by atomic exchange replacements, while those of ordered alloys are changed drastically because of the change of the degree of order induced by atomic exchange replacements. The irradiation study of ordered alloys, therefore, is expected to give additional information which cannot be obtained by the studies of pure metals.

In a previous report[1] two important experimental results were described that (1) about ten times larger resistivity is introduced by irradiation in the ordered copper-gold alloy as compared with that introduced in copper, and (2) the resistivity change of the ordered alloy is far larger than that of copper in the stage III annealing.* It is considered that the kind and the concentration of lattice defects brought about under the same irradiation conditions are nearly the same both in the alloy and copper. This means that the large differences in the irradiation induced resistivity and its change in stage III described above are due to the changes in the degree of order in the alloy. In this report the damage introduction rates precisely determined are presented and on the basis of these the nature of the stage I, II, and III defects are discussed.

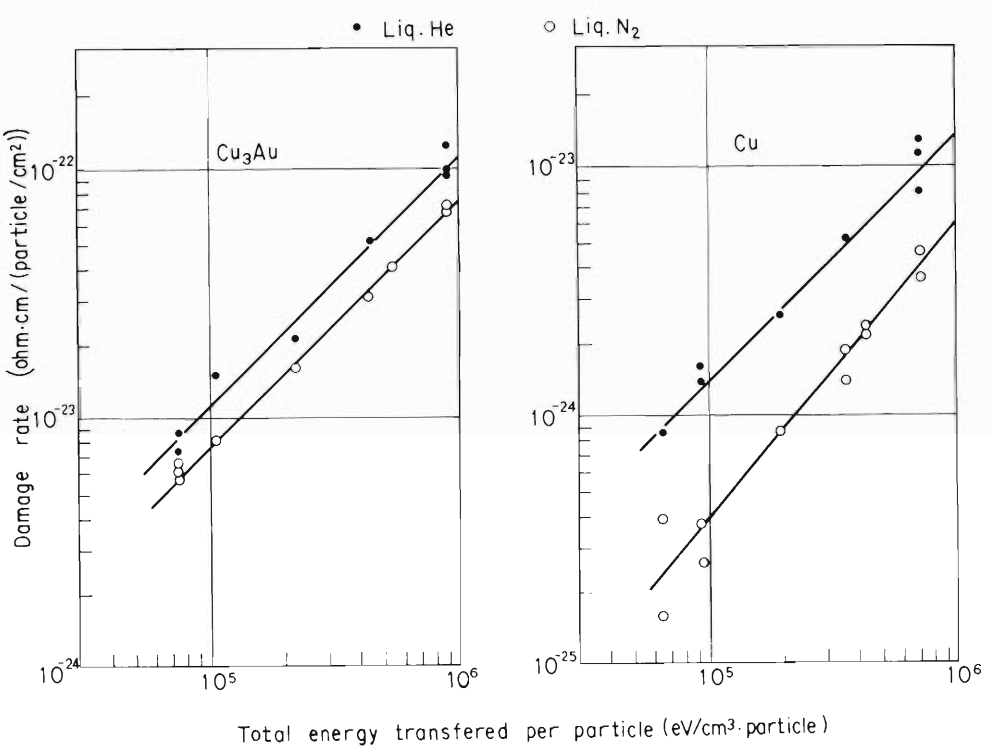

Fig. 1. Damage rate at Liq. He and Liq. N_2 temperature.

* The labelling of stages will be made as follows: stage I below 70°K, stage II between 70° and 220°K, and stage III between 220° and 300°K.

Figure 1 shows the damage rate expressed in the unit of $\Omega \cdot cm/(irradiation\ particles/cm^2)$ as a function of the total energy transferred to all the primary knocked-on atoms by an incident particle expressed in the unit of eV/cm^3 per incident irradiation particle. The ratio of the damage rate of Cu_3Au to that of copper for the irradiation at liquid helium temperature is about 8 independently of the total energy transferred. As it is considered that the resistivity change due to Frenkel defects is nearly the same both in Cu_3Au and copper under the same irradiation conditions, the ratio of the number of pairs of wrongly sited Cu and Au atoms to the number of Frenkel pairs would be obtained to be 10. Here it is assumed that the resistivity is changed as 2.7 and 1.9 $\Omega \cdot cm/\%$, due to 1 atomic % of Frenkel pairs and of wrongly sited atomic pairs, respectively.

The results shown in Fig. 1 can be also used to estimate the size of stage I annealing both in the alloy and copper. The fraction of stage I annealing is estimated from the damage rates for irradiations at liquid helium and liquid nitrogen temperatures as follows:

$$f = \frac{\Delta\rho(\mathrm{He}) - \Delta\rho(\mathrm{N})}{\Delta\rho(\mathrm{He})} \quad .$$

It is 0.6～0.7 for Cu and 0.3 for Cu_3Au. The stage I annealing of Cu_3Au contains contributions both from defect annealing and order recovery. If the extent of defect annealings are assumed to be the same for both the alloy and copper, the fraction of defect annealing in the alloy can be determined and the ratio of the number of wrong pairs recovered in stage I to the number of defects (counted in the unit of Frenkel pair) annealed in stage I is obtained as follows:

$$\frac{n^{\mathrm{I}}_{\text{wrong pair}}}{n^{\mathrm{I}}_{\text{defect}}} = 3 \sim 4 \quad .$$

This shows that during stage I annealing the stage I defects migrate to annihilate, during which the ordering exchange replacement is brought forth, which makes three or four wrong pairs disappear per one migrating defect.

The isochronal annealing curves of Cu_3Au and copper irradiated by alpha particles at liquid nitrogen temperature are shown in Fig. 2 in the previous report,[1] from which the ratio of the number of wrong pairs recovered in stage II to the number of defects annealed in stage II is obtained:

$$\frac{n^{\mathrm{II}}_{\text{wrong pair}}}{n^{\mathrm{II}}_{\text{defect}}} = \sim 3 \quad .$$

It is remarkable that the ratio of wrong pairs to defects in stage II is the same as that in stage I. This shows that the migrating defects are same in stages I and II at least in their abilities to order wrongly sited atoms in alloy.

The results of stage III annealing shown in Figs. 1 and 2 in the previous report, are most striking in this experimental study. The detailed numerical values of five sets of experiments were shown in Table 1. The ratio of wrong pairs to defects in stage III is calculated from the results of each sets except the last in Table 1 as follows:

Table 1. Comparison of stage III temperature of Cu_3Au and Cu.

Irradiation			Resistivity increase		Stage III temperature		
Particle	Energy (MeV)	Dose ($10^{16}/cm^2$)	Cu_3Au ($10^{-6}\Omega\cdot cm$)	Cu ($10^{-8}\Omega.cm$)	Cu_3Au (^oK)	Cu (^oK)	$\frac{T_{III}(Cu_3Au)}{T_{III}(Cu)}$
alpha	16.5	2.7	1.77	4.0	278	259	1.07 ± 0.01
alpha	36.0	2.4	0.84	2.5	275	260	1.06 ± 0.01
alpha	28.0	0.83	0.58	2.2	276	260	1.06 ± 0.01
proton	3.5	3.0	0.37	1.93	283	266	1.06 ± 0.01
proton	8.0	1.20	0.09	0.38	293	275	1.06 ± 0.02

$$\frac{n^{III}_{wrong\ pair}}{n^{III}_{defect}} = 34 \sim 48 \quad .$$

This is an extraordinary value, which is about ten times larger than that for stage II or I. In the case of the last set in Table 1 the ratio is about 140. This means that the migration of stage III defects is ten times or more effective in ordering wrongly sited atoms in the alloy than that of defects in stage I or II.

Reference

1) H. Sakairi, E. Yagi, T. Karasawa, and R. R. Hasiguti : IPCR Cyclotron Progr. Rep., 4, 140 (1970).

9-3. Polarized Positron Annihilation in Ferromagnetic Nickel

N. Shiotani, T. Okada, H. Sekizawa,
S. Ambe, T. Mizoguchi, and T. Karasawa

(1) Introduction

As a consequence of the non-conservation of parity in beta decay the positrons are partially polarized along their direction of motion. When the positrons get into metals, two-quantum annihilation can take place only from the singlet state of the positron-electron pair and two annihilation radiations are emitted in nearly opposite directions. From the conservation of momentum the angular correlation of two annihilation radiations reflects the momentum distribution of annihilated positron-electron pairs. Since in metals the positrons are thermalized before annihilation, the angular correlation measurement can be used to distinguish the momentum distribution of majority spin electrons from that of minority spin electrons in ferromagnetic metals. Such investigations have been reported[1)~5)] on single crystal Fe, polycrystals Fe and Ni, single crystal Ni, and single crystal Gd.

We report here experiments on single crystal of ferromagnetic Ni oriented in the (110) plane with greater accuracy and better angular resolution than existing experiments cited above.

(2) Experimental

The mechanical equipment and the ^{90}Nb source preparation method were the same as described earlier.[6),7)]

(i) Specimen

Nickel of 99.999 % was melted and grown into a single crystal in a vacuum furnace

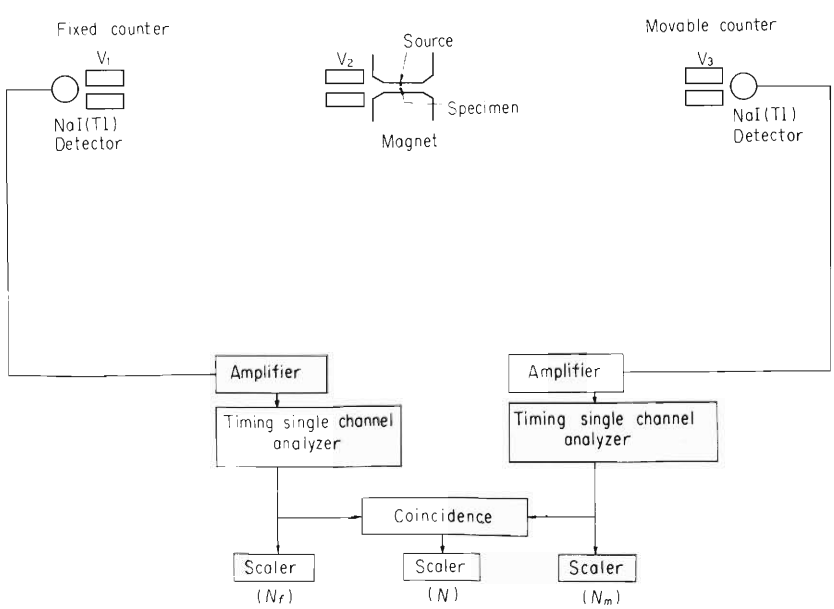

Fig. 1. Schematic diagram of the system.

with a built-in proper temperature gradient. The single crystal was oriented and cut into a (110) plate. The surface was first chemically etched to remove distortion introduced during mechanical cutting, then finished by electropolishing. The Laue spots did not reveal any distortion in our specimen.

(ii) Slit system and specimen alignment

The three vertical slits, V_1, V_2, and V_3, of 2.4 mm, 1.2 mm, and 2.4 mm widths respectively, were used to collimate the annihilation γ-rays as shown in Fig. 1. The angular resolution defined by the slit system was measured to be 0.66 mrad. The specimen was placed exactly on the axis of the slit system. The (110) plane was parallel to the axis. The source was set to face the specimen. Both the source and the specimen were in a magnetic field of 6 kOe which orients the electron spins in the specimen either parallel or antiparallel to the direction of the positron beam.

The direction of the annihilation γ-rays from the specimen is parallel to (110) and the component of the momentum examined is parallel to $[1\bar{1}0]$. The direction of the magnetization of the specimen is either parallel or antiparallel to $[1\bar{1}0]$ which is also the direction of the positron beam.

(iii) Electronic circuits

The block diagram of the electronic circuits is shown in Fig. 1. The resolving time was 500 nsec. During the measurements, the pulse height of the amplifiers was examined every 6 ~ 12 h and the levels of the single channel analyzers were adjusted so that the coincidence was properly taken between two annihilation γ-rays.

(iv) Coincidence counting rate

The coincidence counting rate $N(\theta, t)$ was measured at an angle θ and the time t which was defined to be the midpoint of the time interval of a counting. The rate $N(\theta, t)$ includes the random coincidence rate $N'(\theta, t)$, which is either measurable by setting the movable counter at a sufficiently large angle position or can be calculated from the following relation:

$$N'(\theta, t) = 2\tau N_m(\theta, t) N_f(\theta = 0, t),$$

where τ is the resolving time, $N_m(\theta, t)$ is the counting rate of the movable counter at the angle θ and at the time t, and $N_f(\theta=0, t)$ is the counting rate of the fixed counter at the same time. Thus the time-independent angular correlation $N^O(\theta)$ is given by

$$N^O(\theta) = \left[N(\theta, t) - N'(\theta, t)\right] e^{\lambda t},$$

where $\lambda = 0.693/T$ and T=14.7 h for ^{90}Nb. The final counting rate was obtained by summing up the counting rates of several runs with proper weights.

(3) Results and discussion

Figure 2 shows the observed angular correlation curves taken under the following conditions : The direction of the annihilation γ-rays is parallel to $[1\bar{1}0]$ and the component of the momentum examined is parallel to $[110]$;
and

(i) The direction of magnetization of the specimen is parallel to the direction of polarization of the positron spins.

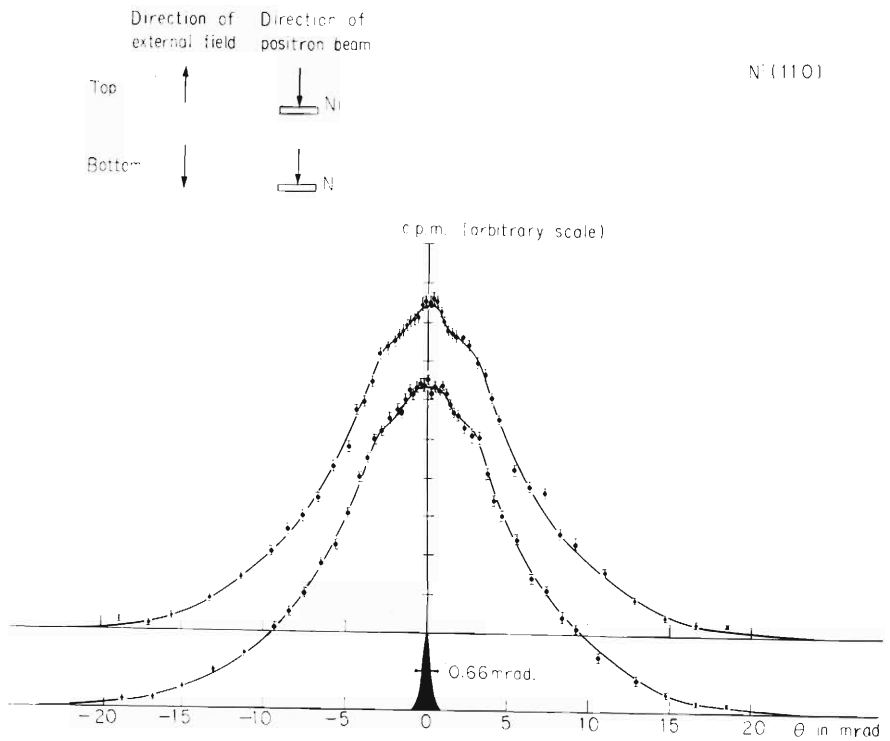

Fig. 2. Angular correlation for a (110) crystal of Ni. The shaded curve in the figure shows the observed angular resolution curve.

(ii) The direction of magnetization of the specimen is antiparallel to the direction of polarization of the positron spins.

Since the volume in the momentum space filled with electrons is exactly the same for both cases, the curves are normalized to give an equal area.

Both curves show a hump around $\theta = 0$ mrad., the shape of which depends on the direction of magnetization of the specimen, and a sharp break near $\theta = 3.2$ mrad. and a slight break near $\theta = 7.3$ mrad.

The (110) -Brillouin zone boundaries occur at $\theta = 7.31$ mrad. The above-mentioned slight break near $\theta = 7.3$ mrad. is ascribed to the (110) -Brillouin zone boundaries.

According to the energy band calculations[8),9)] the Fermi surface consists of four sheets for the minority spin bands and one in the majority spin bands. The minority spin sheets consist of small hole surfaces at the [100] points in the 3rd and the 4th bands, and a closed surface with protrusions along the [110] directions in the 5th band, and a closed surface of nearly rectangular shape with protrusions along the [100] directions and [111] directions in the 6th band. The majority spin sheet is a multiply-connected surface with necks at the [111] points.

The minority spin surface in the 6th band cuts the [110] axes near $\theta = 3.1$ mrad. and the majority spin surface in the 6th band cuts the same axes near $\theta = 3.6$ mrad. We may thus expect that a break would occur between $\theta = 3.1$ mrad. and $\theta = 3.6$ mrad. on the angular correlation curve.

The sharp break near $\theta = 3.2$ mrad. in the present data seems to correspond to the one mentioned above.

The hump around $\theta = 0$ mrad. reflects the existence of the necks at the [111] points in the majority spin surface and the protrusions along the [110] and the [100] directions in the minority spin surfaces.

The authors are grateful to Dr. S. Okano and the members of the Radiation Laboratory for valuable suggestion and kind permission to use their electronic facilites.

References

1) S.S. Hanna and R.S. Preston : Phys. Rev., 109, 716 (1958).
2) P.E. Mijinarends and L. Hambro : Phys. Letters, 10, 272 (1964).
3) T.W. Mihalisin and R.D. Parks : Phys. Rev. Letters, 18, 210 (1967).
4) T.W. Mihalisin and R.D. Parks : Solid State Commun., 7, 33 (1969).
5) C. Hohenemser, J.M. Weingart, and S. Berko : Phys. Letters, 28A, 41 (1968).
6) M. Saito, T. Okada, N. Shiotani, H. Sekizawa, and T. Karasawa : IPCR Cyclotron Progr. Rep., 2, 150 (1968).
7) N. Shiotani, S. Ambe, T. Okada, and T. Karasawa : ibid., 4, 146 (1970).
8) S. Wakoh and J. Yamashita : J. Phys. Soc. Japan, 19, 1342 (1964).
9) J.W.D. Connolly : Phys. Rev., 159, 415 (1967).

10. I PRODUCTION AND ITS APPLICATIONS

10-1. Production of Radioisotope for Medical and Agricultural Use

M. Okano, T. Nozaki, T. Karasawa,
A. Shimamura, K. Yuita, and T. Ido

The production of radioisotope for medical and agricultural use has been continued. The separation of ^{54}Mn formed simultaneously with ^{52}Fe in the chromium target bombarded by ^{3}He- or α-particles was studied, and the method of processing of ^{111}In for diagnostic use was improved to be suitable for the routine supply. Efforts have been made for the preparation of ^{18}F-labelled organic compounds. Also, ^{43}K was produced by the α-particle bombardment of streaming argon and was supplied to Kyushu University.

^{54}Mn was separated as follows. After the extraction of ^{52}Fe, gaseous HCl was introduced into a solution of the bombarded chromium until its HCl concentration became about 11 N. The solution was then passed through a column of anion exchange resin; ^{54}Mn was adsorbed in it, but most part of the chromium and ^{58}V remained in the effluent. The ^{54}Mn was then eluted with water, and the eluate was brought to dryness. After addition of H_2SO_4, HNO_3 and water to the residue, the ^{54}Mn was distilled in a stream of gaseous azeotropic HNO_3 - H_2O, the distillate being received by water containing a trace of H_2O_2. Thus, ^{54}Mn was separated free from carrier and salt in a good yield. The product was supplied to an agricultural laboratory.

Millicurie amounts of ^{18}F-labelled benzotrifluoride and cholesteryl fluoride were prepared. They were injected into animals, and their behavior was examined by a scintillation camera. The results, however, were not satisfactory, because most portion of the activity was trapped in the lungs. Efforts will be made to obtain the products of higher specific activity. The preparation of some ^{18}F-compounds less poisonous and less active physiologically is now being studied.

11. RADIATION MONITORING

11-1. Routine Monitoring

K. Koda, I. Sakamoto, and I. Usuba

The results of measurements made during a period from April 1970 to March 1971 on the residual activities of the machine, the contamination on the floor of the cyclotron room and the personnel monitoring are described.

(1) Residual activities of machine and floor contamination

The residual activities except for that of tritium (see below) seemed to have reached an equilibrium and gave a maximum dose-rate value of 10^4 mR/h at the septum just after machine shutdown.

The surface contamination on the floor of the cyclotron room was kept to be about $10^{-5} \mu Ci/cm^2$ similarly as in the preceding period.

(2) Personnel monitoring

The accumulated dose of external exposure during the present period of all cyclotron workers issued with the film badge are shown in Table 1. Both average and maximum values of the annual exposure dose per person were a little less than those in the preceding period.

Table 1. Accumulated dose distribution of the cyclotron workers from April 1970 to March 1971.

Dose (mrem)	10～100	101～300	301～1 000	>1 000
Operators			6	
Nuclear physicists	6	6	4	
Accelerator physicists	1	1	3	1
Physicists of other fields	4	4		
Radiochemists	2	1	2	2
Radiation chemists	2			
Biological chemists	2			
Health physicists	2			

Average annual dose per person : 299 mrem.
Maximum annual dose : 1090 mrem.

11-2. Individual Monitoring for Internal Contamination with Tritium

K. Koda, I. Sakamoto, and I. Usuba

During the preceding period, two test runs of triton acceleration have been carried out using 1 and 100 Ci of tritium gas, respectively. The results of tritium monitoring in these runs were reported previously. [1)]

In the present period, the third run was done with 700 Ci of tritium gas from Dec. 21 to 26, 1970. As described by Kohno et al.,[2)] a tritium concentration of as much as $10^{-3}\mu$Ci/cc was found in the air inside the acceleration chamber and other parts of the cyclotron just after the exposure of the chamber to the atmosphere for overhaul. The air contamination of such level was observed even 9 months after the triton acceleration in spite of routine use of the machine with inactive gases during that time, and this implies slow release of tritium, probably in the form of tritiated water, from the inner wall of the machine which had been exposed to the tritium gas.

Tritium intakes occurred to several workers who were engaged especially in filament replacement during the triton acceleration or in overhaul after the machine shutdown. The amount of intake in these operations was assessed for each worker from the tritium concentration in urine using the equation as recommended by ICRP. [3)] The data are shown in Table 1.

The effective half-life of tritium in the human body estimated from the results of day-by-day urine analyses was found to be about 9 days as shown in Fig. 1.

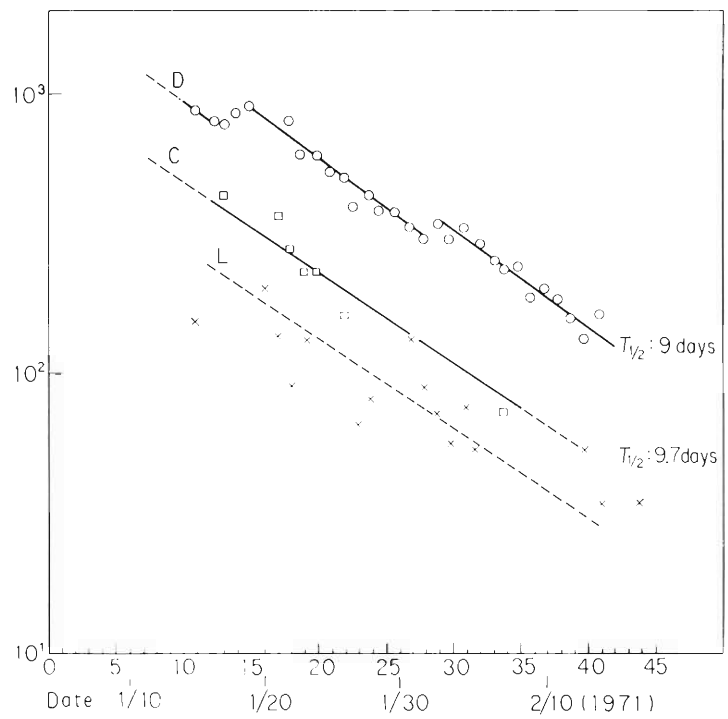

Fig. 1. Effective half-life of tritium in the human body.

Table 1. Tritium intake and total internal dose of cyclotron workers.

		Tritium intake (μCi)				Total dose (mrem)
		Dec. 21~26, '70	Jan. 13~20 '71	Mar. 1~2	Mar. 11~13	
		Loading and collection of tritium gas, filament replacement, etc.	Overhaul	Overhaul	Overhaul	
Accelerator physicists	A	180		41	5	38
	B		560			94
	C	120	430			92
	D	350	3230			597
Operators	E			240		40
	F			260		44
	G				24	4
Nuclear physicists	H	1680		26		285
	I	1450		25	14	250
	J	520		45		95
Health physicists	K		260			44
	L	240	250	52	32	97

References

1) I. Kohno et al. : IPCR Cyclotron Progr. Rep., 4, 11 (1970).
2) I. Kohno et al. : This report, p. 16.
3) Report of Committee IV on Evaluation of Radiation Doses to Body Tissues from Internal Contamination due to Occupational Exposure, ICRP Publication 10, Pergamon Press, p. 29 (1968).

12. LIST OF PUBLICATIONS

1) M. Aratani and N. Saito : "Characterization and Discussion of Charge Spectrometer by Means of Ion Beam Experiment", Radioisotopes, 19, 22 (1970).

2) M. Aratani and N. Saito : "Mass Spectroscopic Studies on the Mechanism of Ionization of Atoms Formed as a Result of Radioactive Decay Process. I", Mass Spectros., 18, 906 (1970).

3) S. Nagamiya, T. Nomura, and T. Yamazaki : "Stroboscopic Determination of the Magnetic Moment of the 8^+ Isomeric State of ^{208}Po", Nucl. Phys., A159, 653 (1970).

4) M. Aratani and N. Saito : "The Mass Spectrometry Using Radioisotopes as an Ion Source", Mass Spectros., 19, 195 (1971).

5) H. Sekizawa, T. Okada, S. Okamoto, and F. Ambe : "Mössbauer Effect of ^{61}Ni in Spinel Type Magnetic Oxides", J. de phys., 32, C 1 - 326 (1971).

6) T. Nozaki, Y. Makide, Y. Yatsurugi, N. Akiyama, and Y. Endo : "A New Radio-Tracer Technique for the Evaporation Study of Light Elements from Molten Silicon", Int. J. Appl. Radiat. Isotopes, 22, 607 (1971).

7) S. Nagamiya, T. Katou, T. Nomura, and T. Yamazaki : "Magnetic Moments of the 8^+ Isomeric States of ^{90}Zr and ^{92}Mo", J. Phys. Soc. Japan, 31, 319 (1971).

8) T. Nomura, T. Yamazaki, S. Nagamiya, and T. Katou : "Magnetic Moment of the Lowest 6^+ State in ^{42}Ca and Effects of the Deformed States", Phys. Rev. Letters., 27, 523 (1971).

9) S. Nagamiya and T. Yamazaki : "Evidence of Anomalous Orbital Magnetism of the Nucleon and the Mesonic Exchange Effect", Phys. Rev., C4, 1961 (1971).

10) S. Nagamiya and T. Inamura : "Isomeric States in Neutron-Deficient Po-Isotopes (A = 200 ~ 203) Studied by (HI, xnγ) Reactions", Nucl. Phys., A182, 84 (1972).

11) T. Inamura, A. Hashizume, T. Katou, and Y. Tendow : "Identification of Neutron Deficient Isotopes ^{100}Ag and ^{104}In", J. Phys. Soc. Japan, 30, 884 (1971).

12) I. Kohno, S. Nakajima, T. Tonuma, and M. Odera : "Elastic Scattering of Carbon and Nitrogen Ions", J. Phys. Soc. Japan, 30, 910 (1971).

13) F. Suhadi, S. Kitayama, Y. Okazawa, and A. Matsuyama : "Isolation of Radio-sensitive Mutans of Micrococcus radiodurans", Agr. Biol. Chem., 35, 1645 (1971).

14) T. Yamazaki and S. Nagamiya : "Unstable Nuclear Magnetic Probes (in Japanese)", Solid State Phys., 6, 323 (1971).

15) T. Yamazaki : "Nuclear Magnetic Moment (in Japanese)", Buturi, 26, 637 (1971).

16) S. Yamaji : "The Manual of the Code for the form Factor Computation of the Two-Nucleon Transfer Reaction", Sci. Papers I.P.C.R., 65, Nos. 3 - 4, 79 (1971).

17) F. Suhadi, S. Kitayama, Y. Okazawa, and A. Matsuyama : "Isolation and Some Radiobiological Properties of Mutants of Micrococcus radiodurans Sensitive to Ionizing Radiations", Radiat. Res., 49, No. 1 (1972).

13. LIST OF PERSONNEL

IPCR Cyclotron Administration Committee

HAMADA Tatsuji 浜田達二 (Chairman)
KUMAGAI Hiroo 熊谷寛夫
IMAMURA Masashi 今村 昌
KAMITSUBO Hiromichi 上坪宏道
KARASAWA Takashi 唐沢 孝
MATSUDA Kazuhisa 松田一久
MATSUYAMA Akira 松山 晃
NOZAKI Tadashi 野崎 正
SAITO Nobufusa 斎藤信房
SAKAIRI Hideo 坂入英雄
SEKIZAWA Hisashi 関沢 尚

Managers of Users Group

HAMADA Tatsuji 浜田達二
NOZAKI Tadashi 野崎 正
ODERA Masatoshi 小寺正俊

IPCR Cyclotron Operating Personnel

Machine Group

HEMMI Masatake 逸見政武
INOUE Toshihiko 井上敏彦
MIYAZAWA Yoshitoshi 宮沢佳敏
SHIMAMURA Akira 島村 晃
TONUMA Tadao 戸沼正雄

Operation

FUJITA Shin 藤田 新
IKEGAMI Kumio 池上九三男
KAGEYAMA Tadashi 影山 正
KOHARA Shigeo 小原重夫
NAKAJIMA Hisao 中島尚雄
OGIWARA Kiyoshi 荻原 清
TERAJIMA Osamu 寺島 為

Scientific and Engineering Personnel

Cyclotron Lab.

KUMAGAI Hiroo 熊谷寛夫
CHIBA Yoshiaki 千葉好明
FUJISAWA Takashi 藤沢高志
FUJITA Jiro 藤田二郎
HEMMI Masatake 逸見政武
HIRUTA Kotaro 蛭田幸太郎
INAMURA Takashi 稲村 卓
INOUE Toshihiko 井上敏彦
KAMITSUBO Hiromichi 上坪宏道
KARASAWA Takashi 唐沢 孝
KOHNO Isao 河野 功
MATSUDA Kazuhisa 松田一久
MIYAZAWA Yoshitoshi 宮沢佳敏
MOTONAGA Shoshichi 元永昭七
NAGAMIYA Shoji 永宮正治
NAKAJIMA Shunji 中島諄二
NAKANISHI Noriyoshi 中西紀喜
ODERA Masatoshi 小寺正俊
SHIMAMURA Akira 島村 晃
TAKEDA Shigeru 竹田 繁
TONUMA Tadao 戸沼正雄
YAMAJI Shuhei 山路修平
YAMAZAKI Yoshishige 山崎良成
YOSHIDA Fusako 吉田房子
WADA Takeshi 和田 雄

(Visitors)

FUJINO Takeo 藤野武夫 (Inst. for Solid State Phys.)
FUJITA Junichi 藤田純一 (Tokyo Univ. of Educ.)
HANAZONO Sakae 花園 栄 (Inst. for Solid State Phys.)
HARADA Kichinosuke 原田吉之助 (Japan Atom. Energy Res. Inst.)
KOIKE Masahiro 小池正宏 (Inst. for Solid State Phys.)
NAKAI Koji 中井浩二 (Univ. of Tokyo)
NOMURA Toru 野村 亨 (Univ. of Tokyo)
YAMAZAKI Toshimitsu 山崎敏光 (Univ. of Tokyo)

Radiation Lab.

AWAYA Yohko 粟屋容子
HAMADA Tatsuji 浜田達二
HASHIZUME Akira 橋爪 朗
KATOU Takeo 加藤武雄
KONNO Satoshi 金野 智
OKANO Masaharu 岡野真治
TAKAHASHI Tan 高橋 旦
TENDOW Yoshihiko 天道芳彦

Nuclear Analytical Chemistry Lab.

AMBE Fumitoshi 安部文敏
AMBE Shizuko 安部静子
ARATANI Michi 荒谷美智
NOZAKI Tadashi 野崎 正
SAITO Nobufusa 斎藤信房

(Visitors)

AKIYAMA Nobuyuki 秋山信之 (Komatsu Electronic Metals Co., Ltd.)
YUITA Koichi 結田康一 (Nat. Inst. of Agr. Sciense)
IDO Tatsuo 井戸達雄 (Nat. Inst. of Radiological Sciense)
YATSURUGI Yoshifumi 八剣吉文 (Komatsu Electronic Metals Co., Ltd.)

Radiobiology Lab.

IGARASHI Kazui 五十嵐一戊
KITAYAMA Shigeru 北山 滋
MASUDA Fumihiro 増田文博
MATSUYAMA Akira 松山 晃

Radiation Chemistry Lab.

IMAMURA Masashi 今村 昌
MATSUI Masao 松井正夫

Metal Physics Lab.

HASIGUTI R. Ryukiti 橋口隆吉
KOYAMA Akio 小山昭雄
SAKAIRI Hideo 坂入英雄
SHIOTANI Nobuhiro 塩谷亘弘
YAGI Eiichi 八木栄一

(Visitors)

ISHINO Shiori 石野 栞 (Univ. of Tokyo)
MISHIMA Yoshitsugu 三島良績 (Univ. of Tokyo)
SHIRAISHI Haruki 白石春樹 (Nat. Res. Inst. for Metals)
TANI Satoshi 谷 賢 (Univ. of Tokyo)

Magnetic Materials Lab.

OKADA Takuya 岡田卓也
OKAMOTO Shoichi 岡本祥一
SEKIZAWA Hisashi 関沢 尚

Radiation Monitors

KODA Kugao 甲田陸男
SAKAMOTO Ichiro 坂本一郎
USUBA Isao 薄葉 勲

(Editors of the Progress Report)

IMAMURA Masashi 今村 昌
NOZAKI Tadashi 野崎 正
ODERA Masatoshi 小寺正俊
SEKIZAWA Hisashi 関沢 尚

AUTHOR INDEX

AKIYAMA Nobuyuki 秋山信之 80

AMBE Fumitoshi 安部文敏 85

AMBE Shizuko 安部静子 85,105

ARATANI Michi 荒谷美智 88

AWAYA Yohko 粟屋容子 31,35,38,57

CHIBA Yoshiaki 千葉好明 42,44,78

FUJISAWA Takashi 藤沢高志 25,42,44

FUJITA Jiro 藤田二郎 68

FURUKAWA Michiaki 古川路明 83

HAMADA Tatsuji 浜田達二 16,57,75

HASHIZUME Akira 橋爪 朗 46,57,63,72

HASIGUTI R. Ryukiti 橋口隆吉 98,101

HEMMI Masatake 逸見政武 19,22

IDO Tatsuo 井戸達雄 109

IMAMURA Masashi 今村 昌 90,93

INAMURA Takashi 稲村 卓 46,63

INOUE Toshihiko 井上敏彦 5

IZUMO Koichi 出雲光一 75

KAMITSUBO Hiromichi 上坪宏道 42,44

KARASAWA Takashi 唐沢 孝 11,90,95,98,101,105,109

KATOU Takeo 加藤武雄 54,57,63,75

KODA Kugao 甲田陸男 110,111

KOHNO Isao 河野 功 5,11,16,28,31

KOIKE Masahiro 小池正宏 42

KONNO Satoshi 金野 智 11

KOYAMA Akio 小山昭雄 101

KUMAGAI Hiroo 熊谷寛夫 72

KUME Sanshiro 久米三四郎 83

KUSUNO Sadao 楠野貞夫 31

Machine Group 2

MASUDA Fumihiro 増田文博 95

MATSUDA Kazuhisa 松田一久 31,35,38

MATSUI Masao 松井正夫 90,93

MATSUYAMA Akira 松山 晃 95

MIYAZAWA Yoshitoshi 宮沢佳敏 5,11

MIZOGUCHI Tadashi 溝口 正 105

MOTONAGA Shoshichi 元永昭七 25,42,44

NAGAMIYA Shoji 永宮正治 46,51,54

NAKAI Kozi 中井浩二 51

NAKAJIMA Hisao 中島尚雄 19,22

NAKAJIMA Shunji 中島諄二 5,28

NAKANISHI Noriyoshi 中西紀喜 31,35,38

NOMURA Toru 野村 享 51,54

NOZAKI Tadashi 野崎 正 80,83,88,109

ODERA Masatoshi 小寺正俊 28

OKADA Takuya 岡田卓也 105

OKANO Masaharu 岡野真治 75,83,109

SAITO Nobufusa 斎藤信房 85

SAKAIRI Hideo 坂入英雄 98,101

SAKAMOTO Ichiro 坂本一郎 16,110,111

SEKI Riki 関 喜紀 83

SEKIZAWA Hisashi 関沢 尚 105

SHIMAMURA Akira 島村 晏 5,16,109

SHIOTANI Nobuhiro 塩谷亘弘 105

SHIRAISHI Haruki 白石春樹 98

SHOJI Hitoshi 庄司 準 85

TAKAHASHI Tan 高橋 旦 11,95

TAKEDA Masuo 竹田満洲雄 85

TAKEDA Shigeru 竹田 繁 31,35,38,68

TENDOW Yoshihiko 天道芳彦 46,57,63,75

TONUMA Tadao 戸沼正雄 5,11,16,28

USUBA Isao 薄葉 勲 110,111

YAGI Eiichi 八木栄一 98,101

YAMAJI Shuhei 山路修平 31,40

YAMAZAKI Toshimitsu 山崎敏光 51,54

YAMAZAKI Yoshishige 山崎良成 51

YATSURUGI Yoshifumi 八剣吉文 80

YOKOI Shigeru 横井 茂 88

YOSHIDA Fusako 吉田房子 11,78

YUITA Koichi 結田康一 109

WADA Takeshi 和田 雄 25,42,44,78

IPCR Cyclotron Progress Report 1971

理化学研究所サイクロトロン年次報告 第5巻（1971）

印　刷　昭和47年（1972）3月25日
発　行　昭和47年（1972）3月30日
発行者　理化学研究所
代表者　星　野　敏　雄
351 埼玉県和光市広沢2番1号
電話（0484）62－1111
編集者　理化学研究所サイクロトロン運営委員会
委員長　浜　田　達　二
印刷所　丸星印刷株式会社
101　東京都千代田区
神田神保町1丁目42番地

定価 2,000円

理化学研究所

埼玉県　和光市　広沢